Study of Mineral Dissolution by Kinetic Monte Carlo Simulations

PhD Thesis by

Pablo Martín García

2020

Directed by:

Dr. Hegoi Manzano

Dr. Juan Jose Gaitero

eman ta zabal zazu

Universidad del País Vasco

Euskal Herriko Unibertsitatea

Study of Mineral Dissolution by Kinetic Monte Carlo Simulations

PhD Thesis by

Pablo Martín García

2020

Directed by:

Dr. Hegoi Manzano

Dr. Juan J. Gaitero

tecnalia Inspiring Business

Equipped with his five senses, man explores the universe around him and calls the adventure Science.

- Edwin Powell Hubble

Dedication

Esta tesis se la dedico a mis padres, que siempre quisieron que llegara tan lejos como ellos, y que sin ellos, no habría llegado tan lejos. Y a mi tía Isabel, quién me enseñó tanto.

Acknowledgments

¡Huid!, ahora que podéis. Estas sabias palabras fueron pronunciadas a un joven dieciochoañero y a sus compañeros de clase del primer curso del grado en física, mientras esperaban impacientes en el pasillo de la facultad a que sus inocentes mentes fueran sacudidas, y aturdidas, por una clase magistral de dispersión de errores. El estudiante de último curso que alertó a aquellos jóvenes cayó en el anonimato, pero no así su mensaje, que tantas veces fue rememorado por más de uno de aquellos jóvenes en sus años venideros, y que yo hoy rememoro para alertar a un incauto lector de lo que ha de encontrar en las siguientes páginas.

Movido por la valentía, curiosidad, o quizás inconsciencia, el dieciochoañero desoyó, al igual que tú, las indicaciones de aquel ducho estudiante, lo que ha conducido a que hoy, una década después, haya podido escribir este apasionante estudio sobre la disolución de minerales.

El camino que escogió aquel joven ha estado lleno de altibajos, pero no ha sido poca la gente dispuesta a ayudarle y hacerlo más llevadero. Vislumbrando ya la meta, ese joven escribe hoy, un poco menos joven, palabras de agradecimiento a todas aquellas personas.

En primer lugar quiero agradecer a mis padres todo el apoyo que me han dado durante todos estos años. La perseverancia y las ganas de aprender son dos de las cualidades que se han esforzado en inculcarme, y a pesar de mis reticencias iniciales, creo que lo han conseguido. A mi hermano Fernando le quiero agradecer el tirar de mi durante tantos años, además de legarme el gusto por la bici, y a mi hermano Javier por compartir la afición del deporte conmigo, además de unas cuantas 'partiditas' al ordenador.

A Anita la conocí algo antes de empezar la tesis, y ha tenido que soportar la que más las consecuencias. Gracias por seguir ahí.

A Jorge y a Hegoi les quiero agradecer haber confiado en mí y haberme dado la oportunidad de adentrarme en el mundo de la investigación dentro del equipo de Tecnalia. Sin lugar a dudas la calidad de esta tesis, tanto científica como artística, no habría sido la misma sin las pautas y consejos que ambos me han dado. Además de mi mejora en el mundo científico, mi mejora en el mundo futbolístico no es tema menor. Gracias a Hegoi dejé de ser ambidiestro, igual de malo con la derecha

que con la izquierda, para ser malo solo con la derecha.

A Jontxu le agradezco sus recomendaciones, tanto en este trabajo como en otros, y esas reuniones en bicicleta, que junto con David Salgado, me permitió conocer algún que otro rincón de Vizcaya y ponerme a prueba mis habilidades sobre esta. ¡Algún día te alcanzaré!.

A Achu le agradezco toda la ayuda en temas de programación, y la subida al Pagasarri, propia de todo buen bilbaíno.

A Edu le agradecco haberme guiado, tanto en mis inicios, antes incluso de empezar con mi doctorado cuando aún cursaba el máster, como al terminar con él.

A muchas otras personas de Tecnalia como Edurne, Eunate, Vero, Jaime, Aratz, Josean, David, Fran, Rubén, Alex, Asier, María, Ana, Marta, Raffaele, Idoia, Gurutze, Jaca, Iñigo y seguro que me olvido de más, les agradezco haber hecho mi estancia en Tecnalia más agradable, llena de conversaciones interesantes y momentos divertidos. A Idoia y Gurutze les quiero agradecer además acogerme en el laboratorio para escribir esta 'masterpiece' y alimentarme abundantemente con chocolate, galletas, y otras fuentes de energía para mi exhausto cerebro.

Durante mi doctorado estuve tres meses en Delft, en los Países Bajos. A pesar del indecente frío y monótono paisaje, recuerdo con especial cariño aquella preciosa ciudad. Jorge, Achu y Edurne son mayormente culpables de ello.

Big thanks to the Materials and Environment department of the civil engineering faculty of TUDELFT. Thank you, Prof. Klaas van Breugel, for giving me the opportunity to work with you, and thank to Josef, Jiayi, Sthephan, Claudia, Yuan, Kai Yang and Prof. Ye guang, for making me feel at home since the very first day.

Los últimos agradecimientos van para mis amigos, tanto de Santander como los que me conseguí hacer en Bilbao, por ayudarme a desconectar en el día a día.

Gracias a todos,

Pablo

Table of Contents

List of Figures

List of Tables

List of Abbreviations

TCD Thermal conductivity detector 19

CSTR Continuously stirred tank reactor 22

FBR Fluidized bed reactor 22

SEM Scanning electron microscopy 23

VSI Vertical scanning interferometry 23

AFM Atomic force microscopy 23

DHM Digital holographic microscopic 24

TST Transition State Theory 25

KMC Kinetic Monte Carlo 31

MC Monte Carlo 31

TLK Terrace Ledge Kink system 36

PBC Periodic boundary conditions 49

List of Relevant Symbols

$r_{\mathbf{D}}$ Mineral dissolution rate (mol m^{-2} s^{-1}) 2

ΔG Gibbs free energy (J mol^{-1}) 3

Π Ion activity product 4

$K_{\mathbf{s}}$ Thermodynamic solubility product 4

R Ideal gas constant (8.3145 J mol^{-1} K^{-1}) 4

β Saturation index 4

γ Activity coefficient 4

C Concentration (mM) 4

$C_{\mathbf{e}}$ Concentration at equilibrium (mM) 4

ΔG^{*} Local or superficial Gibbs free energy (J mol^{-1}) 5

k Dissolution rate constant (mol m^{-2} s^{-1}) 5

$\Delta G_{\mathbf{crit}}$ Critical Gibbs free energy at the middle of the onset (J mol^{-1}) 6

$C_{\mathbf{s}}$ Concentration at the surface (mM) 8

D Diffusivity (m s^{-1}) 8

S Surface area (m^2) 8

δ Diffusive layer (m) 8

ξ Roughness factor 8

v Kinematic viscosity (m^2 s^{-1}) 8

$F_{\mathbf{r}}$ Flow rate (m^2 s^{-1}) 8

ω Angular velocity (rad s^{-1}) 10

A' Arrhenius prexponencial factor (mol m^{-2} s^{-1}) 10

$E_{\mathbf{a}}$ Dissolution activation energy (J mol^{-1}) 10

$\overline{V}$ Molar volume (m^3 mol^{-1}) 18

$\ddagger$ Transition state or activated complex 26

$E_{\mathbf{B}}$ Energy barrier (J mol^{-1}) 26

$f_{\mathbf{f}}$ Fundamental frequency (s^{-1}) 26

$k_{\mathbf{B}}$ Boltzmann constant ($1.38 \cdot 10^{-23}$ J K^{-1}) 27

h Planck constant ($6.626 \cdot 10^{-34}$ J s) 27

q Partition function 27

ν_l Vibrational frequencies (s^{-1}) 30

r' Rate (s^{-1}) 32

$\Delta G'_{\mathbf{crit}}$ Critical Gibbs free energy when dislocations in a mineral start to open (J mol^{-1}) 38

$\Delta G'_{\mathbf{m.III}}$ Critical Gibbs free energy when mechanism III appears (J mol^{-1}) 39

$\Delta G_{\mathbf{m.III}}$ Critical Gibbs free energy when mechanism III has half of its contribution (J mol^{-1}) 46

List of Relevant Relations

$R = N_A \cdot k_B$; N_A Avogadro number $(6.022 \cdot 10^{23})$

1 $k_B T$ units = 2.494 kJ mol^{-1} = 0.596 kcal mol^{-1} at 300 K

1 cal = 4.18 J

List of Minerals

Muscovite $KAl_2(AlSi_3O_{10})(F,OH)_2$ 1

Cinnabar HgS 1

Sphalerite ZnS 1

Cassiterite SnO_2 1

Sapphire Al_2O_3 1

Ruby Al_2O_3:Cr 1

Quartz SiO_2 2

Calcite $CaCO_3$ 2

Kyanite Al_2SiO_5 3

Halite NaCl 3

Brucite $Mg(OH)_2$ 7

Alite Ca_3SiO_5 7

K-feldspar $KAlSi_3O_8$ 14

Sanidine $AlSi_3O_8$ 15

Calcic plagioclase $CaAl_2Si_2O_8$ 15

Rutile TiO_2 15

Fluorapatite $Ca_5(PO_4)_3F$ 16

Labradorite $(Ca,Na)(Si,Al)_4O_8$ 16

Albite $NaAlSi_3O_8$ 17

Diamond C 21

Moissanite SiC 21

Gypsum $CaSO_4{\cdot}2H_2O$ 24

Belite Ca_2SiO_4 24

Aluminate $Ca_3Al_2O_6$ 24

Smectite $(Na,Ca)_{0.33}(Al,Mg)_2(Si_4O_{10})(OH)_2{\cdot}nH_2O$ 61

Portlandite $Ca(OH)_2$ 133

General Introduction

The earth's surface is composed of rocks, soils, as well as other materials that contain different types of minerals. Minerals dissolve and precipitate when interact with water. As minerals dissolve, chemicals in the solid phase transform into ions in water, resulting in a decrease of the mineral mass and volume. Dissolution process is important in both natural and engineered processes. It has influenced on water geochemistry, soil formation, contaminant transport, acid stimulation in reservoir engineering, environmental remediation, and global carbon cycling. As an engineered example, acid stimulation in oil reservoirs accelerates mineral dissolution, increasing reservoir porosity and permeability and enhancing oil extraction. As a natural example, the CO_2 consumption during chemical weathering in a mineral dissolution reaction helps to regulate atmospheric CO_2 and maintain the conditions for life on earth.

Understanding the mechanisms involved in water-mineral interaction requires both experimental and computational techniques. In this context, both experimental and computational works have aimed at characterizing their interactions, highlighting the importance of their concomitant mechanism and processes at the atomic scale.

At this scale, atomistic modelling has demonstrated to be an indispensable numerical instrument. It allows to study the nanoscale of a material or molecule with detail. However, atomistic simulations are often difficult to compare to experimental results due to its time and length limitations. Other modelling tools, like the Kinetic Monte Carlo method, can help to bridge the gap between them.

This thesis has focused on the study of the mineral dissolution by using Kinetic Monte Carlo method. In the following chapters we will describe the scientific contribution of the authors that can be summarized in:

- Chapter 1: A revision of the state of the art of the water-mineral interaction, highlighting the more relevant experimental techniques and modelling tools.

- Chapter 2: Extension and improvement of Kinetic Monte Carlo method and the kinetic model from the bibliography, to reproduce the general behaviour of the mineral dissolution and to

provide an explanation to experimental observations.

- Chapter 3: Presentation of KIMERA, a Kinetic Monte Carlo code developed to study the dissolution of minerals.
- Chapter 4: A general parametric study of minerals with AB composition and different structures.
- Chapter 5: A specific study of the quartz dissolution in water, which serves also as a verification of the proposed model in chapter 2.
- Chapter 6: A study of the dissolution phenomenology of alite due to its importance in the field of cement.

Overall, this thesis presents an extension of the kinetic model and a powerful code based on it. Both tools represent a great advance and provide continuity on deepening the knowledge on the field of mineral dissolution.

Chapter 1: State of the art

1.1 Introduction to mineral dissolution

A mineral is defined as a solid chemical compound that can be found in nature in pure form, usually as aggregates in rocks [25]. They are crystalline compounds with a well defined chemical composition and a specific crystal structure. If a chemical compound may occur naturally with different crystal structures, each structure is considered a different mineral species. The interest of the minerals can be commercial or ornamental. For example, muscovite ($KAl_2(AlSi_3O_{10})(F,OH)_2$), can be used for windows, as a filler or as an insulator [26]. Other minerals have a high concentration of a valuable element. Examples are cinnabar (HgS), an ore of mercury, sphalerite (ZnS), an ore of zinc, or cassiterite (SnO_2), an ore of tin. Other minerals, known as gemstones, have an ornamental value due to their beauty, durability, and usually rarity. Gemstone examples are sapphire (Al_2O_3) and ruby (Al_2O_3:Cr).

The dissolution or hydration of minerals is a specific case of a branch of physical chemistry named chemical kinetics, also known as reaction kinetics. The origin of this branch of science dates back to 1884 when Van't Hoff published his famous 'Études de dynamique chimique' [27] and was awarded the first Nobel Prize in Chemistry in 1901. Since then, chemical kinetics deals with the experimental determination of reaction rates from which rate laws are derived. Chemical kinetics includes investigations of how experimental conditions influence the speed of the chemical reactions as well as the construction of mathematical models that describe them. Chemical kinetics is well complemented by thermodynamics. Although thermodynamics cannot tell anything about the reaction rate, they deal with the direction in which a process occurs because of the nature's tireless pursuit of the equilibrium in a minimum energy state.

The mineral dissolution rate is defined as the quantity of dissolution reactions happening per unit

time [28]. Usually, the mineral dissolution is a complex reaction involving several elementary ones at molecular level. Therefore, an overall reaction represents the net result of a series of its elementary reactions. The slowest step is the limitant of the reaction and is particularly important as it marks the overall dissolution rate.

Researchers have focused on measure mineral dissolution rates in order to make predictions of the evolution of our environment, and thus, their impact in the human activity and health [3,6]. Controlling soil fertility, porosity in aquifers and oil reservoirs, transport and sequestration of contaminants and CO_2, cycling of metals and formation of ore deposits, building, etc are among its most significant applications [29–37]. Works have been done over the years, improving the understanding in the interaction between the solvent and the minerals [1] and improving the experimental techniques to isolate the variables which influence their dissolution rate [2,12,19,21,38]. With the improvement of computers, limitations on downscaling of experimental techniques were complemented by methods such as *ab initio* calculations, molecular dynamics and molecular mechanics, bringing to light the role played by the elementary reactions happening at the molecular level [39–45]. Other computational methods such as Monte Carlo (MC) or Kinetic Monte Carlo (KMC) have helped the scientists to bridge the properties obtained from these calculations to the experimental ones, upscaling the atomic level energy barriers to the nanoscale to reproduce the experimental properties and dissolution rates.

1.2 The mineral dissolution rate

The characterization of a dissolving mineral is measured by the amount of material (in moles) released per second and per surface area, that is, its dissolution rate r_D (mol m^{-2} s^{-1}). Such property is in the first place influenced by the crystal structure and the chemical bonds of the mineral. At 300 K in pure water, typical dissolution rates lies in a range between 10^{-13} and 10^{-6} mol m^{-2} s^{-1} for very covalent minerals like for example quartz (SiO_2), and very ionic minerals like calcite ($CaCO_3$) (see figure 1.1). A 1 mm spherical grain of these minerals would take about 1000 years and 1 hour to dissolve respectively [31].

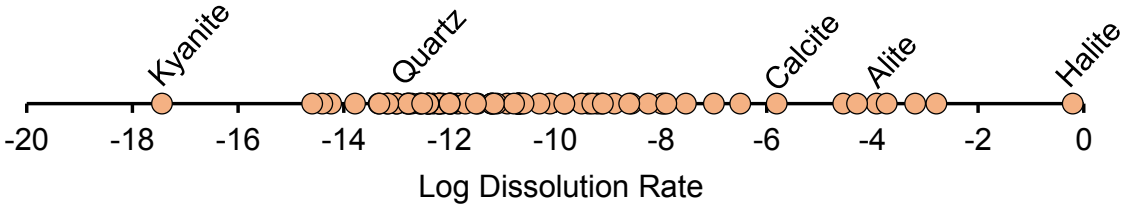

Figure 1.1: **Compilation of mineral dissolution rates**. Logarithm of the dissolution rates for 78 minerals at 300 K [1]. Kyanite (Al_2SiO_5) and halite (NaCl) are respectively the lower and higher limit cases.

The dissolution rate can be found in the bibliography as a negative or a positive magnitude indistinctly. It depends on which reference point is taken; the mineral, or the solvent. In this work we have taken preferably negative values unless a comparison with published plots with positive ones is done. In general the experiments show a low reproducibility of the dissolution rate. A dispersion of the results by an order of magnitude is usually found. [][]

The more important factors affecting the dissolution rate are: temperature [1], pH [1,3], Gibbs free energy difference between solid and solution (ΔG) [6], solution chemistry [31], reactions of transport [3,6] and dislocation density [46]. Moreover and as a curiosity, some microorganisms can influence on the previous factors to boost or inhibit the dissolution rate according to their needs [47,48].

Next step we explain the factors that affect dissolution one by one in the following order for clarity purposes.

1.2.1 Variation of the mineral dissolution rate with ΔG

Considering a mineral immersed in water, in the surface of the mineral there are reactions of the constituent atoms with water at the mineral surface, and then, diffusion of the dissolved atoms within the water [3,6]. The reactions taking place on the surface are closely related to the already dissolved atoms within the closest water layer. The higher concentration, the lower the dissolution rate. This driving force of the reaction, related to the concentration, is named Gibbs free energy difference ΔG (J mol^{-1}).

Given an elementary reaction like:

$$aA + bB \leftrightarrow cC + dD \tag{1.1}$$

ΔG is experimentally calculated from the ion activity product Π of the dissolved material in water divided by the thermodynamic solubility product K_s.

$$\Delta G = R \cdot T \cdot \ln(\Pi / K_s) \tag{1.2}$$

R is the ideal gas constant (8.3145 J mol^{-1} K^{-1}) and T the temperature (K). Π/K_s is more commonly known as saturation index β and sets the distance to equilibrium where no dissolution happens. Therefore, K_s is defined as the activities Π in which the reaction is in equilibrium. Π is experimentally obtained from:

$$\Pi = \frac{\{C\}^c \cdot \{D\}^d}{\{A\}^a \cdot \{B\}^b} \tag{1.3}$$

where $\{A\}$, $\{B\}$, $\{C\}$ and $\{D\}$ represents the activity and a, b, c and d their respective stoichiometric coefficients. The activity represent the effective concentration truly available to react. The called activity coefficient γ has values between 0 and 1 $\gamma \in [0,1]$ to represent the available concentration reacting (mM). For example $\{A\} = \gamma_A \cdot [A]$.

In the specific case in that the reaction is in equilibrium, $\Pi = K_s$ and thus $\Delta G = 0$. If $\Delta G < 0$, the solution is undersaturated and dissolution happens, and if $\Delta G > 0$, the solution is supersaturated and the mineral grows by precipitation. In very diluted systems, instead of activities, concentrations can be used since the dissolved components are spread far apart and interactions among them are very weak thus $\gamma = 1$:

$$\Delta G = R \cdot T \cdot \ln(C / C_e) \tag{1.4}$$

Where C is the concentration and C_e is the concentration in which the system is at equilibrium.

As we will see in the next section, there is a discrepancy between the measured ΔG and the one at very close to surface positions since the concentration is not the same as in the bulk water. Therefore, from now on, we differentiate between macroscopic or apparent ΔG and superficial or local ΔG^*.

The mineral dissolution rate is influenced by its distance from equilibrium. Some of the studied minerals present a dissolution rate dependence with ΔG that increases sharply by getting away from the equilibrium to reach gradually a plateau (see figure 1.2) [6].

$$r_{\mathrm{D}} = k\left(1 - \left(\frac{\Pi}{K_{\mathrm{s}}}\right)^{p}\right)^{q} \tag{1.5}$$

Where k is the dissolution rate at far from equilibrium conditions in the plateau, also named dissolution rate constant. The parameters p and q are empirical and dimensionless. Expression 1.5, without p and q , can be predicted by the Transition State Theory (TST) as we will see subsequently. This curve shape has been overshadowed by experimental curves of some minerals following a sigmoid function [31,49,50]. Different regions in the sigmoidal function are governed by different dissolution mechanisms depending on the mineral bond energy and ΔG. These mechanisms can be observed when vertical scanning interferometry (VSI), atomic force (AFM) or scanning electron microscopy (SEM) are used to follow the surface topography during dissolution [21, 49–52] (see sections 1.3.2.1, 1.3.2.2 and 1.3.2.3). In a typical curve like the one portrayed in figure 1.2, three mechanisms with different dissolution rates can be distinguished:

- **Mechanism I**. At low negative ΔG, the superficial groups of atoms (terraces) and lonely atoms (adatoms) on the mineral surface dissolve leading to flat and smooth areas. The dissolution rate is very low due to the close position to equilibrium state.

- **Mechanism II**. As ΔG decreases, topographical defects of the mineral like vacancies and dislocations become dissolution cores, which lead to pit opening and step retreat.

- **Mechanism III**. As ΔG becomes even lower, any surface atom can become a dissolution core. However, this only occurs in minerals with low bond energy, like calcite.

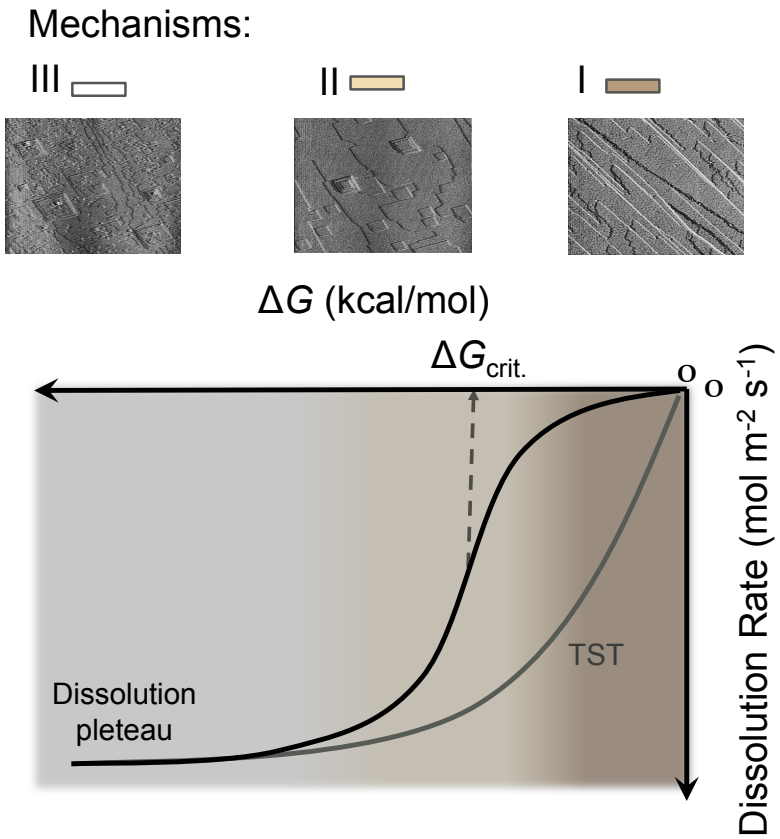

Figure 1.2: **Dissolution rate with** ΔG. Schematic representation of the mineral dissolution rate. The typical curve predicted by the TST and the sigmoid function experimentally reported are represented. Depending on the sigmoid curve region, the mineral presents three well diferentiated dissolution mechanism; I) Flat surfaces II) Pit opening and step retreat III) Spontaneous pit opening.

The three dissolution mechanisms are additive and must coexist, that is, it is not possible to have mechanism II without mechanism I, or mechanism III without II and I, and they take place simultaneously. The value of ΔG where the onset of dissolution rate takes place due to mechanism II is called critical ΔG (ΔG_{crit}). In figure 1.2, the topography observed for calcite in the different dissolution mechanism and the schematic representation of the sigmoid function are highlighted.

From these experimental results it can be inferred that the mineral dissolution rate is closely related to its topography. Over the years, several topographical models have focused on trying to predict dissolution rates depending on the mechanism that is active [7, 10, 20, 31, 53–56]. As we will see, a model was developed for relating the ΔG_{crit} to the elastic properties of the mineral, and thanks to the TST, experimental curve fits with reasonable success were proposed [9, 10] (see section 1.4).

In this thesis, part of the work is focused in the study of the dissolution rate dependence with ΔG. Most of the important results obtained are the outcome of the study of this relation as we will show in the subsequent chapters.

1.2.2 Variation of the mineral dissolution rate with the diffusion

The concentration of the dissolved material within the solvent is not constant. As it is shown in the figure 1.3 with a schematic representation of a dissolving mineral grain, at close to surface distances the concentration C_s is expected to be higher than the concentration at water bulk C, which is the one usually measured by the experiments. The difference between both quantities is determined by the dissolution rate and the diffusivity of the dissolved material into the water. Depending on which one of those two factors is slower, the dissolution process is said to be limited by surface reactions or limited by transport, respectively [6]. In figure 1.4 different scenarios are presented. It shows the concentration profile with the distance from the surface. If the dissolution rate is very low, like in quartz, every dissolved atom is immediately diffused and the concentration is very similar as a function of the distance from the surface (see case 2 in figure 1.4). The other way around, if the dissolution rate is high, like in calcite, the diffusion is not able to vacate the material and the concentration in the surface C_s increases until reaching a concentration close to the equilibrium one C_e where the dissolution is much lower (see case 3 in figure 1.4). In most cases, both effects are balanced and the diffusion managed to vacate partly the dissolved material (see case 1 in figure 1.4). Case 4 would correspond to the concentration profile expected during growth, where thanks to precipitation, the concentration close to the surface decreases.

As we will see in the next section, the dissolution rate changes with temperature. Diffusivity is also affected by the temperature change because a reduction of the water density, but in much lower degree. In a mineral, it may happen that the limiting step changes when increasing the temperature, as in the case with brucite ($Mg(OH)_2$) at 323 K [57]. It may also happen that the increase of the dissolution rate due to the deviation from equilibrium is enough to produce this change, as demonstrated recently in alite (Ca_3SiO_5) [21].

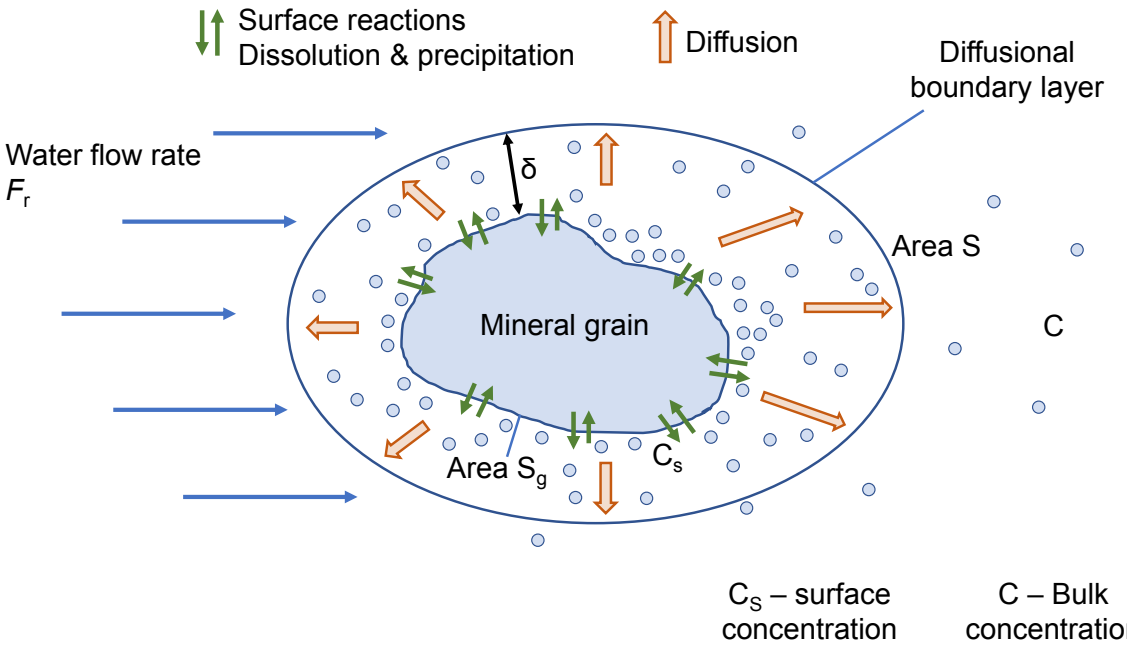

Figure 1.3: **Diffusive layer**. Schematic representation of the diffusive layer of a dissolving mineral. The concentration close to the surface is expected to be higher than the bulk concentration in the water. Adapted from [2].

The concentration in the surface C_s (and so ΔG^*) can be estimated by considering, instead of a exponential decay, a linear one by getting far from the surface (Fick's law) [2, 6, 58].

$$D \cdot \frac{C_s - C}{\delta} = \frac{S_g}{S} \cdot k \left(1 - \frac{C_s}{C_e}\right) \tag{1.6}$$

where D is the diffusivity (m s^{-1}), S is the diffusive layer surface (m^2), S_g is the grain surface (m^2), and δ is the size of the diffusive layer (m) (see figure 1.3). $\xi = \frac{S_g}{S}$ is the named roughness factor, which depends on the specific grain shape in the experiment.

The size of the diffusive layer δ can be estimated by [58]:

$$\delta = \left(\frac{2 \cdot \Pi}{0.244}\right)^{1/3} \cdot v^{1/6} \cdot F_r^{-1/2} \cdot D^{1/3} \cdot x^{1/2} \tag{1.7}$$

where v is the kinematic viscosity of the water (m^2 s^{-1}), F_r is the flow rate (m^3 s^{-1}) and x can be considered to be the largest diameter of the dissolving grains (m). Typical values for experiments are the following: $v \sim 10^{-7}$ m^2 s^{-1}, $F_r \sim 10^{-9} - 10^{-8}$ m^3 s^{-1} [59], $D \sim 10^{-13}$ m s^{-1} and $x \sim 10^{-3} - 10^{-4}$

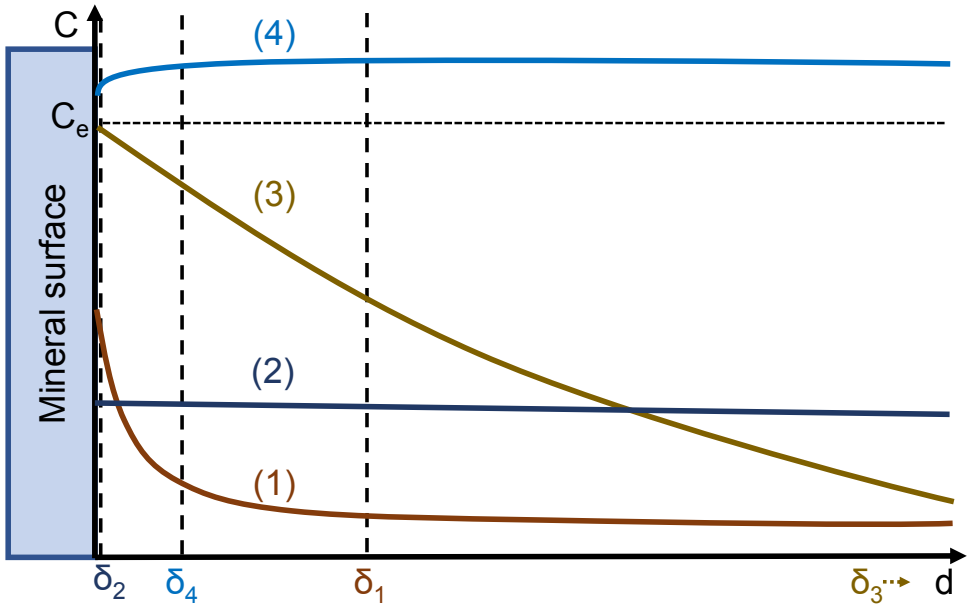

Figure 1.4: **Concentration profile within the diffusive layer**. Schematic representation of the concentration gradient within four different cases: 1) Typical case where the dissolution rate and diffusivity are balanced. 2) Extreme case where the diffusivity is much higher than the dissolution rate. 3) Extreme case where the the dissolution rate is much higher than diffusivity. 4) Typical case in mineral growth. δ is the size of the diffusive layer defined by the concentration plateau. Adapted from [3].

m leading to a δ in the order of μm. This equation is suitable for most experimental devices generating a laminar water flow, without turbulences. In a rotating disk experiment, which we will describe later (see section 1.3.1.2), the expression is slightly different.

$$\delta = 1.61 \cdot D^{1/3} \cdot \nu^{1/6} \cdot \omega^{-1/2} \tag{1.8}$$

where ω is the disk angular velocity (rad s^{-1}).

We can then relate the 'apparent' dissolution rate k' obtained from experiments to the 'real' one k:

$$k' = \frac{1}{\frac{1}{\xi \cdot k} + \frac{\delta}{D \cdot C_e}} - \frac{1}{\frac{C_e}{\xi \cdot k} + \frac{\delta}{D}} \cdot C \tag{1.9}$$

This equations, apart from considering some geometric approximations, are based in a normal behaviour of the TST (see figure 1.2). This means that minerals whose dissolution follows normal TST trend with ΔG would get more accurate results. For the rest of the minerals, deeper study would be needed but it represents a good first approach.

1.2.3 Variation of the mineral dissolution rate with T

The famous Arrhenius equation as it is known today was not the first law proposed to describe the mineral dissolution rate dependence with temperature, but it has been one of the most extended [60].

$$k = A' \cdot \exp\left(-\frac{E_a}{R \cdot T}\right) \tag{1.10}$$

Where A' is a constant (mol m^{-2} s^{-1}) and E_a is the named dissolution activation energy (J mol^{-1}) and is related to the energy needed for the limiting reaction in the dissolution process.

In fact, modified Arrhenius equations reproducing the temperature behaviour were proposed, which suggested a temperature dependent prefactor $A'(T)$ related with the vibrational frequencies of the limiting reaction and whose contribution is marked when the activation energy is low [6].

$$k = A' \cdot T^n \cdot \exp\left(-\frac{E_a}{R \cdot T}\right) \tag{1.11}$$

Where n is a fitting parameter that usually lies between $1/2$ and $3/2$.

Nowadays, despite the prefactor may be temperature dependent, it is assumed to be constant. All possible contributions of the prefactor are assumed to have its effects on the global or apparent activation energy E_{app} and therefore equation 1.10 is recovered by simply replace E_a by E_{app}. Keeping in mind this formalism, we use in this work the original Arrhenius equation 1.10 which is obtained from the slope of representing the natural logarithm of the dissolution rate $\ln k$ versus the inverse of the temperature $1/T$.

$$E_{app} \equiv -R\left(\frac{\partial \ln k}{\partial(1/T)}\right)_P \tag{1.12}$$

The overall activation energy is mainly determined by the limiting step of the reaction. As said in the previous section, this step can be related to a surface reaction, or to the transport of the dissolved material. As the surface reactions are more influenced by the temperature than the diffusion, the activation energies in the first case are much greater than in the second. Typical activation energies for a surface limited dissolution lies between 30 and 100 kJ mol^{-1} [1]. The activation energy when the diffusion is the limiting factor is lower than 30 kJ mol^{-1} [6]. Figure 1.5 shows a schematic representation of typical curve by representing the $\ln k$ versus $1/T$ and highlighting the two slope regions corresponding to surface and transport reactions.

1.2.4 Variation of the mineral dissolution rate with pH and other catalytic or inhibitory effects

pH is one of the factors that strongly affects the dissolution rate, and it has been one of the most widely studied. Many minerals show a U-shaped relation (V-shaped on logarithmic plots) between dissolution rates and pH. This trend is roughly in parallel with the mineral solubility and surface charge [6]. For a given temperature, rates are slowest at the pH where the mineral surface has a

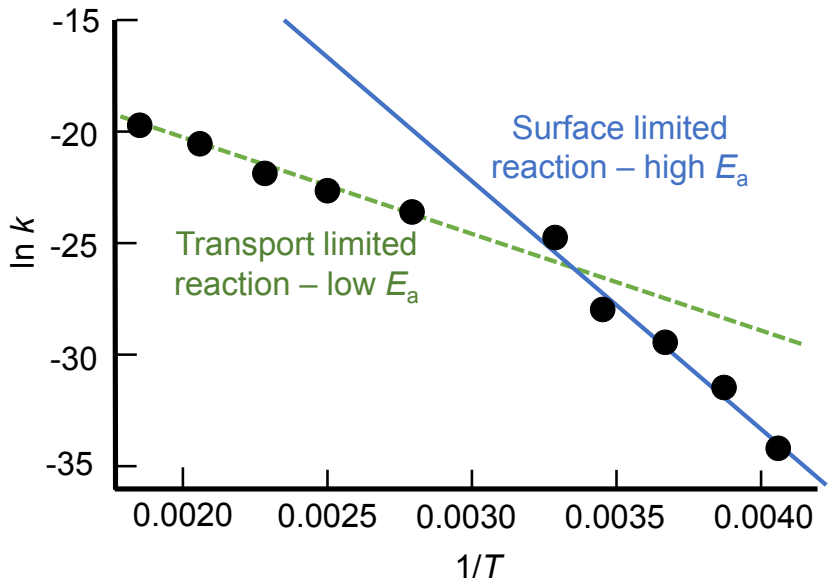

Figure 1.5: **Arrhenius plot**. Schematic representation of an Arrhenius plot. The limiting reaction generally changes with temperature. Adapted from [3].

neutral net charge, labeled pH of zero point charge , and usually shifted one or two pH units from the neutral pH 7. As a general rule, at low pH, rates increase with decreasing pH catalyzed by H^+, and at high pH, rates increase with increasing pH, catalyzed by OH^- [1]. This behaviour can be observed in some minerals in figure 1.6, where the dissolution rate constant k is represented with pH at 300 K [31].

Based on this three regions of the curve, acid, neutral and basic, the dependence of the dissolution rate with pH is usually written as follows:

$$k = k_{\text{acid}} \cdot \{H^+\}^{n_1} + k_{\text{neut}} + k_{\text{base}} \cdot \{H^+\}^{n_3} \tag{1.13}$$

where $\{H^+\}$ is hydrogen ion activity and n_1 and n_3 are fitting parameters. Here, base contribution is related to $\{OH^-\}$, but in water $\{OH^-\}$ can be related to $\{H^+\}$ with a negative n_3 [1]. k_{acid}, k_{neut} and k_{base} represent the dissolution rate at far equilibrium condition in each region.

Other anions and cations also affect in the dissolution rate. In nature, mineral dissolution may be affected by inorganic or organic solutes that can act as catalysts or inhibitors [31]. The effect of them is very specific of each mineral since it is very related to the mechanisms involved at the

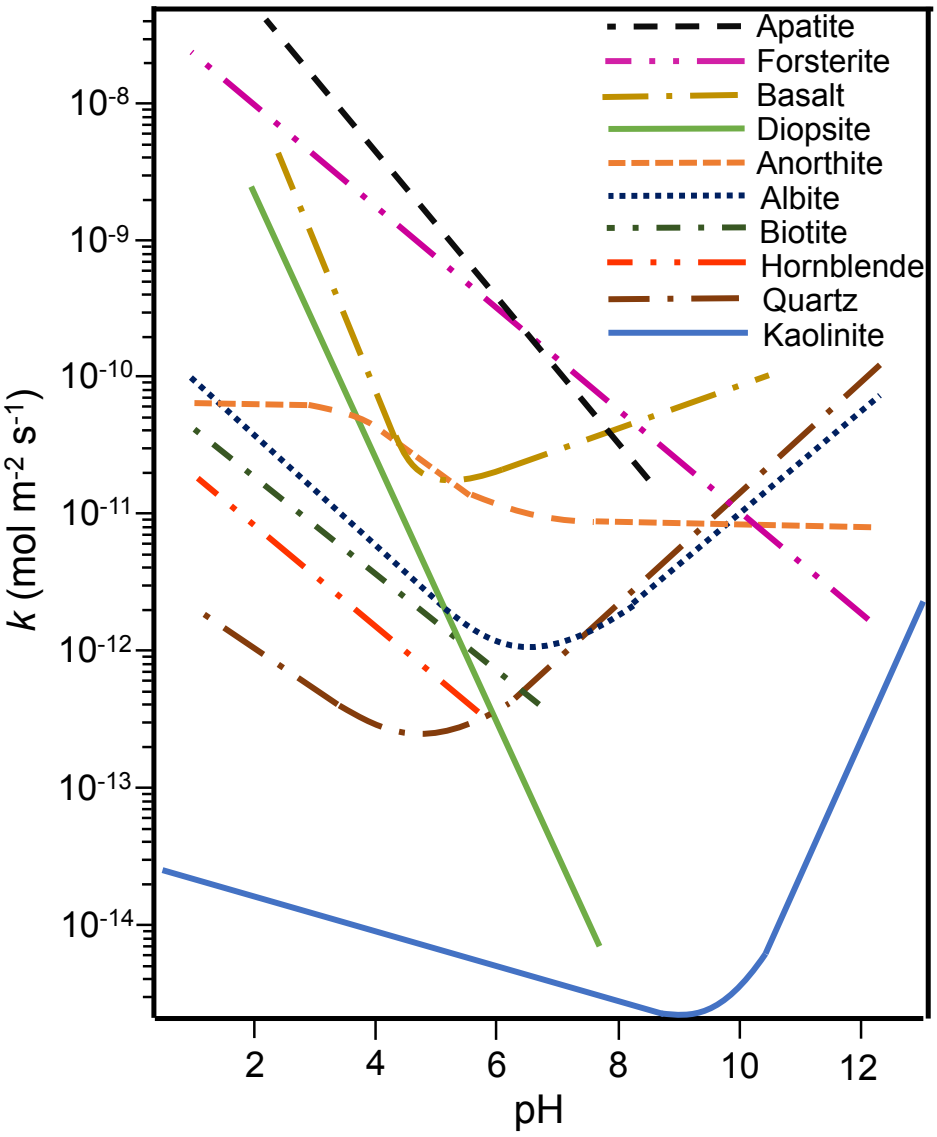

Figure 1.6: **Dissolution rate dependence with pH**. Some of them present the typical V shape curves. Adapted from [3].

atomic scale in the surface reactions. Cations that enhance the dissolution in some minerals may decrease it in some others. Fore example, Mg^{2+}, Ca^{2+}, Li^{+} Na^{+}, K^{+} and Ba^{2+} cations increase the dissolution of quartz, but decrease it in albite, K-feldspar ($KAlSi_3O_8$) and calcite [31]. The functions which describes the dependence of the dissolution rate with the activity of the cations and anions are numerous. One of the most extended is based on the named Lagmuir model [31] which considers the surface as a network of empty sites that are occupied by the adsorbate reaching a saturation state. For example, the inhibitory effect of salt on dissolution of K-feldspar and albite in acidic solution follows the next expression:

$$f\left(\{H^+\},\{M_i\}\right) = \frac{\{H^+\}\cdot K_{sH}^{ads}}{1+\{H^+\}\cdot K_{sH}^{ads}+\sum_i\{M_i\}\cdot K_{sM_i}^{ads}} \tag{1.14}$$

where M_i refers to adsorbing cations, and K_{sH}^{ads} ads and $K_{sM_i}^{ads}$ refer to the equilibrium constants for adsorption of H^+ and M_i on the surface site corresponding to the bridging oxygen between silicon and aluminum.

1.2.5 Variation of the mineral dissolution rate with the mineral topography and size

Other factors that may affect the dissolution rate are the grain shape and size, and the dislocation density. Looking at the minerals from an atomistic point of view, it has been demonstrated that the more bonds or coordination a chemical specie has, the more difficult for it to dissolve, either because of the reduction of the accessibility of the water molecule to produce the hydrolysis reaction or because the intrinsic change of energy by increasing the number of bonds [6]. Dislocations, defects, corners and edges of a mineral produce a decrease of the coordination and therefore the dissolution rate is enhanced. Experiments conducted for the same mineral with different density of initial irregularities on the surface result on different dissolution rates. Not waiting long enough for the mineral to reach the steady state when the surface has smoothed would also show discrepancies between experiments. Note that the time needed to reach the steady state in a experiment for covalent

minerals and low temperatures can be unaffordable.

Similar problems are found for the grain size. A big grain containing long perfect planes is preferentially dissolved by the corners. When the grain little by little decreases in size, the fraction of perfect planes is lower and the density of sites with lower coordination increases, and so its dissolution rate. To overcome this effect, experiments are usually done within a period of time in that the reduction of grain size is not significant. An example of this effect can be found in quartz. A great difference for the activation energy in water has been experimentally found in several works, $E_a = 46 - 90$ kJ mol^{-1} [19]. Such difference was explained by Tester *et al.* due to the existence of small grains on the surface of the bigger samples. Naturally, the importance of this two effects in the dissolution rate is closely related to the atomic structure of the mineral but it may affect in one or two orders of magnitude [61].

Finally, the effect of dislocation density has been also widely studied [62]. Numerous works have documented that dislocation density has an insignificant effect in the dissolution rates. For example, in sanidine ($AlSi_3O_8$) no difference was found when dislocation density increased from 10^{10} to 10^{12} – 10^{13} m^{-2} [63]. In quartz, despite an increase from 10^{10} to 10^{15} m^{-2}, the dissolution rate in distilled water and HF solutions remained the same [46]. In calcic plagioclase ($CaAl_2Si_2O_8$), rutile (TiO_2) and calcite, from 10^{10} to 10^{14} m^{-2} the increase was only three times greater [55, 64–66]. It looks surprising that dislocations, which play a fundamental role in the dissolution rate onset with ΔG, have such a low dependence with their density.

Some authors have suggested than the spontaneous pit opening or mechanism III in the perfect planes are responsible of this dislocation density inaction (see section 1.2.1). As artificial 'dislocations' are produced during dissolution, it does not matter the existence or not of previous ones. We will demonstrate that this idea is not misguided as we will see in following chapters. Nevertheless mechanism III is not very common and is restricted only to low bond energy minerals. A possible explanation will be presented for those minerals without such mechanism (see section 2.4.6).

1.2.6 External stimuli of the dissolution rate

It may happen that the mineral dissolution rate is influenced by an external stimulus that is able to change one or several of the factors described below. One of the most studied stimulus are the microorganisms. Microorganisms can influence the dissolution rate of a mineral having either a catalytic or inhibitory effect. In calcite for example, VSI measures in the presence of the bacteria *Shewanella oneidensis* MR-1 shows no mechanism III, so typical of this mineral, and a dissolution rate below the detection limit of the VSI method [47]. Other work has studied the impact of the rhizosphere (region of the soil containing roots) in the dissolution of fluorapatite ($Ca_5(PO_4)_3F$) and labradorite ($(Ca,Na)(Si,Al)_4O_8$); minerals containing the Ca needed for the plants to grow. Results have been compared with the dissolution in soil without roots, obtaining that rhizosphere can regulate to its needs the dissolution rate by a factor of 3 or 4 by changing the solvent conditions [48]. As a curiosity, a relatively new field of study is the named biomineralization [67, 68], and seeks for mimic the microorganism ability to synthesize complex organic-inorganic hybrid structures such as teeth, bones and shells.

Other external stimuli are the emission of x-ray radiation over the mineral surface during its dissolution, inducing very far from equilibrium conditions [69], or the emission of the ultrasounds which increase the dissolution rate by promoting the atomic interaction [70].

1.2.7 Compilation of the important factors within a single equation

The three more important contributions of T (equation 1.10), pH (equation 1.13) and distance to equilibrium (equation 1.5) are collected in the following equation 1.15 [1].

$$
\begin{aligned}
r_{\mathrm{D}}\left(T,\{H^{+}\},\Pi/K_{\mathrm{s}}\right) = & k_{\mathrm{acid}}^{300}\cdot\exp\left(\frac{-E_{\mathrm{acid}}}{R}\cdot\left(\frac{1}{T}-\frac{1}{300}\right)\right)\cdot\{H^{+}\}^{n_1}\cdot(1-(\Pi/K_{\mathrm{s}})^{p_1})^{q_1} \\
& + k_{\mathrm{neut}}^{300}\cdot\exp\left(\frac{-E_{\mathrm{neut}}}{R}\cdot\left(\frac{1}{T}-\frac{1}{300}\right)\right)\cdot(1-(\Pi/K_{\mathrm{s}})^{p_2})^{q_2} \\
& + k_{\mathrm{base}}^{300}\cdot\exp\left(\frac{-E_{\mathrm{base}}}{R}\cdot\left(\frac{1}{T}-\frac{1}{300}\right)\right)\cdot\{H^{+}\}^{n_3}\cdot(1-(\Pi/K_{\mathrm{s}})^{p_3})^{q_3}
\end{aligned}
\tag{1.15}
$$

where the dissolution rate constant k is taken at 300 K to facilitate the comparison of the rates between minerals. E_{acid}, E_{neut} and E_{base} are the activation energy for each mechanism (J mol^{-1}) and k_{acid}, k_{neut} and k_{base} their dissolution rate constant (mol m^{-2} s^{-1}).

This expression is general but presents some exceptions as described above. An experimental setup with big diffusive layer or a sigmoid dependence instead of a normal TST curve are clear candidates to spoil such predictive equation, though it would help to obtain a good first approximation.

1.2.8 Disagreement of field and laboratory dissolution rate measurements

Once we have compiled all the main factors affecting the dissolution in our laboratory experiments, one could think that it is time to predict the mineral water interaction in the field. Nevertheless it can be a gap up to 5 orders of magnitude lower in the dissolution rate in the field, depending on the mineral. [71]. Gruber *et al.* demonstrated in their work in albite ($NaAlSi_3O_8$) that the origin of such discrepancy lies, on the one hand, in the closeness to equilibrium of the field weathering, and on the other hand, in a lower reactivity due to the lower amount of irregularities on the surface. In essence, in the discrepancy of conditions between field and laboratory measurements.

1.3 Experimental devices for measuring the dissolution rate

To determine the dissolution rate, experimentalists have used two different approach. On the one hand, chemical reactors in which mineral powders are weathering under controlled conditions of pressure and temperature. On the other hand, direct microscopic examinations of the mineral surfaces.

In the first case, the dissolution is obtained from the detected amount of one of the constituent elements of the mineral divided by its stoichiometric coefficient. The chemical reactors used can be further divided into two types depending on how the measurements are taken: the batch reactor, and the mixed flow reactor [3]. Furthermore, other variants from these ones were subsequently developed [5]. For the microscopic observations of the mineral surface, experimentalists have used techniques such as atomic force microscopy (AFM) [49,72–74], vertical scanning interferometry (VSI) [10,21,47,74], scanning electron microscopy (SEM), or more recently the digital holografic miscroscopy (DHM) [2,38,75–77] and have revealed important details of nanoscale topography. The dissolution rate in these cases is calculated from the surface retreat depth compared to a region of the mineral where a 'mask', usually Polymethyl methacrylate (PMMA), has been set to avoid dissolution.

$$r_{\mathrm{D}} = \frac{dz}{dt} \cdot \overline{V} \tag{1.16}$$

where dz is the average difference of height with the mask (m) and $\overline{V}$ is the molar volume of the dissolving mineral ($\mathrm{m}^3\ \mathrm{mol}^{-1}$).

The comparison between these two sets of experimental devices is difficult since microscopic measurements are taken in one face, whereas powder-based measurements are an average value over all crystal faces along with the contribution from sharp corners. In the next step, operation and characteristic of the experimental devices are explained.

1.3.1 Reactors

Surface area

An estimation of the grains area of the mineral powder is needed to get the correct dissolution rates in the experiments. Basically there are two methods: geometric basis, and BET. First one is intuitive. It is based on calculate the area from the shape and size grain determined by microscopic observations or sieving. It requires often a simplification such as considering the grain as a sphere, a cube or

a rhombohedron. Besides, it does not consider any surface topography or roughness that would increase the total surface. To solve this problem, a surface roughness factor ξ is usually introduced which relates the total surface area with the geometric one [3].

$$\xi = \frac{S_g}{S} \tag{1.17}$$

where S_g is the grain surface and S its geometrical one. This factor is usually estimated by looking at the pits density in the surface with SEM images, thought it can be a difficult task since a deep pit can contribute with surface as much as several smaller ones.

Second method, named after its developers, Brunauer, Emmett and Teller (BET) [78] is based on measuring the quantity of a gas adsorbed by the surface. The used gas is usually an inert one, like nitrogen, krypton, or argon, so the attachment to the surface is only produced by van der waals forces and there is no change of the mineral chemistry. In general, two different techniques can be distinguished for the adsorption analysis; the thermal conductivity detector (TCD), which only gives information of the quantity of gas adsorbed, or the volumetric technique, which is based on pressure measurements in an enclosed volume and it provides information about pore volume and pore size distribution.

Plenty of works have discussed which one of the two method, the geometrical or BET, is best to get the correct surface area [79]. Typically BET surface areas are larger than geometrical estimations. The difference varies greatly between different minerals and is particularly sensitive to microporosity effects that may vary between samples of the same mineral. Moreover, dissolution within the micropores is expected to be much lower because of the high local concentration of the pore solution. For example in quartz, the geometric basis seems to report better results since its pits are nonreactive [14].

1.3.1.1 Batch reactor

Batch reactors are stirred tank reactors which run without flow (see figure 1.7a). These may be open or closed to the atmosphere. The progress of the reaction can be known by monitoring the

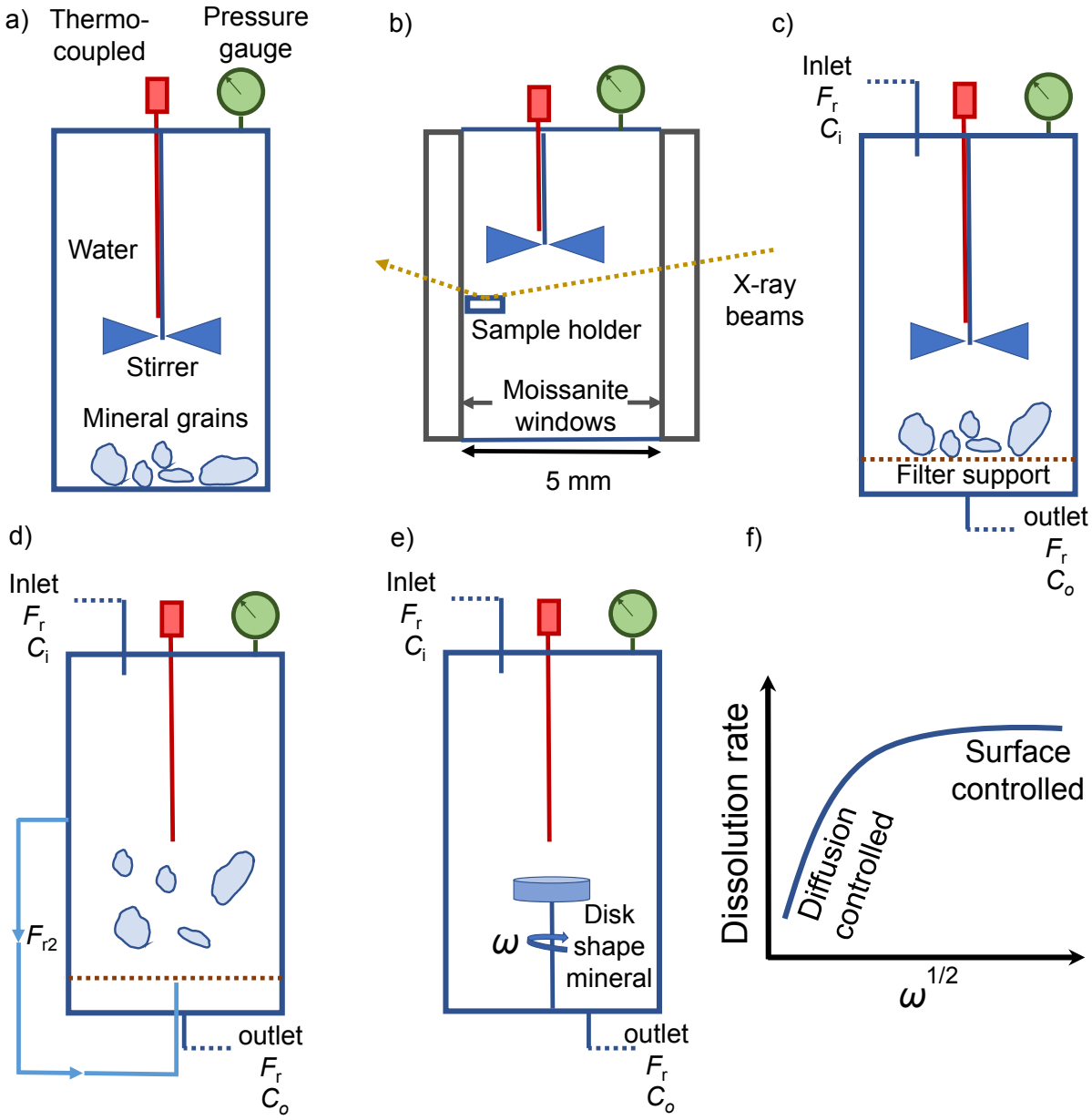

Figure 1.7: **Reactors for determining the dissolution rate**. Schematic representation of the experimental reactors. a) Batch reactor. b) Microreactor. c) Mixed flow reactor. d) Fluidized bed reactor. e) Rotating disk reactor. f) Typical curve of the dissolution rate with the rotating speed in a rotating disk reactor highlighting the two regimes. The diffusion is neglected if the rotating speed is high enough. Adapted from [3–5].

concentration of dissolution products as a function of time, and by correcting the removal of sample during monitoring. If the fluid is not repeatedly sampled during the experiment, repeated runs of increasing duration are required to characterize the rate of reaction advancement by removing fluids and solids at different times. The advantage of its simple use is overshadowed by the disadvantage of the interpretation of the results. The large diffusivity layer expected due to lack of flow (see section 1.2.2), the change of the solution chemistry over time, the back reactions including precipitation of secondary phases, or the presence of cations and anions influence the dissolution rate and mechanisms. The dissolution rate in batch reactor can be calculated from the equation 1.18 supposing a reaction as in equation 1.1 ($aA + bB \leftrightarrow cC + dD$).

$$r_{\mathrm{D}} = \frac{V}{S \cdot c} \cdot \frac{d[C]}{dt} \tag{1.18}$$

where V is the volume of water (m^3), $[C]$ the molar concentration of element C (mM) and c its stoichiometric coefficient. In batch experiments, solid samples can only be recovered from apparatus after the experiments are terminated. Batch apparatus that permit time sampling of solids are custom made not available commercially [5].

Microreactor

The limitations of the batch reactor motivated the development of microreactors capable of in situ monitoring of fluid rock interactions (1.7b) [5]. Only of few microlitres in size, they have transparent windows constructed of diamond (C) or moissanite (SiC). In situ monitoring of reactions is performed using methods such as X-Ray diffraction, X-ray fluorescence, Infrared or Raman techniques. Thought this devices has been limited to mineral physics for high pressure, the development of low-pressure reactors with an external control on the fluid opens new perspectives for the study of water-rock interactions using a wider range of characterization tools. The main disadvantage of this reactor is that the size of the window may require the use of synchrotron radiation in order to get the required small resolution and beam intensity for analyzing such small volumes of minerals and fluids.

1.3.1.2 Mixed flow reactor

In a mixed flow reactor, also named continuously stirred tank reactor (CSTR), a mineral sample is placed in a reactor and the solvent is pumped through with a flow rate F_r. The fluid is stirred by a propeller or by agitation (see figure 1.7c). The dissolution rate is calculated from the inlet $[C]_i$ and outlet $[C]_o$ concentrations of a component released during dissolution of the mineral:

$$r_D = \frac{F_r\left([C]_o - [C]_i\right)}{S \cdot c} \tag{1.19}$$

Dissolution rates are reported with respect to outlet solution chemistry when $[C]_o$ reaches a constant steady-state value.

Fluidized bed reactor

A modification of the previous one, named fluidized bed reactor (FBR), is a stirred tank reactor that apart from the main flow F_r uses a faster recirculating secondary one to suspend the grains to manage a complete mixing (see figure 1.7d). Same equation 1.19 is used to determine the dissolution rate. One criticism of fluidized bed reactors is the abrasion caused by turbulent collision of particles. This abrasion could lead to production of fine particles resulting in misleading dissolution rate data.

Rotating disk

The rotating disk setup consists of placing in the center of the vessel the mineral with a disk shape (see figure 1.7e). By rotating this disk some advantages are achieved; fluid motion is induced by the disk rotation, large fluid volumes are not required and, more importantly, with enough rotating speed ω, the diffusive layer is negligible (see figure 1.7f and section 1.2.2) [4]. Same as before, equation 1.19 is used to determined the dissolution rate.

1.3.2 Characterization techniques

1.3.2.1 Scanning electron microscope

A scanning electron microscopy (SEM) allows to get images of the mineral surface topography by scanning it with a focused beam of electrons. The electron beam is scanned in a raster scan pattern, and the position of the beam is combined with the intensity of the detected signal to produce an image. It is also possible for SEM to ionize the atoms of the mineral and make them emit x-ray with a wavelength that is specific of its composition. SEM achieves resolution on the order of the nanometer and thank to its great depth of field, it can produce images that are good representations of the three dimensional surface shape of the sample. Nowadays it is a widely used technique and almost every experiment uses it to characterize at least the sample surface.

1.3.2.2 Vertical scanner interferometry

The vertical scanning interferometry (VSI) captures intensity data at a series of positions along the vertical axis z for each x, y point, determining where the surface is located by using the shape of the white light interferogram. The intensity data as a function of the optical path difference are processed and converted to height information of the sample. This technique enables measuring height differences with a vertical resolution in the nanometre range, though it is objective dependent, and a lateral resolution typically in 0.5 μm [21]. Some minerals studied with this technique are calcite [47], alite [21], dolomite [10] and flourite [74].

1.3.2.3 Atomic force microscopy

The atomic force microscopy (AFM) device is based on scanning the surface by the vertical displacement of a cantilever placed in contact with it. The movement of the cantilever is detected by the fluctuation of the reflection of a laser light which is pointing at it. This technique allows resolution on the order of the nanometer. Some minerals studied with this technique are quartz [72, 73], albite [49] and fluorite [74].

1.3.2.4 Digital holographic microscopy

The digital holographic microscopic (DHM) distinguishes itself from other microscopy methods by not recording the projected image of the object. Instead, the light wave front information originating from the object is digitally recorded as a hologram, from which a computer calculates the object image by using a numerical reconstruction algorithm. Therefore, the image formed by lens in traditional microscopy is replaced by a computer algorithm. This technique permits in situ measurements and is able to obtain the surface concentration close to the mineral surface C_s and the diffusive layer size from the local change of the water refractive index [2] (see section 1.2.2). Moreover, real time measurements provide extra information about the dissolution rate of each specific site of the surface (irregularities), obtaining the named dissolution rate spectra.

Very recent studies with DHM were done for gypsum ($CaSO_4 \cdot 2H_2O$) [2, 75], calcite [76], belite (Ca_2SiO_4) [38] and aluminate ($Ca_3Al_2O_6$) [77] and doubtlessly this technique will provide more information about the dissolution process in other minerals.

1.4 Modeling of mineral dissolution

Once we have seen how the mineral dissolution is studied experimentally, we go on to see the models that during these past 70 years have been proposed to describe the processes behind it. The first models were based on the macroscopic properties of the minerals. As the years went by and the importance of the atomic mechanisms became evident thanks to *ab intio* calculations, dissolution models have focused on describing the dissolution from the elementary reactions. The Transition State Theory (TST) sets the necessary guidelines to upscale this elementary reactions from the atomic scale to higher scales. Thanks to methods like MC and KMC, scientist have checked the evolution of multiple reactions happening at the same time that would otherwise be impossible to visualize. Nowadays, some authors continue exploring the dissolution process using general as well as specific models from nanoscale properties, other works have focused on continuing bridging the gap between experimental results and atomistic simulations. The Voronoi method for instance [80], which consists

of a geometrical approach able to bring KMC results to the macroscale, sets the step to follow in the study of mineral dissolution.

Herein we will explain the three main dissolution models of the bibliography in order of appearance (see section 1.4.5): The BCF model [7, 53, 54], the stepwave model [10] and the kinetic model [81]. Before moving to describe the models, four important tools are further explained which will help to understand them: the Transition State Theory (TST), *ab initio* calculations, the Kinetic Monte Carlo method (KMC) and the Kossel crystal system. The Kossel crystal is a simple and general way to describe the mineral topographic features and is widely used to study the mineral dissolution. In fact, all the three models use a Kossel crystal structure as first case of study. The other three tools are specific of the kinetic model. The TST set the basis to handle the time evolution of the reactions happening in a system. *Ab initio* simulations help to get the necessary parameters that determine those reactions, and the KMC method gets results of the time evolution in scales that are comparable to experiments. The kinetic model, in combination with the TST, *ab initio* calculations and KMC method, has proven to have a greater potential, though some of its features are still subject to discussion. In this thesis we have used and improved the kinetic model to describe the mineral dissolution.

1.4.1 Transition state theory

The Transtion State Theory (TST) was developed simultaneously in 1935 by Henry Eyring at Princeton University, and by Meredith Gwynne Evans and Michael Polanyi at the University of Manchester. Before its development, the Arrhenius rate law was widely used to determine reaction energy barriers (see section 1.2.3). Nevertheless, the Arrhenius equation was proposed from empirical observations and ignores any mechanisms involved in the reactions. Thanks to the TST, it was stated the origin of the two parameters in the Arrhenius equation (see equation 1.10) (see equation 1.10), the prefactor A' and the activation energy E_a.

TST is focused on explaining the reaction rate of the elementary chemical reactions that constitute the global reaction process. For that, it assumes that every reaction has a quasi-equilibrium state

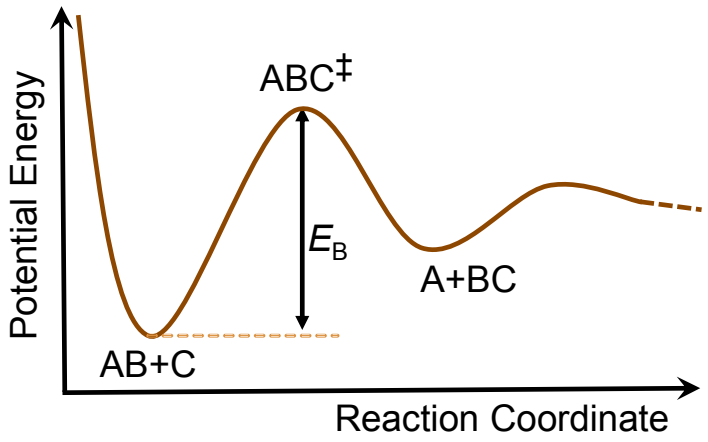

Figure 1.8: **Transition state theory**. Schematic representation of a simple reaction $AB+C \rightarrow A+BC$. Adapted from [6].

(‡) which needs to be overcome for it to happen, that is, the system needs enough energy to change its state (see figure 1.8). This energy barrier E_B depends on every single reaction in the system. From the properties of the initial state along with the quasi-equilibrium one, it is possible to obtain its elementary reaction rate. As we will see in the next section, *ab initio* calculations represent the perfect tool to characterize the transition states and get the necessary parameters for the TST. Other computational methods like molecular dynamics and mechanics with reactive empirical force fields are also suitable for this task but they are in principle less accurate.

Assume that we have an elementary reaction as the following happening at the mineral surface.

$$AB+C \rightarrow A+BC \tag{1.20}$$

In the quasi-equilibrium state, the system is in what is called the transition state or activated complex $[ABC]^{\ddagger}$, which is in equilibrium with the reactants.

$$K_s^{\ddagger} = \frac{\{ABC\}^{\ddagger}}{\{AB\}\{C\}} \tag{1.21}$$

We can then express the reaction rate r (mol m^{-2} s^{-1}) as the product of the frequency f_f (s^{-1}) with which the system tries to activate, and the concentration of reactants [6, 82].

$$r = f_{\mathrm{f}} \cdot [ABC]^{\ddagger} = f_{\mathrm{f}} \cdot \frac{\gamma_{AB}\gamma_C}{\gamma^{\ddagger}_{ABC}} \cdot K^{\ddagger}_{\mathrm{s}} \cdot [AB][C] \tag{1.22}$$

Herein the concentration is expressed in terms of surface area and not volume (mol m^{-2}). The γ is the called activity coefficient, $\{A\} = \gamma_A \cdot [A]$ and represent the proportion of atoms truly available to react in a time given by the frequency f_{f}. The activity coefficient has values between 0 and 1 $\gamma \in [0, 1]$. In a reaction of a mineral with water, values lower than 1 may be due to incapability of a water molecule to reach a reactive site on the surface. f_{f} is known as fundamental frequency.

$$f_{\mathrm{f}} = \frac{k_{\mathrm{B}} \cdot T}{h} \tag{1.23}$$

where k_{B} is the Boltzmann constant ($1.38 \cdot 10^{-23}$ J K^{-1}), h is the Planck constant ($6.626 \cdot 10^{-34}$ J s). $f_{\mathrm{f}} = 2.6 \cdot 10^{12}$ s^{-1} at 300 K. Using standard thermodynamic conventions, $K^{\ddagger}_{\mathrm{s}}$ can be also represented by

$$K^{\ddagger}_{\mathrm{s}} = \exp\left(\frac{-\Delta G^{\ddagger}}{R \cdot T}\right) = \exp\left(\frac{\Delta S^{\ddagger}}{R}\right) \cdot \exp\left(\frac{-\Delta H^{\ddagger}}{R \cdot T}\right) \tag{1.24}$$

where $\Delta G^{\ddagger}$, $\Delta S^{\ddagger}$ and $\Delta H^{\ddagger}$ are the Gibbs free energy, entropy and enthalpy change from reactants to activated complex, expressed in the appropriate units of the concentration. Note that $\Delta H^{\ddagger} = E_{\mathrm{B}}$ if the pressure and volume of the system do not change [3]. Overall, we can write the reaction rate as:

$$r = \frac{k_{\mathrm{B}} \cdot T}{h} \cdot \frac{\gamma_{AB}\gamma_C}{\gamma^{\ddagger}_{ABC}} \cdot \exp\left(\frac{\Delta S^{\ddagger}}{R}\right) \cdot \exp\left(\frac{-E_{\mathrm{B}}}{R \cdot T}\right) \tag{1.25}$$

or more typically, relating the entropy with the partition function q of each state of the reactants.

$$r = \frac{k_{\mathrm{B}} \cdot T}{h} \cdot \frac{\gamma_{AB}\gamma_C}{\gamma^{\ddagger}_{ABC}} \cdot \frac{q^{\ddagger}/S}{q_A/S \cdot q_B/S} \cdot \exp\left(\frac{-E_{\mathrm{B}}}{R \cdot T}\right) \tag{1.26}$$

Here do not confuse the S for surface area and the S for entropy in equation 1.25.

From this expression we can identify the preexponencial factor A', and the activation energy E_{a} in

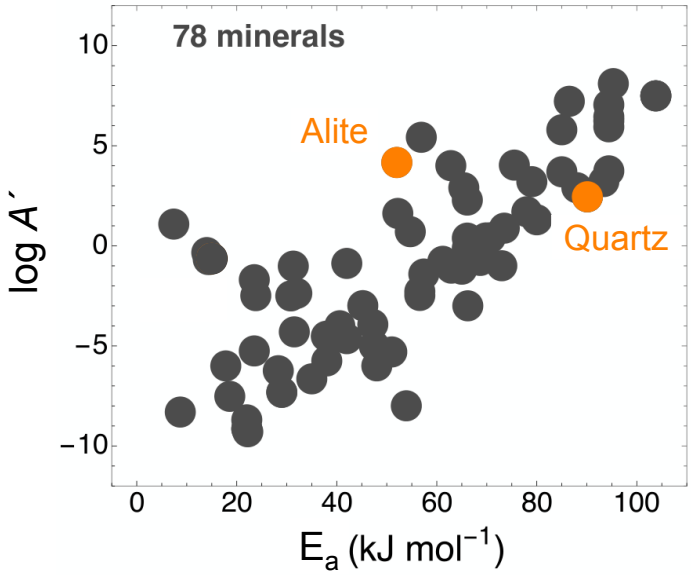

Figure 1.9: **Compensation law**. compilation of the A' values with activation energy from [1].

the Arrhenius equation 1.10 by using the definition of equation 1.12.

$$A' = \frac{k_B \cdot T}{h} \cdot \frac{\gamma_{AB}\gamma_C}{\gamma^{\ddagger}_{ABC}} \cdot \exp\left(\frac{\Delta S^{\ddagger}}{R}\right) \tag{1.27}$$

$$E_a = R \cdot T + E_B \tag{1.28}$$

These important results have two important implications. First, A' value contains information about the entropy of the constituent atoms of the mineral. In figure 1.9, a compilation of experimental values of A', in decimal logarithm, versus E_a is represented [1]. The observed lineal trend, known as compensation law, may not be very surprising if it is understood that atoms, having stronger bonds and therefore higher E_a, are expected to be more constrained in the transition state than as reactants, which decreases the vibrational modes and thus increases the A' values. Second, E_a has a term, $R \cdot T$, that may be important when E_B is low. For example at 300 K, $R \cdot T = 2.5$ kJ mol^{-1}. Remember that for most minerals, $E_a = 30 - 100$ kJ mol^{-1}.

Other important result of TST is the relation of the dissolution with ΔG. If consider the rate of opposite reactions of dissolution r_D and precipitation r_P, and taking into account that both rates

must at equilibrium be equal ($r_D = r_P \rightarrow \Delta G = 0$), by computing $r_D - r_P$ we reach the following expression [6]:

$$r_D = k\left(1 - \exp\left(\frac{\Delta G}{R \cdot T}\right)\right) \tag{1.29}$$

By considering expression 1.2, equation 1.29 matches the shape of the equation 1.5 experimentally reported above (see figure 1.2).

Nevertheless, as explained in section 1.2.1, the TST presents some limitations to reproduce the real mineral behaviour. The origin of this discrepancy has been explained based on two reasons. First, the dislocations and other defects play an important role in the kinetics dissolution, and these elements are not contemplated by the equilibrium in which the TST is based. Typical behaviour of the dissolution rate with ΔG when dislocations are leading the dissolution is as in equation 1.5 with $p = 2$ and $q = 1$. Secondly, TST is only adequate when there is only one limiting reaction in the overall process. Competing reactions would report a combination of TST behaviours [31, 83–86]. This assumption has been used to propose a fitting equation like:

$$r_D = k \cdot f(I) \cdot \prod\{j\}^{m_j} \cdot \left(1 - \exp\left(\frac{\Delta G}{\sigma \cdot R \cdot T}\right)\right) \tag{1.30}$$

where $f(I)$ is an equation describing the anion or cations activity like in equation 1.14, m_j is the stoichiometry coefficient of the j chemical species in each limiting reaction and σ is the Temkin's coefficient, which is used to account for sequential or parallel steps [6, 31]. Another example of fitting was used to describe parallel reaction activated with different ΔG, like in albite at 353 K at pH 8.8 [9, 31].

$$\begin{aligned} r_D = & k_1\left[1 - \exp\left(-\left(\frac{n_1 \cdot |\Delta G|}{R \cdot T}\right)^{m1}\right)\right] \\ & + k_2\left[1 - \exp\left(-\left(\frac{|\Delta G|}{R \cdot T}\right)^{m2}\right)\right] \end{aligned} \tag{1.31}$$

where m_1, m_2 and n_1 are fitting parameters and k_1 and k_2 the dissolution rate at far from equilibrium conditions of each reaction.

This fitting equations have been very handful to describe the dissolution of specific minerals. As we will see, other fitting equations were proposed based on the evolution of the mineral surface during dissolution. Nevertheless, a general dissolution rate law remains to be developed.

1.4.2 *Ab initio* calculations

The theories underlying atomistic simulation methods were independent from the existence of computers. However, the mathematical complexity of the algorithms to be solved made the computers indispensable in any atomistic simulation. Since computers became available for non-military purposes in the 50's, atomistic simulation methods have become essential in many different research areas, such as drug design in organic chemistry, protein and DNA studies in biochemistry, or magnetism, electronics and optics in material science [40].

Ab initio methods, also called first principles methods, owe their name to the fact that are derived directly from theoretical principles, and do not need any empirical parameter during the calculation. Just from the electronic interactions between atoms, they seek to solve the schrodinger equation for the electrons. Different approximations have been used and, as it always happen, the accuracy is at odds with calculation time. The simulations are based in the recursive calculations of the interatomic forces to reach equilibrium states. Therefore, defining a system as simple as possible but that captures the property to be studied is the critical part of planning a simulation. The fewer the atoms, the fewer the iterations and so the calculation time. Another important part is the selection of the basis set of functions used to describe the electron orbital of the atoms. The more functions, the higher the accuracy but also the calculation time. It may happen that one simple and one complex basis set reach the same results but with much higher computation time.

Ab initio simulations allows to study reaction pathways, transition states and electrostatic potentials, which are very handy for the TST. Reactions taking place in the mineral surface can be identified, as well as their energy barriers E_B. Moreover, by studying the vibrational frequencies ν_l of

the initial state of reactants (AB and C) and of the transition state ($ABC^{\ddagger}$), we can get their partition function q [6, 24].

$$q = \Pi_l \left(1 - \exp\left(-\frac{h \cdot \nu_l}{k_B \cdot T}\right)\right) \tag{1.32}$$

Once we have all the needed parameters to characterize the reaction on the surface of the mineral, we can use an upscaling methodology in order to describe them in larger length and time scales than the provided by *ab initio* calculations and get some results comparable with experimental ones. This method is named Kinetic Monte Carlo, a descendant of the famous Monte Carlo.

1.4.3 The Kinetic Monte Carlo method

1.4.3.1 History

The method commonly called Kinetic Monte Carlo (KMC) has a long history. Its ancestor, the Monte Carlo (MC) method, dates back to 1946, and was proposed by Stanislaw Ulam and John von Neumann [87]. Ulam, during an illness was playing solitaire and realized that it was much easier to get an idea of the overall result of solitaire by making numerous tests with the cards and analyze the probabilities of the results, rather than computing formally all the possible combinations. He realised that the same procedure could be used in the study of electron scattering in which he was working at *Los Alamos*, where he had to solve integro-differential equations with difficult analytical solutions. Ulam mentioned the method to von Neumann, who after initial skepticism, welcomed the method and began to apply it to trace isotropic generation from a variable composition of active material along the radius of a sphere. One of the first applications of this method to a deterministic problem was carried out in 1948 by Enrico Fermi, Ulam and von Neumann, when they solved the singular values of its Schrödinger equation [88].

The KMC method as we know it today was developed in 1966 by Young and Elcock [89] for the study of hole diffusion in a binary alloy. Independent of Young and Elcock's work, Bortz, Kalos and Lebowitz [90] developed a KMC algorithm which they called the *N-fold way* to simulate an

Ising model, and applied it to study the growth of a material. The basis of their algorithm is the same as in the case of Young and Elcock, although they provided much more detail on the method. Nowadays KMC has numerous applications such as the study chemical reactions [91], colloidal aggregation kinetics [92, 93], phase separation [94, 95], absorption and emission processes [94], diffusive transport [96, 97], heterogeneous catalysts [98] and naturally growth and dissolution of minerals and materials [99, 100], among others.

1.4.3.2 Theorical aspects

Now that we have the rate of transitions between states of a system from the TST in equation 1.26, we can correlate them with its global time evolution. Within a system where one particle can only evolve into close states, as it is the case here (see figure 1.10a), it can be mathematically probed that the probability of having a transition between states is independent of its history. This is known as the Markov property [101]. Physically speaking, we can assume that the previous reactions do not interfere on the probability of the current reaction, since the time of residence in a state is much longer than the period of vibration of the particle, and therefore it 'forgets' about the process that led it to its current state. The Poisson processes are the ones that, in addition to satisfying the Markov property, it is known the average time between them, as it is our case. The probability distribution of the time between Poisson processes is an exponential decay.

Imagine a particle in a given state, trying to reach multiple states by means of a reaction. The probability p_{stay} that the particle remains in the same state is:

$$p_{\text{stay}}(t) = \exp\left(-r'_{\text{tot}} \cdot t\right) \tag{1.33}$$

where r'_{tot} is the total particle reaction rate. Note that we consider on the following the expressions without mol m^{-2} normalization, r' (s^{-1}). Later the relation with r is direct.

We want to obtain the probability function $p(t)$ for the first escape in a time t' since once this happens, the system changes. Knowing that the integral of this function $p(t)$ at t' must be equal to $1 - p_{\text{stay}}(t')$ and taking into account the derivative of the equation 1.33, the expression 1.34 is

obtained:

$$p(t) = r'_{\text{tot}} . \exp(-r'_{\text{tot}} \cdot t) \tag{1.34}$$

The average escape time τ is the average of this distribution:

$$\tau = \int_0^\infty t . p(t) dt = \frac{1}{r'_{\text{tot}}} \tag{1.35}$$

It can be demonstrated that if we consider many particles, each of them with many possible transitions and independent from each other, the result is the same. Therefore, the time increment corresponding to one transition Δt does not depend on the probability for it to happen, but on the probability of all the transitions in the system.

Once we know how is related the rate of the transitions (or events as commonly known in KMC) with the system time evolution, it is time to see how to implement it in an algorithm.

1.4.3.3 Practical aspects

A typical KMC code follows the next implementation (see figure 1.10b):

1. The system is defined and initial time set to 0 ($t = 0$).

2. A list containing all possible events N_j of all the i particles is created.

3. A cumulative function R'_j of the rates r' of all possible events is then calculated and stored in an array (see figure 1.10c). $R'_j = \sum_{i=1}^{j} r'_i$ for all $j = 1, \cdots, N_j$. The total rate is $r'_{\text{tot}} = R'(N_j)$.

4. A random number u with uniform distribution is generated $u \in (0, 1]$. This random number is used to determine randomly the event to happen.

5. By comparing values in the stored array, we get the event j that is going to happen. The condition to achieve is $R'_{j-1} < u \cdot r'_{\text{tot}} \leq R'_j$. Two approaches are generally used to find it: the lineal search or the binary search [102]. The lineal search compares the values one by one from

one end of the array to the other. The binary search, which is more efficient, splits the search range in two and discards one of them if the value to be searched is not in it. The search range narrows until the value is found (see figure 1.10c).

6. The time increment is also random, yet it has to follow an exponential decay probability function typical of Poisson processes (see equation 1.34). Therefore, we need a random number within exponential distribution. One way to obtain it is to compute $\ln(1/u')$ from a random number u' with uniform distribution. Time t is then updated. ($t = t + \Delta t$)

$$\Delta t = \frac{1}{r'_{\text{tot}}} . \ln\left(\frac{1}{u'}\right) \tag{1.36}$$

7. The system is updated according to the found event, for example the removal of an atom from the surface. The state of the system has changed and it is necessary to create a new list with all possible events, that is, go back to point 2. Usually the transition affects only locally to a small part of the whole system, which can save great computational time [103].

Some practical guidelines about the KMC method are the following:

- The way the computation time scales with the number of operations is named computational complexity. The computational complexity associated to a KMC method is mainly related to the method used to find the event to happen, the step 5. In lineal search the complexity is $O(N_j)$ (N_j number of events). In binary search, $O\left(\log(N_j)\right)$. In the specific case of mineral dissolution, events are going to happen only in the surface. There is no need for a description of the events of the bulk atoms, which greatly reduces N_j.

- The KMC method is used to describe stochastic (or random) processes. In two different simulations the results are different. Therefore, several simulations are needed to obtain statically meaningful results.

- A typical disadvantage encountered with KMC method may arise when events have a great difference of rate. It may happen that a fast event makes a great computational waste without

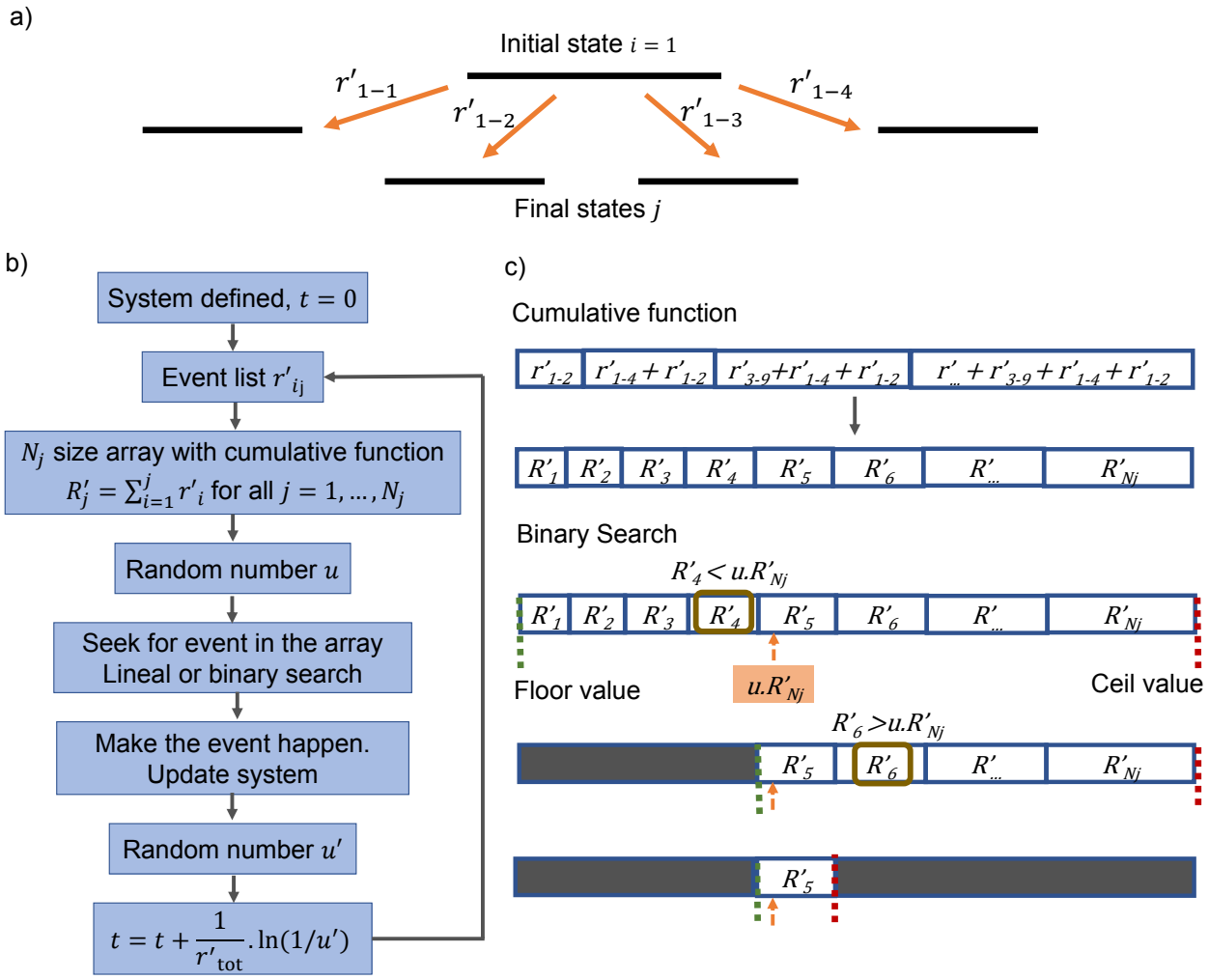

Figure 1.10: **KMC method**. a) Schematic representation of the possible transition states or reactions. b) Flowchart. c) Graphical explanation and binary search.

remarkable changes in the system. A clear example of this can be seen when studying the ion diffusion within a material [104]. Imagine we have two kind of events, one with a high rate (low E_B) like the rotation of a ion around the same atom, and one with a low rate (high E_B) as the translation of the ion to another atom. A great quantity of computational resources are wasted in the highly likely rotation events without actual net diffusion of the ion. The common way to solve this problem is to increment artificially E_B of the high rated event as far as the net result is not being biased [105]. In our specific case of mineral dissolution, and as we will see in chapter 2, we have developed a methodology to solve this problem without using this approach and without efficiency loss.

- The KMC method, in theory, reports an exact description of a system. In practice, to make a complete list of all events of the particles with their respective frequencies and energy barriers is unreachable. The important point here is that the possible events take into account all possible transitions relevant to the study of the desired property.

1.4.4 The Kossel crystal

Up to this point, thanks to the TST, we have seen the necessary elements to characterize a reaction, we have seen how *ab initio* methods can obtain them, and we have seen a methodology capable of observing properties on a larger temporal and spatial scale, the KMC method. The last necessary point is to describe our system. The reader may ask, why do not use the atomic surface of a mineral directly? Indeed, some examples of real surfaces studies have been done in recent years on minerals such as quartz or calcite [16, 106, 107]. However, complex *ab initio* simulations are needed to obtain all the vibrations and energy barriers of all possible reactions on the surface of a mineral. As we will see in chapter 5, quartz, one of the most studied minerals, still presents unknown energy barrier values. Therefore, in many works scientists have chosen to describe the surface of a mineral with a simple model able to provide general results. The system is named Kossel crystal.

A Kossel crystal, or Terrace Ledge Kink system (TLK) is a simple mineral structure consisting of

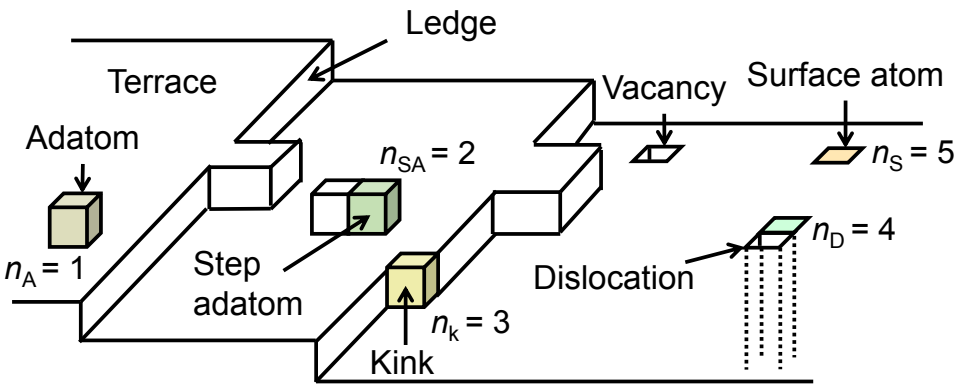

Figure 1.11: **Kossel crystal**. Simple model to describe the surface topography of a mineral. Dotted lines represent an infinite hole. Each site has different amount of first neighbours. An adatom $n_a = 1$, a step adatom $n_{sa} = 2$, a kink atom $n_k = 3$, a step atom $n_D = 4$ and a surface atom $n_S = 5$.

a cubic structure with six first neighbours [108] (see figure 1.11). This structure includes the different topographic elements that can be found on the surface of the mineral. There may be lonely atoms called adatoms, vacancies in the crystalline lattice, dislocations (represented by depth holes), terraces with kink atoms, and perfect flat surfaces.

Usually, studies performed in a Kossel crystal consider some approximations. First, the partition functions of the transition state and the reactants are the same, $q^{\ddagger}/q = 1$, and the value of the activity coefficients is $\gamma = 1$, letting the pre-exponential of equation 1.26 only with the fundamental frequency term (equation 1.23). Secondly, the energy barrier is considered to be lineal with the number of first neighbours n of each atom.

$$E_B = n \cdot E_{ba} \tag{1.37}$$

where E_{ba} is the energy barrier that an atom with one neighbour (an adatom) needs to react and be detached from the mineral surface. The number of neighbours range from 1 to 5 depending on the atom position in the surface (see figure 1.11). A bulk atom inside the mineral have $n_b = 6$. This fits with the idea that the more bonds an atom has, the harder to react.

Despite the simplicity of the Kossel crystal, it ensures enough topographical details so as to reproduce the mechanisms attributed to the dissolution process. Some studies in mineral dissolution

using this system are the presentation of the kinetic model [81] and the step retreat model [10] that we will see subsequently, as an introduction to the Voronoi method [80], the effect of the dissolution rate with the mineral size [61] and with the surface roughness [109], a study of calcite [110] and alite dissolution [111], and many others.

1.4.5 Dissolution models

Once we know four important tools in the study of mineral dissolution, we continue to look at the models that have been proposed and improved over the last 80 years that have benefited from them. Several models, all of them focused on the processes happening at the nanoscale, have been proposed but can be grouped in three main ones: The BCF model, the stepwave model, and the kinetic model. Below, we briefly describe them in order of appearance.

1.4.5.1 BCF model

Developed by Burton, Cabrera and Frank, [53,54] and later extended by Lasaga and Blum [7], this model was the first attempt to describe the influence of ΔG in the dissolution.

They based their model on the observed in experiments that dissolution was produced preferably around the dislocations. The model relates macroscopic properties of the mineral like the Poisson ratio, the shear modulus, and the Burgers vector that defines a dislocation, with the free energy needed for the dislocation to open $\Delta G'_{\text{crit}}$. Note that we have previously defined the ΔG_{crit} as the middle height value by convenience with the rest of our work (see figure 1.2), and here however, it is considered at the beginning of the onset.

Consider a deep hole in the mineral surface (see figure 1.12). The change in the surface free energy ΔG_{dis} when the hole grows can be computed by the sum of three terms. The first one account for the change of superficial energy by the volume of material dissolved. The second one accounts for the released stress density produced by the dislocation. Stress density is higher the closer to the dislocation. Finally, as opposite effect, the third term accounts for the increment of energy produced by a large amount of atoms located at the edge of dislocation, in less energetically favourable

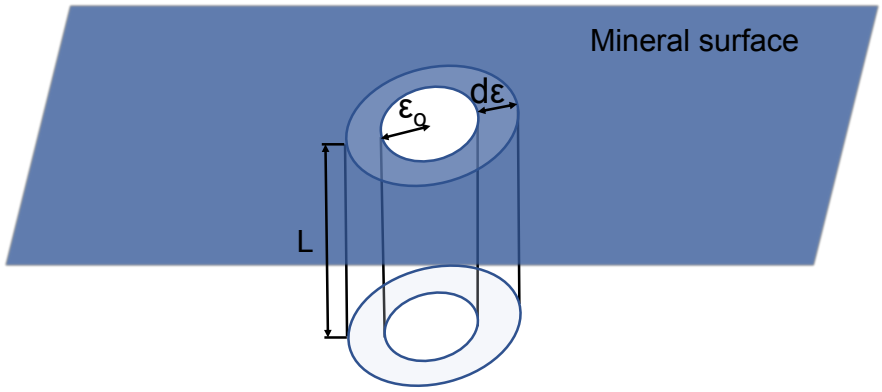

Figure 1.12: **BCF model**. Schematic representation of a deep hole on the mineral surface, the starting point for the development of the BCF model. L is the hole depth and ε_o its radius. Adapted from [7]

locations:

$$\Delta G_{\text{dis}} = \frac{\pi \cdot \varepsilon^2 \cdot a \cdot \Delta G}{\overline{V}} - \frac{a \cdot \tau \cdot b^2}{4 \cdot \pi} \ln\left(\frac{\varepsilon}{\varepsilon_o}\right) + 2 \cdot \pi \cdot \varepsilon \cdot a \cdot \Gamma \tag{1.38}$$

where ε_0 and ε is the dislocation initial and final radius (m), respectively, a is a geometric constant (m) , b the Burgers vector, $\overline{V}$ is the molar volume (m^3 mol^{-1}), Γ is the energy of the water-crystal interfacial energy (J m^{-2}), τ is an energy factor related with the shear modulus and Poisson ratio (J m^{-1}) and the dislocation type, edge or screw.

From the derivative of equation 1.38 against the radius, the expression that gives the energy at which the dislocation would continuously open is obtanined.

$$\Delta G'_{\text{crit}} = -\frac{2 \cdot \pi \cdot \Gamma^2 \cdot \overline{V}}{\tau \cdot b^2} \tag{1.39}$$

Moreover, if considering that there is no dislocations by removing the second term in equation 1.38, we can get the energy needed to produce mechanism III ($\Delta G'_{\text{m.III}}$), the spontaneous pit openning (see section 1.2.1).

$$\Delta G'_{\text{m.III}} = -\frac{\pi \cdot \Gamma^2 \cdot \overline{V} \cdot L}{\Delta G} \tag{1.40}$$

where L is the depth of the pit created. Note that, although the energy for the spontaneous pit opening $\Delta G'_{\text{m.III}}$ is dependent of the solvent through ΔG, the energy for dislocation opening $\Delta G'_{\text{crit}}$ is not.

Applications of the model predicts $\Delta G'_{\text{crit}}$ values ranging from -2 to -17 kJ mol^{-1} for a variety of defects in different minerals. For example in quartz $\Delta G'_{\text{crit}} = -2.28$ kJ mol^{-1} in pure water [31].

1.4.5.2 Stepwave model

This model was developed by Lasaga and Luttge [10]. It benefits from the results obtained by the BCF model and relates the overall dissolution of the mineral with the dissolution of the atoms at the edges of the dislocation. These atoms, forming steps, retreat layer by layer, as if they were a wave over the mineral surface. The dissolution rate is related with ΔG as follows:

$$r_{\text{D}} = B\left(1 - \exp\left(\frac{\Delta G}{R \cdot T}\right)\right) \cdot \tanh\left[\frac{A}{f(\Delta G)}\right] \cdot f(\Delta G) \tag{1.41}$$

$$f(\Delta G) = 1 - \left(\frac{1 - \exp\left(\frac{\Delta G'_{\text{crit}}}{R \cdot T}\right)}{1 - \exp\left(\frac{\Delta G}{R \cdot T}\right)}\right) \tag{1.42}$$

where A and B are the dissolution rate just before the dislocation opening at $\Delta G'_{\text{crit}}$ and at far from equilibrium conditions respectively ($B = k$, the dissolution rate constant).

1.4.5.3 Kinetic model

Lasaga and Luttge proposed then a model from an atomistic point of view [81]. They describe the dissolution process as a set of elementary reactions with different frequencies and energy barriers. The properties in which the other models are based, if the reactions are detailed described, could arise as results with this general model. They laid the foundation for the computational study by MC and KMC methods of the minerals from the TST. Part of the results of this thesis are the product of an extension of their kinetic model.

They describe in their model three different types of reactions interplaying on the mineral

surface; dissolution, precipitation and diffusion over the surface. They applied it to an A-B Kossel crystal consisting of two different types of atoms interspersed in the three directions of space, like a three-dimensional chessboard. It is established that the probability of dissolution of an atom is the conditional probability of breakage of every bond, which is known as the 'flickering-bond' model:

$$E_{\mathrm{B}} = \sum_{i=1}^{n} E_{\mathrm{b}i} \tag{1.43}$$

where $E_{\mathrm{b}i}$ is the contribution from every single bond to the overall energy barrier and n the total number of bonds. Note that if we consider this contribution is the same for each bond, the equation 1.37 is recovered.

In the presentation of the model, additional approximations were assumed. First, the breakage and reforming of bonds is equally energetic (see equation 1.37). Second, the rate of precipitation is constant and does not depend on the number of neighbors since it is supposed to happen exclusively in a kink site $n = 3$ (see figure 1.11), which is the preferable site to react in a mineral [6]. Finally, the diffusion of atoms is done diagonally over the surface of the Kossel crystal. This last approach is taken to avoid that an atom of one type has to pass through a position with an atom of the same type (like the bishop on a chess board).

The equations describing the model are the following:

$$r'_{\mathrm{D}} = f_{\mathrm{f}} \cdot \exp\left(-\frac{n \cdot E_{\mathrm{b}a}}{k_{\mathrm{B}} \cdot T}\right) \tag{1.44}$$

$$r'_{\mathrm{P}A} = f_{\mathrm{f}} \cdot \exp\left(-\frac{3 \cdot E_{\mathrm{b}a} - \Delta G_A}{k_{\mathrm{B}} \cdot T}\right) \tag{1.45}$$

$$r'_{\mathrm{P}B} = f_{\mathrm{f}} \cdot \exp\left(-\frac{3 \cdot E_{\mathrm{b}a} - \Delta G_B}{k_{\mathrm{B}} \cdot T}\right) \tag{1.46}$$

$$r'_{\mathrm{Diff}} = f_{\mathrm{f}} \cdot \exp\left(-\frac{(n-1)E_{\mathrm{b}a} + E_{\mathrm{b.diff}}}{k_{\mathrm{B}} \cdot T}\right) \tag{1.47}$$

where ΔG_A and ΔG_B are the Gibbs free energies due to the concentration of A and B elements in the solvent respectively, supposing the activity coefficient $\gamma_A = \gamma_B = 1$. $E_{\mathrm{b.diff}}$ is the energy barrier for

the diffusion process and f_f the fundamental frequency (see equation 1.23). The energy barrier for a dissolution process and a precipitation process is the same, and the latter does not change with the number of neighbours. The results of this model matches a normal TST behaviour (see section 1.2.1).

As we will see in chapter 2, the experimental sigmoid function arises by having different energy barriers for dissolution and precipitation and doing this last one neighbourhood dependent. Moreover, the study done for quartz in chapter 5 questions the validity of the 'flickering-bond' model (equation 1.43).

Two dimensional lattice model

Developed by Bandstra and Brantley shortly after [112], this simplification of the kinetic model consist of two terms, dissolution and precipitation, and it is applied to a simple 2D Kossel crystal. The time evolution is obtained using an Ising model [113] where each site, occupied or empty, has a rate to change its state. Both rates $\dot{r}'_D$ and $\dot{r}'_P$ are normalized to an arbitrary time instead of seconds.

$$\dot{r}'_D = \left(1 - \frac{n}{4}\right)^{\kappa} \tag{1.48}$$

$$\dot{r}'_P = \left(\frac{n}{4}\right)^{\beta} \cdot \exp\left(\Delta G + \Omega\right) \tag{1.49}$$

where κ and β are adjustable parameters, and Ω is a constant whose value is chosen to yield zero average net dissolution when $\Delta G = 0$. Despite its simplicity the model highlights the importance of making a difference in precipitation energy to reveal the sigmoid form with ΔG.

Analytical model

Another simplification of the kinetic model to describe dissolution was made by Nicoleau and Bertolim [114]. As it is an analytical model, there is no need of additional computational tools to get the time evolution of the system.

The model is based on the dissolution provoked by the step retreat of dislocations and it was applied to a spherical Kossel crystal. The results obtained, though extensible to other minerals,

were applied to the specific case of the alite dissolution to explain the calorimetric curve of cement hydration.

The dissolution rate $\dot{r}_{\mathrm{D}}$, with arbitrary time units, is as follows.

$$\dot{r}_{\mathrm{D}} = \frac{1}{i} \sum_{j=0}^{m} A_{j,\mathrm{E}_j} \cdot a_0 \cdot h \tag{1.50}$$

$$A_{j,\mathrm{E}_j} = A_{j,\mathrm{E}_j-1} \left(1 - \frac{1}{\Omega_j}\right) + 1 \tag{1.51}$$

Where A_{j,E_j} is the number of elements or cells E dissolved from layer j in a given i time step, Ω_j its remaining number of elements, and a_0 and h are respectively, the surface area of an elementary cell and the height of one layer.

It is highlighted that the coalescence of dislocations along with the progressive reduction of grain size causes a decrease in the net dissolution. As we will see in chapter 6, although the grain size does cause a reduction, the dislocation coalescence does not.

1.5 Conclusions and outlook

Both experiments and modeling work together to bridge the gap that divide them and understand the processes taking place at nanoscale during the mineral dissolution. Gibbs free energy, temperature, diffusion, pH, size or dislocations are some of the main parameters influencing the dissolution. Experimentalists have focused on the improvement of experimental devices to get more accuracy and resolution to isolate each contribution to dissolution. On the other side, modelers have worked on understanding, based on the experimental results, the underlying processes. The BCF model, the stepwave model, and the kinetic model are the three main theories developed to explain the experimental results. The development of the TST, along with *ab initio* calculations and upscaling methods like KMC have allowed the kinetic model to explain experimental results that the BCF and stepwave models cannot.

In the last years, the experiments have focused on minimizing the effect of diffusion and obtaining dissolution rate spectra characteristic of each mineral and even crystallographic faces, and studies of the dissolution rate with the concentration, surface topography, cations and anions on the solvent, and other biological influences, all over in a wider temperature range. The computational work has focused, on one hand, on continuing to extend the catalogue of possible reactions by *ab initio* methods on various minerals, and on the other hand, on extending and improving the tools available to take the results to larger scales.

This chapter provides the basis for understanding the work carried out in the following chapters, which consists mainly on the extension and application of the kinetic model for the study of mineral dissolution.

Chapter 2: Dissolution Model

2.1 Introduction

As we have seen in the previous chapter, many models were proposed to reproduce the dissolution of minerals as a function of their composition, topography and ΔG. One of them, the kinetic model proposed by Lasaga and Luttge, is likely the most successful one, since it is able to explain the dissolution process from a fundamental scale (see section 1.4.5.3). In their work they defined the general considerations that would have to be taken to describe the dissolution of minerals, to later apply them to specific cases.

Related studies using this model have captured the inherent topographies associated to the dissolution mechanisms [10,16,106,115], dislocations [10,115], grain sizes [61], particular mineral compositions [16,106], and even it has allowed to reproduce the experimentally observed pulsating dissolution frequency at the nanoscale [116].

However, some of the proposed approximations taken are not able to mimic the complexity of dissolution processes near equilibrium conditions, and the model does not reproduce the sigmoid dependence of the dissolution rate with the Gibbs free energy and its intrinsic mechanisms (see section 1.2.1). Therefore, most of these studies are made at far from equilibrium conditions [16,106] where precipitation processes are very unlikely to happen.

In this chapter we will discuss the necessary considerations to extend the kinetic model proposed by Lasaga and Luttge [81] to reproduce the dissolution rate dependence with the Gibbs free energy. This extension is the main result of this thesis, and subsequent chapter shows side results of its application in specific systems. In this chapter the model is tested in a simple Kossel crystal, but as we will see later, it can be extended to specific studies of minerals, as we have done for quartz in the chapter 5.

The chapter is organized as follows. First, after presenting the model, the considerations taken to apply it to a system are explained. Second, the net dissolution rate dependence with its main parameters, i.e. the dissolution and precipitation energy barriers, is explored. Third, these microscopic parameters are related to macroscopic parameters, like the dissolution onset ΔG_{crit}, the Gibbs free energy in which the mechanism III is produced $\Delta G_{\text{m.III}}$, or the global activation energy E_{a}. Fourth, experimental data for several minerals is fitted, finding a reasonably good agreement in spite of the structural limits of using a simple Kossel crystal. Finally, side results such as the extension to a diamond like mineral, dissolution rate dependence with dislocation density, or initial irregularities over the surface are studied.

2.2 Extension of the Lasaga and Luttge Kinetic Model

KMC models based on Transition State Theory (TST) consider that the rate of a dissolution event, r'_{D}, depends on its dissolution reaction energy barrier E_{D} and the frequency to overcome it (equations 1.26 and 1.44). As usual approximations, it is considered that the ion activities $\gamma = 1$ and that the entropy does not change between states $\Delta S^{\ddagger} = 0$, that is, the partition functions of initial and transition state are the same $q^{\ddagger} = q$ [10, 16, 61, 106, 115, 116]. Besides, the dissolution energy barrier depends linearly on the first neighbours $E_{\text{D}} = n \cdot E_{\text{da}}$ by considering a Kossel crystal system (see equation 1.37). E_{da} is the energy barrier needed to dissolve an atom with only 1 bond, an adatom (see figure 1.11). Same considerations are taken in our model. By simply considering the precipitation effect symmetrically to the dissolution and the local Gibbs free energy ΔG^{*}, the experimental sigmoid function of the dissolution rate dependence with ΔG and the three mechanisms can be successfully reproduced (see figure 1.2).

$$r'_{\text{D}} = \frac{k_{\text{B}} \cdot T}{h} \cdot \exp\left(-\frac{n \cdot E_{\text{da}}}{k_{\text{B}} \cdot T}\right) \tag{2.1}$$

$$r'_{\text{P}} = \frac{k_{\text{B}} \cdot T}{h} \cdot \exp\left(-\frac{n \cdot E_{\text{pa}} - \Delta G^{*}}{k_{\text{B}} \cdot T}\right) \tag{2.2}$$

With this model both dissolution and precipitation are taken into account, and together they describe the net dissolution process. Dissolution is assumed to be intrinsic for a mineral and its topography, via E_{da} and n respectively, and it does not depend on ΔG^*. Equation 2.2 accounts for precipitation phenomenon. The rate of a precipitation process decreases with the solute concentration by means of ΔG^*, and similarly to the dissolution rate equation, the nature of the mineral and topography is considered via E_{pa} and n.

Two aspects of the model must be remarked. First, as expected, when the system is very far from equilibrium ($\Delta G^* \to -\infty$) the precipitation rate becomes negligible and the proposed model is then reduced to the dissolution term. Second, if the net dissolution rate $r'_{\mathrm{D}} - r'_{\mathrm{P}}$ is calculated and E_{D} and E_{P} are equal and constant (no n dependence is considered), the general expression for the normal TST is recovered (see equation 1.29).

This model, along with a code to easily define systems of minerals will be used in chapter 3 to systematically get results of their dissolution.

2.2.1 Relating local ΔG^* and macroscopic ΔG

From the previous chapter we know the effect of the diffusivity on the Gibbs free energy (see section 1.2.2). A low diffusivity can produce a change in the local concentration over the mineral surface, decreasing its dissolution rate. Besides, there is another effect involved that may also change it; the charge. Usually during the dissolution there is a potential gradient between the surface and the closest released ions. The layer where this happen is named electrical double layer or Stern layer (see figure 2.1). Although the experiments manage to remove all the diffusivity effect, the concentration gradient because of the charge is inevitable due to the close range interaction.

We do not know what the concentration in this layer is, but we do know that in this layer the dissolution and precipitation have to be equal when the system is at equilibrium, that is, $r'_{\mathrm{D}} = r'_{\mathrm{P}}$ when macroscopic $\Delta G = 0$ (see equations 2.1 and 2.2). For that, the dissolution and precipitation rate for a kink site is taken as a reference for the mineral dissolution [3, 6, 108] (see figure 1.11). It is a peculiar position: independently of the mineral composition a kink atom is the one which dissolves the most.

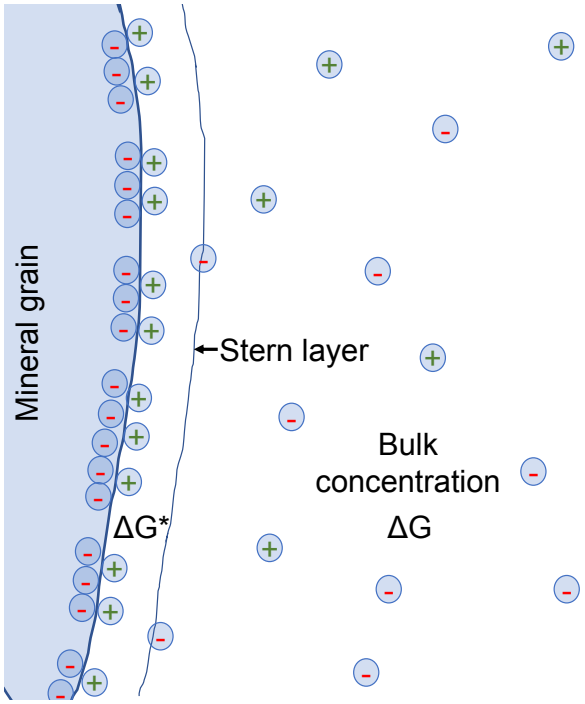

Figure 2.1: **Stern layer**. Schematic representation.

Besides, it has always half the number of bonds that in the bulk and therefore its energy is half, and it is observed experimentally that the sublimation energy of a crystal corresponds to the change of the internal energy when detaching it [3, 6, 108]. With this site as reference, the local ΔG^* in the Stern layer and the macroscopic ΔG are related by the following expression [108, 112]:

$$\Delta G = (\Delta G^* - b) \cdot n_{\mathrm{k}} \tag{2.3}$$

where n_{k} is the coordination of a kink site; in a Kossel crystal $n_{\mathrm{k}} = 3$. The constant b is the deviation in energy related to the concentration difference. It can be determined by considering that equilibrium is reached during dissolution when no kink atoms can dissolve $r'_{\mathrm{D}} = r'_{\mathrm{P}}$, and hence the macroscopic $\Delta G = 0$:

$$r'_{\mathrm{D}}(n = n_{\mathrm{k}}) = r'_{\mathrm{P}}(n = n_{\mathrm{k}}) \rightarrow \Delta G = 0 \tag{2.4}$$

Expressing the result in $k_{\mathrm{B}}T$ units, the constant b is:

$$b = n_k \cdot (E_{pa} - E_{da}) \tag{2.5}$$

or by considering equation 1.2:

$$b = \ln \beta^* - \frac{1}{n_k} \cdot \ln \beta \tag{2.6}$$

Therefore, b constant can be seen as the superficial change of saturation index β^* due to the mineral susceptibility to dissolution or precipitation.

2.2.2 Differences with the previous kinetic model

The differences between this model, and the one proposed by Lasaga and Luttge (see section 1.4.5.3) are basically two. On the one hand, the precipitation term has different energy barrier value and it is neighbour dependent (see equations 1.45 and 1.46 and equation 2.2). On the other hand the effect of the Stern layer has been introduced as a differentiation between ΔG and ΔG^* with the b parameter. Nevertheless, they do consider atom diffusion where an atom can move randomly over the mineral surface (do not confuse with diffusion within the solvent)(see equation 1.47). As we will see, it is not necessary to explain the dissolution mechanisms, yet it can be implemented in future studies.

2.3 Application of the Proposed Model

In the next step the proposed model is applied to a Kossel crystal system with the KMC method to check its validity. The system under study consists of a Kossel crystal with 240 x 240 x 8 sites for a total of $\sim$ 460800, with periodic boundary conditions (PBC). With a typical distance between atoms of 2.5 Å [117], the system has a size of $\sim$ 60 x 60 x 2 nm. Mineral topography and surface are key factors in the dissolution mechanisms. To simulate a mineral as real as possible all the different topographic defects showed in a Kossel crystal (see figure 1.11) have been included. On the surface, a random number of terraces, vacancies, and adatoms have been introduced.

The system has two dislocations. This equates, for the system size, to a dislocation density of $\sim 5.5 \cdot 10^{14}$ m^{-2}. This value lies into the known dislocation density range for minerals: 10^{10} - 10^{14} m^{-2} [62]. We have considered the simplest case: the $\{001\}$ plane with perpendicular dislocations as it can be appreciated in figure 1.11, though results are extensible to $\{100\}$ and $\{010\}$ planes since they are identical. Only surface atoms are supposed to react since they are in contact with the solvent, therefore there are no possible events for a bulk atom. A KMC home code, described in detail in chapter 3, has been developed in C++11 language to perform the simulations.

The next step is to set the values of the model parameters. The activation energy E_a for a dissolution process of a typical mineral lies in the range of $30 \lesssim E_a \lesssim 100$ kJ mol^{-1} [1]. Expressing this in $k_B T$ units ($k_B T = 2.494$ kJ mol^{-1} at 300 K), $12 \lesssim E_a \lesssim 40$. In the model E_D represents the bond breaking energy barrier, which in a Kossel crystal with an average of three broken bonds during a dissolution event, should correspond to $E_a/3$. Hence, simulations with $E_{da} = 4.0,\ 7.0,\ 9.0,\ 12.0$ $k_B T$ units have been done. Several ΔG values covering the three mechanism zones have been taken starting from $\Delta G = 0$ and with finer focus on the ΔG_{crit} onset. For the energy barrier of precipitation events a value of $E_{pa} = 1.0\ k_B T$ units is taken. The presented results are the average of 5 simulations for each condition unless the contrary is specified.

2.3.1 Methodology for accelerating simulations close to equilibrium with KMC

As we discussed in the section 1.4.3, a major problem in simulations close to equilibrium conditions is that atoms undergo dissolution and precipitation reactions rapidly. These fast events happen continuously, inducing an exponential increase on the use of computing resources and blocking the simulation. Therefore a methodology to unstuck it is necessary, skipping repeating and computing consuming processes. There are several algorithms to avoid such issue [103, 105, 118], yet a new one has been used based on Poisson processes statistics. For an atom attempting to dissolve, it is possible to do an estimation of the probability for that atom to truly leave the mineral taking into account both dissolution and precipitation rates. System time increment is then recalculated based on that

probability and plenty of simulation time is saved depending on ΔG value and mineral dissolution energy barrier. While far from equilibrium conditions this does not make any difference, close to it, in minerals with high energy barrier, simulations are about 10^4 times faster.

Imagine that we have an atom trying to dissolve, but at close to equilibrium conditions with high concentration, it may reprecipitate. Its dissolution rate gives us its characteristic time for the process to happen $t_{\mathrm{D}} = 1/r'_{\mathrm{D}}$. In the same way, its characteristic precipitation time is given by $t_{\mathrm{P}} = 1/r'_{\mathrm{P}}$. We can compute the effective time for the dissolution process to happen knowing that the dissolution and precipitation events are Poisson processes (see section 1.4.3.2).

The effective time $t_{\mathrm{D_{eff}}}$ needed for the atom to leave with certain probability is:

$$t_{\mathrm{D_{eff}}} = -\ln(1-P)\cdot t_{\mathrm{D}} \tag{2.7}$$

where P is the probability of the event to happen. To ensure that the $t_{\mathrm{D_{eff}}}$ is captured, a P threshold value of 99.9% was used. Given the characteristic time of precipitation t_{P}, we can estimate the effective probability P' for an atom to dissolve.

$$P' = \exp\left(-\frac{t_{\mathrm{D_{eff}}}}{t_{\mathrm{P}}}\right) \tag{2.8}$$

If $t_{\mathrm{P}} << t_{\mathrm{D_{eff}}}$, the exponent goes to $-\infty$ and $P' = 0$. It is impossible for an atom to dissolve since it always comes back when it tries. The other way around, if $t_{\mathrm{P}} >> t_{\mathrm{D_{eff}}}$, $P' = 1$. Every single atom trying to dissolve, manages it. The net dissolution rate r'_{net} can be expressed as the product of this probability P' and the dissolution rate r'_{D} to finally reach:

$$r'_{\mathrm{net}} = r'_{\mathrm{D}}\cdot\exp\left(\frac{\ln(1-P)\cdot r'_{\mathrm{P}}}{r'_{\mathrm{D}}}\right) \tag{2.9}$$

We check from this function that at far from equilibrium $\Delta G, \Delta G^* \to -\infty$, thus $r'_{\mathrm{P}} = 0$ and $r'_{\mathrm{net}} = r'_{\mathrm{D}}$. When $\Delta G = 0$, $r'_{\mathrm{net}} = 0$ by definition. This function may not have a TST shape. It depends on the specific system, its coordination, and how this coordination evolves over time. KMC method

helps us to obtain this time evolution.

2.4 Results

2.4.1 Dissolution rate as a function of ΔG

First, the effect of E_D on the dissolution rate as a function of ΔG is tested. Simulations with $E_{da} = 4.0,\ 7.0,\ 9.0,\ 12.0\ k_B T$ units are shown in figure 2.2a. It is remarkable that the curves have the sigmoidal shape found experimentally. To the best of our knowledge this is the first model that reproduces the whole ΔG dependence and captures the inherent mechanism and its topography. Close to $\Delta G = 0$, in mechanism I region, very low dissolution takes place since only adatoms and terraces are dissolved. Then dissolution slowly increases until ΔG is high enough to allow pit opening or mechanism II, leading to a sharp increase of the rate. Finally a steady dissolution rate is obtained at very high ΔG values, when mechanism III governs dissolution if E_{da} is low enough. It is important to notice that the relationship between ΔG_{crit} and E_{da} matches what is seen in experiments; the higher the E_{da}, the lower the ΔG_{crit}. Another point of agreement with experiments is the maximum dissolution rate far from equilibrium: the higher the E_{da}, the lower the rate.

In figure 2.2a the cases $E_{da} = 7.0\ k_B T$ with $E_{pa} = 7.0\ k_B T$ and $E_{pa} = 10.0\ k_B T$ are studied to show how E_{pa} affects mechanisms and to underline that the TST curve can also be reproduced by the model. Two interesting phenomena should be emphasized. On one hand, mechanisms II and III can take place very close to equilibrium conditions. On the other hand, if E_{pa} is significantly higher than E_{da}, spontaneous vacancies can be created and pit opening is more favourable than adatom removal, provoking very irregular patterns. To our knowledge, this dissolution mechanism has not been observed before and should deserve experimental validation.

In figure 2.2b dissolution patterns are represented in the three differentiated zones for the four cases in figure 2.2a. First, at high dissolution energy barrier, $E_{da} = 12.0\ k_B T$ and $E_{da} = 9.0\ k_B T$, two dissolution mechanisms are easily differentiated. Close to equilibrium only terraces and adatoms are dissolved (mechanism I). Once ΔG_{crit} is reached, dissolution is produced almost exclusively

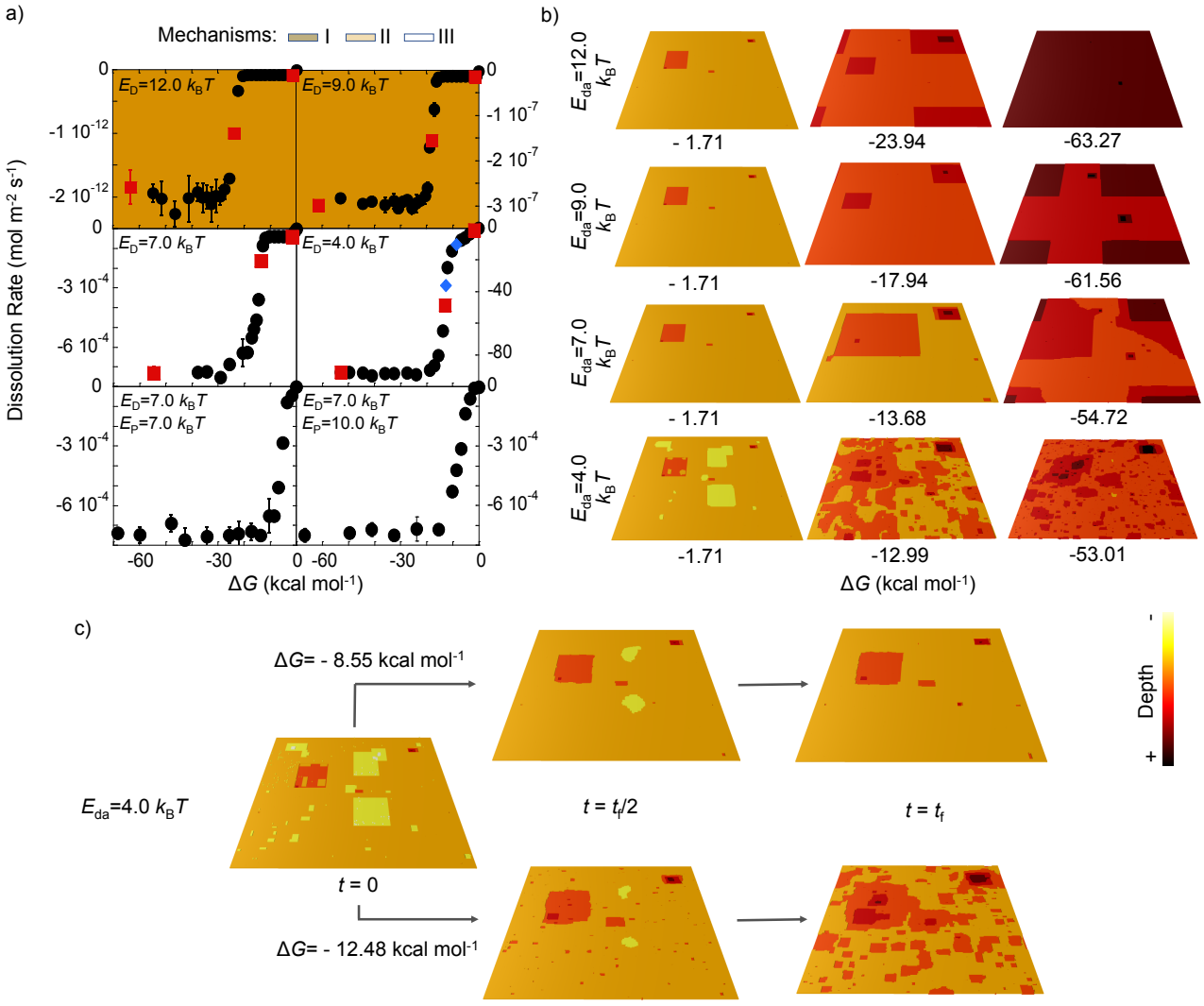

Figure 2.2: **Dissolution rate versus Gibbs free energy** (ΔG). a) Kossel crystal with different precipitation and dissolution energies. Points in red and blue are represented in panel b and c respectively. Values are the average of 5 simulations. b) Surfaces at a given time t_f. c) Time evolution of the surface. The visual representation is done using OVITO program. [8].

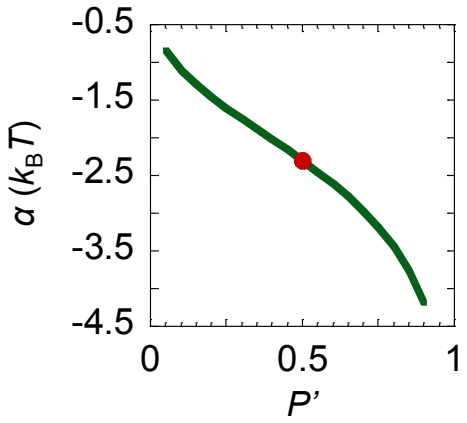

Figure 2.3: **Dispersion in α depending on P'.**

from step retreat (mechanism II). Mechanism III does not exist in these cases. Secondly, looking at minerals with low dissolution energy barrier $E_{\mathrm{da}} = 7.0\ k_{\mathrm{B}}T$ and $E_{\mathrm{da}} = 4.0\ k_{\mathrm{B}}T$, it can be seen that, like in the previous case, at close to equilibrium conditions adatoms and terraces are the only ones which are removed. Once ΔG_{crit} is reached pits start to open. But shortly after ΔG_{crit} value, spontaneous opening of surface (mechanism III) happens, the more the farther from equilibrium. At far from equilibrium conditions, differences in energy between more and less coordinated atoms are not high enough to prevent them to dissolve almost randomly, so very irregular patterns appear.

The difference between mechanisms becomes more evident the lower the E_{da} is. Therefore, for a better sighting, in figure 2.2c the dissolution pattern at three different times in the onset between mechanism II and mechanism III for a $E_{\mathrm{da}} = 4.0\ k_{\mathrm{B}}T$ mineral is shown. In minerals with low dissolution energy barrier, in addition to the contribution to dissolution rate of the dislocation opening, there is a small contribution from mechanism III.

2.4.2 Calculation of ΔG_{crit} and $\Delta G_{\mathrm{m.III}}$ as a function of E_{da} and E_{pa}

Dislocations are key structural features for the mineral dissolution. In this work we have validated that in all studied cases dislocations produce the onset in the dissolution rate at ΔG_{crit} [10,20,50,119]. Once the system is able to remove an atom close to dislocations, that is, with 4 neighbours in a Kossel crystal, the dissolution probability of the atoms in that layer increases due to the appearance

of 3-coordinated kink site atoms. It is possible to analytically relate the microscopic variables E_{da} and E_{pa} used in this model with the macroscopic ΔG_{crit}.

With the equations 2.9, 2.1 and 2.2 above, we calculate the net dissolution for an atom close to a dislocation, with $n_D = 4$, and relate it to the local ΔG^*_{crit} in $k_B T$ units.

$$\Delta G^*_{crit} = \alpha - n_D \cdot \left(E_{da} - E_{pa}\right) \tag{2.10}$$

$$\alpha = \ln\left(\frac{\ln P'}{\ln(1-P)}\right) \tag{2.11}$$

To consider a low P' value implies that a small proportion of the dislocations attempting to open finally manage to do it, and therefore, the expression reports the beginning of the ΔG_{crit} onset. Nevertheless, a clearer choice is to obtain the medium height value for a better sighting. For that, it has been considered that half of the dislocations are able to open, meaning $P' = 0.5$. Figure 2.3 shows the α value dispersion which allows to report an error of such an approximation. Final value considered is $\alpha = -2.3 \pm 0.9\ k_B T$, which corresponds to $P' = 0.5$ and $P = 0.999$.

Using equation 2.3, the relation of ΔG^*_{crit} with macroscopic ΔG_{crit} is ($k_B T$ units):

$$\Delta G_{crit} \approx \left(\alpha + (n_k - n_D) \cdot (E_{da} - E_{pa})\right) \cdot n_k \tag{2.12}$$

Equation 2.12 allows to determine the theoretical ΔG_{crit} even in conditions where E_{pa} is higher than E_{da} and the onset is produced at positive ΔG. The accuracy of Equation 2.12 is checked in table 2.1. There is an excellent match between the ΔG_{crit} obtained from simulations and the one analytically derived when the transition between mechanism I and II is given at negative ΔG.

We can generalize equation 2.12 to any coordination in a Kossel crystal to get, for example, the ΔG value when atoms with coordination $n_s = 5$ on the surface start to dissolve and mechanism III occurs ($k_B T$ units):

E_{da}	E_{pa}	Simulation ΔG_{crit}(kcal mol^{-1})	Analytical ΔG_{crit} (kcal mol^{-1})
12.0	1.0	-24	-23.8
9.0	1.0	-18	-18.4
7.0	1.0	-15	-14.9
7.0	7.0	-2	-4.1
7.0	10.0	-7	1.3
4.0	1.0	-13	-9.5

Table 2.1: **Validation of equation 2.12**. ΔG_{crit} is obtained by applying the Equation 2.18, which is later explained, to figure 2.2b. E_{da} and E_{pa} are in $k_B T$ units. Error in analytical ΔG_{crit} is $\pm$ 1.6 kcal mol^{-1}.

$$\Delta G_n \approx \left(\alpha + (n_k - n) \cdot (E_{da} - E_{pa}) + \ln\left(\frac{f_D}{f_P}\right) \right) \cdot n_k \tag{2.13}$$

Where f_D and f_P have been introduced to account for a different pre-exponential factor between dissolution and precipitation events (see equations 2.1 and 2.2). Note that equation 2.13 tells us where the mechanism III happens if it is not overshadowed by mechanism II. Mechanisms II and III are competing mechanisms and the former usually goes first hiding the other. By the time a surface atom is able to dissolve, it is already dissolved by the step retreat provoked by the opening of a dislocation. From the dislocation density we can do an estimation of the conditions where the mechanism III is produced, considering that the rate for any atom in the surface with coordination n_S has to be higher, or in the same magnitude, than an atom close to a dislocation with n_D. In a perfect surface, very few atoms (4 in a Kossel crystal) surround a dislocation of radius ε (m). The number of atoms in the surface is much larger, and can be calculated by the the dislocation density ρ (m^{-2}) and the distance between atoms d (m) of the mineral. The condition to accomplish is (see equation 2.9):

$$r_{net}(n = n_S) \cdot \frac{1}{d^2 \cdot \rho} \geq r_{net}(n = n_D) \cdot \frac{2 \cdot \Pi \cdot \varepsilon}{d} \tag{2.14}$$

to finally reach ($k_B T$ units):

E_{da}	E_{pa}	Condition	Simulation $\Delta G_{m.III}$(kcal mol^{-1})	Analytical $\Delta G_{m.III}$ (kcal mol^{-1})
12.0	1.0	$E_{da} \leq 8.9$	–	−43.5
9.0	1.0	$E_{da} \leq 8.9$	–	−32.8
7.0	1.0	$E_{da} \leq 8.9$	−25	−25.6
7.0	7.0	$E_{da} \leq 9.6$	−6	−4.1
7.0	10.0	$E_{da} \leq 22.8$	0	6.6
4.0	1.0	$E_{da} \leq 8.9$	−15	−14.9

Table 2.2: **Validation of equations 2.12**. The condition to meet is equation 2.16. Simulation $\Delta G_{m.III}$ is obtained visually from simulations. E_{da} and E_{pa} are in $k_B T$ units. Error in analytical $\Delta G_{m.III}$ is $\pm$ 1.6 kcal mol^{-1}.

$$\Delta G_{m.III} \approx \left(\alpha + (n_k - n_S) \cdot (E_{da} - E_{pa}) + \ln\left(\frac{f_D}{f_P}\right) \right) \cdot n_k \tag{2.15}$$

if

$$\ln\left(\frac{1}{2 \cdot \Pi \cdot \varepsilon \cdot d \cdot \rho}\right) \geq (n_S - n_D) \cdot E_{da} - \ln\left(\frac{1}{2}\right) + \ln\left(\frac{1}{2}\right) \cdot \exp\left((n_S - n_D) \cdot (E_{da} - E_{pa})\right) \tag{2.16}$$

Note that the higher the E_{da} and the dislocation density, the more difficult for a mineral to present mechanism III. Nevertheless, if $E_{pa} \sim E_{da}$, the last right term gains importance and minerals with high E_{da} can show mechanism III.

The validity of equations 2.15 and 2.16 is checked in table 2.2 for our simulations. Note that they report the half height value, and colored regions in figure 2.2a reports the beginning of the mechanism. If we take the middle point between the beginning of mechanism III and the point when the plateau is reached, the equations show an excellent match. Moreover, they allow us to define $\Delta G_{m.III}$ even when it is produced at positive ΔG.

When E_{pa} is significantly greater than E_{da}, mechanism III occurs before mechanism II, and even before than mechanism I. Up to our knowledge this dissolution mechanism has not been experimentally reported for any mineral. One possible explanation is that such hypothetical minerals would not be found in nature, as it would be very difficult for them to precipitate into a solid. A

clue that validates this hypothesis is the case of alite. This artificial and metastable mineral is one of the essential components of cement. The fact that it presents spontaneous pit opening at very close to equilibrium conditions indicates that its E_P and E_D are close in value. Other possible clue is the dissolution patterns observed by Laanait et al. [69] in Calcite-water interfaces where they would be decreasing E_D artificially with X-ray. Though at present we cannot prove it and more experimental validation is needed.

2.4.2.1 Comparison with the BCF model

In section 1.4.5.1 we have described the BCF model. It relates the $\Delta G'_{crit}$ with macroscopic parameters like the shear modulus and Poisson ratio (see equation 1.39). Besides it also relates the $\Delta G'_{m.III}$ with same macroscopic parameters along with the concentration in the solvent (see equation 1.40).

In our model, both parameters $\Delta G'_{crit}$ and $\Delta G'_{m.III}$ can be approximately obtained by changing the α value to $\sim -1\ k_B T$ units (see figure 2.3). As we can see, $\Delta G'_{crit}$ and $\Delta G'_{m.III}$ are only dependent of E_D and E_P. Nevertheless, E_D and E_P are related to the macroscopic parameters along with the interaction with the solvent, though this relation may be very complex. Therefore, the kinetic model is a generalization of the BCF model and represents a different approach, and in principle more accurate, to describe mineral dissolution. The main disadvantage of the kinetic model is that a complete and precise study of E_D and E_P in the proper mineral structure and conditions is required with *ab initio* calculations to get accurate results.

2.4.3 Proposed empirical fitting

The sequential activation with ΔG of atoms from lower to higher coordination contributes to the overall dissolution rate. Based on the major contributions, an empirical fitting function that differs from the previously proposed ones in the literature [3, 9, 10] is shown (see equations 1.30, 1.31 and 1.41 and 1.42). The fitting function adds two logistic function terms [120] to the TST expression reporting the activation of mechanism II at ΔG_{crit} and mechanism III at $\Delta G_{m.III}$.

$$
\begin{aligned}
r_{\mathrm{D}} =& A \cdot \left(1 - \exp\left(\frac{\Delta G}{k_{\mathrm{B}} \cdot T}\right)\right) + \\
& B \cdot \left(1 - \frac{1}{1 + \exp(D \cdot (-\Delta G + \Delta G_{\mathrm{crit}}))}\right) + \\
& C \cdot \left(1 - \frac{1}{1 + \exp(E \cdot (-\Delta G + \Delta G_{\mathrm{m.III}}))}\right)
\end{aligned}
\tag{2.17}
$$

where A, B and C are the limiting dissolution rates for each mechanism, I, II and III respectively. D and E are fitting parameters related to E_{D} and topography. To reduce fitting parameters in most cases we can remove the third term of mechanism III since it is very small comparing to the mechanism II or it does not exist. For example, for the cases studied in figure 2.2, only $E_{\mathrm{da}} = 7$, $E_{\mathrm{pa}} = 1\ k_{\mathrm{B}}T$ units case shows a small contribution at ~ -18 kcal.mol^{-1}. $E_{\mathrm{da}} = 4$ and $E_{\mathrm{pa}} = 1$ case also shows mechanism III, but it is so close to mechanism II that they overlap.

$$
\begin{aligned}
r_{\mathrm{D}} =& A \cdot \left(1 - \exp\left(\frac{\Delta G}{k_{\mathrm{B}} \cdot T}\right)\right) + \\
& B \cdot \left(1 - \frac{1}{1 + \exp(D \cdot (-\Delta G + \Delta G_{\mathrm{crit}}))}\right)
\end{aligned}
\tag{2.18}
$$

Note that both this empirical equation and equation 2.12 report ΔG_{crit} at the middle height value. We have used equation 2.18 to fit ΔG_{crit} for the simulations from figure 2.2a in table 2.1 by fixing A and B values.

2.4.4 Relationship between E_{D} and E_{a}

In this section we are going to relate the dissolution energy barrier with the activation energy (see section 1.2.3).

In an idealized simulation model, the activation energy E_{a} can be written as $E_{\mathrm{a}} = n_{\mathrm{k}} \cdot E_{\mathrm{da}}$ because it is observed experimentally that the sublimation energy of a crystal corresponds to the change of internal energy when detaching a kink atom. Nevertheless, as it is checked below, this relation is not

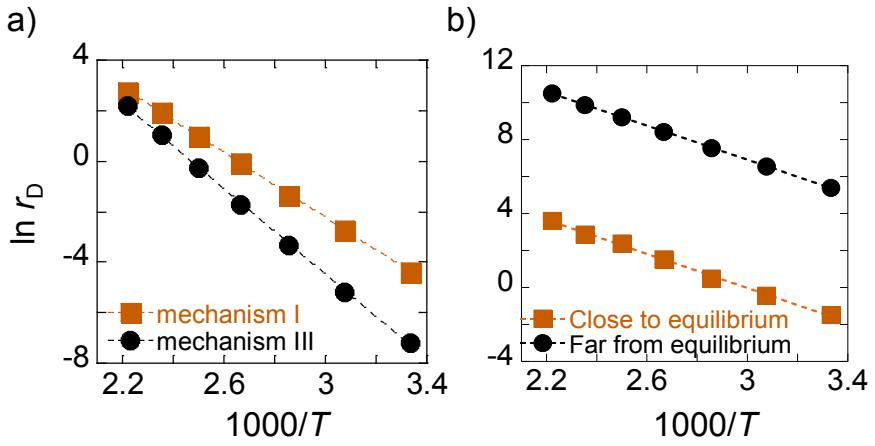

Figure 2.4: **Activation energy**. a) Kossel crystal of $E_{da} = 7.0\ k_B T$ and $E_{pa} = 1.0\ k_B T$ units. b) Same values for a diamond like mineral. Points in black represent far from equilibrium conditions. Points in orange represent close to equilibrium conditions. Error is smaller than the size of the points. Arrhenius fitting parameters are represented in table 2.3.

true at the whole ΔG range [81]. Thus, the real link between macroscopic E_a and microscopic E_{da} is explored to compare with experimental data.

Experimental studies usually report a single E_a, usually corresponding to far from equilibrium conditions in powder samples. Nevertheless, in an infinite ideal surface system E_a actually depends on the dissolution mechanism. In the mechanism I zone, dissolution is driven by removal of kink atoms in terraces. In contrast, in mechanisms II/III zones dissolution is driven by step retreat. Therefore, microscopically it is expected that $E_{a\,m.I} \approx n_k \cdot E_{da}$ and $E_{a\,m.II/III} \approx n_d \cdot E_{da}$, where n_k and n_d are 3 and 4 respectively for a Kossel crystal.

In order to verify such relationship, Arrhenius equation has been used to fit the natural logarithm of the dissolution rate, $\ln r_D$, as a function of $1/T$ for fixed ΔG conditions corresponding to mechanisms I and III. For that, values of 7 $k_B T$ and 1 $k_B T$ units have been chosen for E_{da} and E_{pa} respectively. For the mechanism III, the Kossel crystal described before has been used, and the dissolution rate at each T is taken as the plateau value at far from equilibrium conditions. However, to study mechanism I, a limiting value of the dissolution rate is not reached. For this case, the beginning of the onset at $\Delta G'_{crit}$ represents a good reference point since no contributions from other mechanisms are involved. In addition, the Kossel crystal topography has been modified for a better quantification of the rate. As

		Kossel crystal	Diamond like system
mech. III / f.f.e	$\ln A'$	20.98 ± 0.19	20.69 ± 0.05
	$\frac{E_a}{E_{da}}$	4.0	2.2
	E_a	70.5 ± 0.6 kJ mol^{-1}	38.0 ± 0.2 kJ mol^{-1}
mech. I / c.e	$\ln A'$	17.15 ± 0.06	13.8 ± 0.3
	$\frac{E_a}{E_{da}}$	3.1	2.2
	E_a	53.73 ± 0.17 kJ mol^{-1}	38.3 ± 0.9 kJ mol^{-1}

Table 2.3: **Activation energy and fitting parameters**. Reported values in figure 2.4 for both, a Kossel crystal in mechanisms III and I, and a four coordinated diamond like mineral at far from equilibrium (f.f.e) and close to equilibrium conditions (c.e). The latter is studied in section 2.4.8.

only terrace dissolution is the governing mechanism, a surface with a big terrace of 8 sites high has been constructed without any other surface defect.

As it can be seen in figure 2.4a and table 2.3, there is good linear correlation of the dissolution rate logarithm with the inverse of temperature for both mechanisms, which indicates that the systems are following an Arrhenius process as expected. An important consequence is that the expected values of E_a as a function of E_{da} are obtained ($E_{a\ m.I} = 3.1 \cdot E_{da}$ and $E_{a\ m.II/III} = 4.0 \cdot E_{da}$). Therefore, the macroscopic dissolution activation energy can be obtained directly from the computed dissolution reaction energy in any ΔG conditions.

Note that, although the activation energy may change with ΔG, the consideration of taking kink atoms as reference point to define $\Delta G = 0$ is still valid since most atoms which dissolve are in kink sites along all ΔG range.

2.4.5 Comparison with experimental dissolution rates

The next target is to apply the proposed model to describe the experimentally reported dissolution for several minerals: albite [9, 10], smectite ($(Na,Ca)_{0.33}(Al,Mg)_2(Si_4O_{10})(OH)_2 \cdot nH_2O$) [10, 11], alite [12], labradorite [10, 13], K-feldspar [14] and belite [12]. Table 2.4 contains the obtained values for the model parameters in equations 2.1 and 2.2, their activation energies, and the ΔG_{crit}.

The initial values for the simulations have been set as follows. First the ΔG_{crit} value is obtained from the empirical equation 2.18. Second, a guess E_{da} value is chosen based on the dissolution rate limit value at far from equilibrium conditions. Finally, E_{pa} is calculated from equation 2.12. With these initial values simulations are run and the parameters are adjusted *ad-hoc* to obtain the best possible fit according to the regression coefficient between the simulation results and an empirical fit for the experimental data.

The experimental and computed dissolution rates as a function of ΔG are shown in figure 2.5. It can be first noticed that the sigmoidal shape of the mineral dissolution rate as a function of ΔG can be reproduced with the presented model. Furthermore, equation 2.12 provides a ΔG_{crit} in good agreement with the experimental and computed values and helps to define the onset in cases in which transition between mechanism I and II is not so clear, such as the case of K-feldspar.

The dissolution and precipitation energies E_{da} and E_{pa}, the activation energies in mechanism I and II regions, and the ΔG_{crit} obtained from the fitting are presented in table 2.4, together with experimental dissolution activation energies. All the obtained values are in reasonable agreement with the experiments, yet the experimental dissolution activation energies are consistently overestimated by nearly a factor 2 for all minerals. Clearly, using a Kossel crystal with the same topography for all the studied minerals will necessary lead to qualitative results. Other discrepancies in the values can arise from considering a ΔG value independent of ion activities, the unknown initial surface conditions, or the homogeneous pre-exponential value chosen for the study.

2.4.6 Dissolution rate dependence with dislocation density

In section 1.2.5 we have discussed about the experimental reported influence of the dislocation density in the dissolution rate. Experiments in general report hardly any influence by increasing 4 orders of magnitude the dislocation density.

Therefore, we have done simulations in our Kossel crystal with different dislocation densities to check their dependence with dissolution rate at far from equilibrium conditions where mechanisms III and/or II dominate. Simulations with $0, 2, 4, 10, 20, 50, 100$ and 200 dislocations randomly distributed

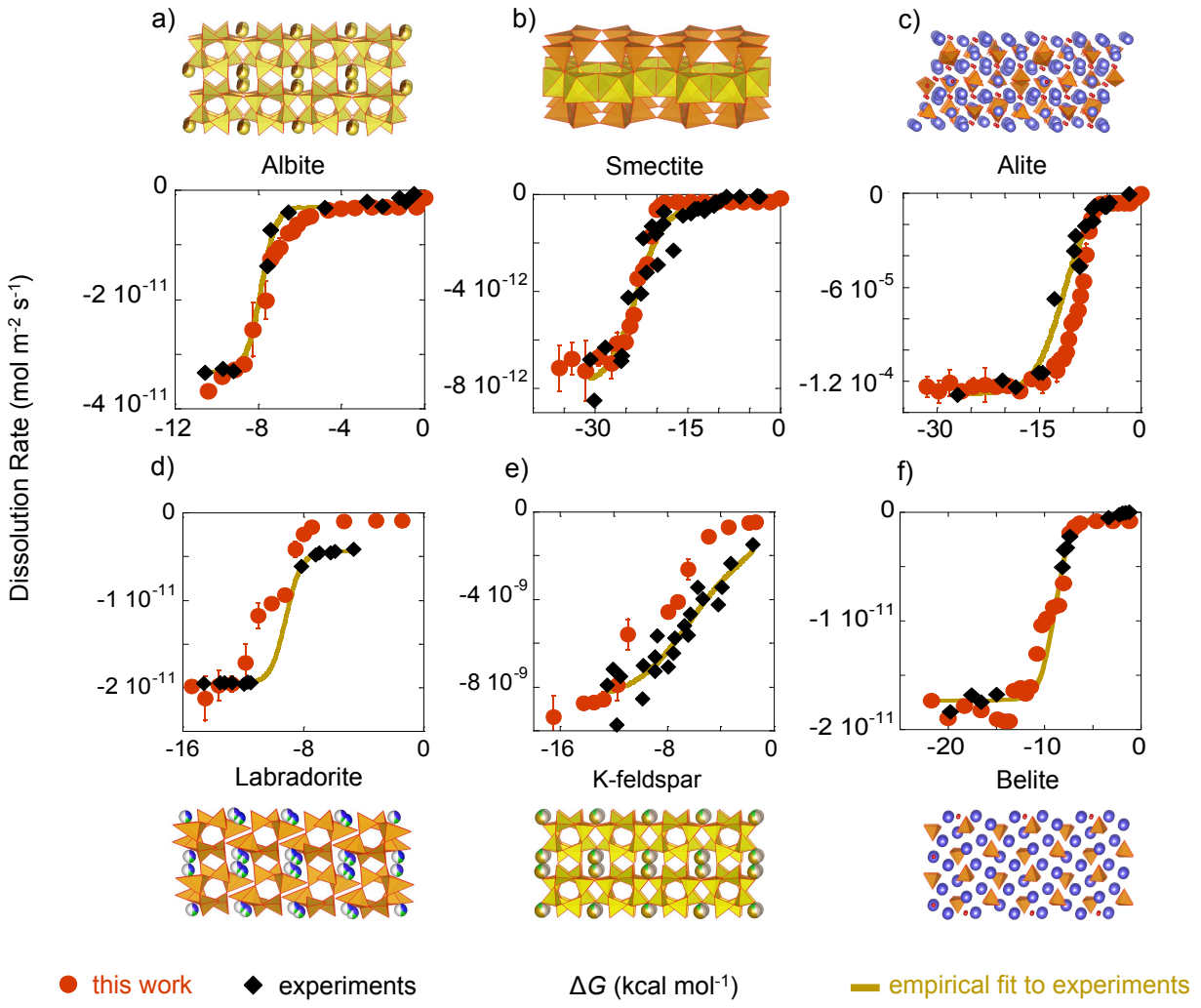

Figure 2.5: **Comparison of the experimental data with the proposed dissolution theory**. a) Albite at pH 8.8 and 357 K [9, 10]. b) Smectite at pH 3 and 357 K [10, 11]. c) Alite at 300 K [12]. d) Labradorite at pH 3 and 300 K [10, 13]. e) K-feldspar at pH 9 and 423 K [14] f) Belite at 300 K [12]. Structural visualization is done using VESTA program [15]. Belite case consists of only one simulation per point.

Mineral	T (K)	$E_{da}(k_BT)$	$E_{pa}(k_BT)$	$E_{a\ m.II/III}$ (kJ mol^{-1})	$E_{a\ m.I}$ (kJ mol^{-1})	$E_{a\ exp.}$ (kJ mol^{-1})	Simulation ΔG_{crit} (kcal mol^{-1})	Analytical ΔG_{crit} (kcal mol^{-1})
Albite	357	11.14	10.00	132	99	69.8 [1] 71 ± 7 [121] 88.6 [84] 69 ± 5 [122]	-8	-7.3 ± 1.9
Smectite	357	11.73	4.00	139	104	52 ± 4 [123]	-23	-21.4 ± 1.9
Alite	300	7.47	4.95	75	56	49 [21]	-11	-8.6 ± 1.6
Labradorite	300	11.40	8.8	114	85	45.2 [1]	-9	-8.8 ± 1.6
Feldspar	423	9.95	10.3	139	104	38.0 [1]	-6	-5 ± 2
Belite	300	11.43	9.0	114	86	-	-9	-8.5 ± 1.6

Table 2.4: **Model parameters for minerals**. Fitting values for figure 2.5 of the corresponding activation energy in each mechanism and comparison with bibliographic ones. ΔG_{crit} value is obtained by equation 2.18 and analytically by equation 2.12.

have been done for $E_{da} = 4.0,\ 7.0,\ 9.0,\ 12.0\ k_BT$ units. In figure 2.6a, the dissolution rates of all the systems are compared, taking as reference the system with two dislocations.

At far from equilibrium conditions, in minerals with low energy barrier ($E_{da} = 4.0, 7.0\ k_BT$ units) the dissolution rate exhibits a small linear dependence with the number of dislocations. In this conditions, corresponding to the mechanism III region, perfect planes are opened spontaneously, so the dislocations hardly affect dissolution. On the opposite side, for minerals with high dissolution energy barrier ($E_{da} = 9.0, 12.0\ k_BT$ units) the rate is more sensitive to dislocations since they represent the only dissolution source. The increase is not lineal, approaching a limit value at high dislocation density due to the coalescence of dissolution fronts.

Our simulations shows very small increase of dissolution rate for minerals with low dissolution energy barrier. Nevertheless, in minerals with high dissolution energy barrier, like the quartz, the variation would be higher than observed experimentally. The explanation of such discrepancy lies in its specific structure, as we will see in section 2.4.8.

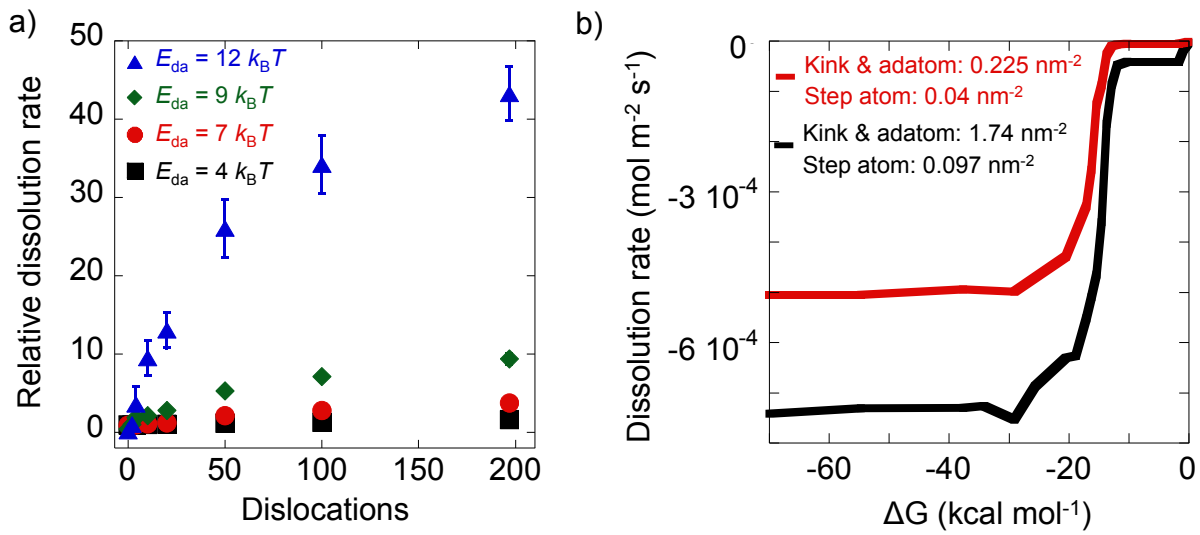

Figure 2.6: **Influence of the dislocation density and surface topography in the dissolution rate**. a) Relative dissolution rate versus the number of dislocations. 2 dislocation case has been chosen as reference point. This value equates to a dislocation density of $\sim 5.5 \cdot 10^{10}$ cm^{-2}. Each point is the mean of 8 values. Error bars are smaller than the point except of the $E_{da} = 12.0\ k_BT$ case. b) Dissolution rate with ΔG for two different systems. In black, the system considered along the chapter and in red a more regular one.

2.4.7 Dissolution rate dependence with surface roughness

Surface initial topography of a mineral may have an important effect on the dissolution rate. Figure 2.6b shows the difference on the dissolution rate for a Kossel crystal with different initial topography. Taking into consideration that initial irregularities are important in mechanism I, and initial step atoms and vacancies are important in mechanisms II/III, both quantities are recorded per nm^2. The system considered in this work presents a density of 1.7436 nm^{-2} of atoms forming terraces or adatoms and 0.0969 nm^{-2} step atoms. A more regular system presents a density of 0.225 nm^{-2} and 0.0411 nm^{-2} respectively. Both systems have $E_{da} = 7.0$ and $E_{pa} = 1.0\ k_BT$. A difference in dissolution rate is appreciated in the initial stages for the whole ΔG range, although is smaller than one order of magnitude. If enough time is waited to reach an steady state, the dissolution rate for both cases at far from equilibrium conditions would be identical.

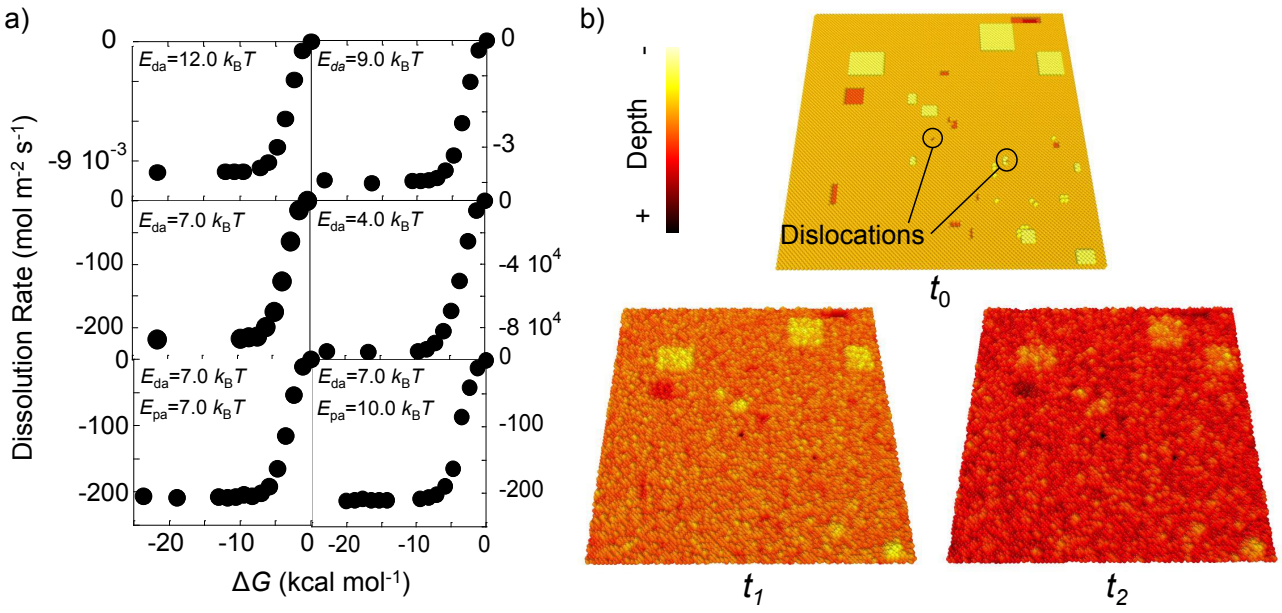

Figure 2.7: **Dissolution rate versus ΔG for 4-coordinated minerals**. a) Study for different precipitation and dissolution energies. b) Typical dissolution pathway of any E_{da} or E_{pa} in three different times. Error bars are smaller than the points.

2.4.8 Four coordinated systems

Coordination number, as can be shown from the mechanisms described above, plays an important role in the dissolution. This section looks for checking the extension of the proposed model to a four coordinated mineral. For that, a diamond like structure system was used to simulate same cases as the Kossel crystal study. The results in the figure 2.7 show a TST behaviour independently of the value of E_{da} or E_{pa}. Only one mechanism governs the dissolution characterized by a random detachment of atoms in the surface without dislocation opening for any E_{da} or E_{pa} value. The further from the equilibrium, the more dissolution until a plateau is reached. In this sense, the study done by Kurganskaya and Luttge for the quartz [16] meets this dissolution mechanism at far from equilibrium conditions when only the first neighbours are considered.

Besides, from figure 2.4b and table 2.3 $E_a \approx 2 \cdot E_{da}$ either at far from equilibrium conditions or close to it. This agrees with the fact that kink atoms, with coordination two, are the only source of dissolution. Dislocations do not enhance the dissolution rate.

These results highlight the importance of mineral structure in dissolution mechanisms. Although we have determined in table 2.4 that a similar E_D and E_P value is needed to recover a TST shape in figure 2.5, it is more likely that such shape relies on a topographical feature.

2.5 Conclusions and outlook

In this chapter a new atomistic mineral dissolution model is presented. Based on the kinetic model, the main novelty of the model consists of taking into account the microscopic reversibility of chemical reactions by adding a new precipitation term to the kinetic model. As a result, it is possible for the first time to reproduce the experimentally observed sigmoidal dependence of the dissolution rate over the whole ΔG range by atomistic simulations. Indeed, as a proof of concept, the two main parameters of the model (the dissolution and precipitation energy barriers) have been calibrated to correctly fit the dissolution rates of several representative minerals. Besides, the model successfully captures the proposed dissolution mechanisms and their activation. The three observed dissolution mechanisms naturally emerge from the simulations depending on dissolution and precipitation energy barriers E_D and E_P, and ΔG: initial irregularities dissolution (mechanism I) at close to equilibrium conditions, pit opening and step retreat (mechanism II) when ΔG_{crit} is reached, and spontaneous vacancy opening (mechanism III) at $\Delta G_{m.III}$ if the E_D and dislocation density are low enough. The model also confirms the generally accepted idea that the onset for the dissolution rate increase is originated by the opening of pits, which constantly supplies terraces for step retreat. Interestingly, according to the simulations, when the dissolution and precipitation energies are sufficiently low and high respectively, there can exist close-to-equilibrium dissolution modes where spontaneous vacancies creation and pit opening can occur before adatom and terrace removal. These dissolution modes have not been previously reported, and should deserve due experimental attention.

The fundamental role played by the specific atomic structure of each mineral has also been highlighted. Thus future works will focus on building realistic mineral models beyond the current implementation based on the simple Kossel crystal.

In summary, the present model sheds new light on the subtle dissolution mechanisms and can open the door to the development of a comprehensive theoretical framework for dissolution and other surface-related phenomena like etching [124].

Chapter 3: KIMERA. A KMC Code for Mineral Dissolution

3.1 Introduction

In the previous chapters we have highlighted the importance of the computational tools to study nanoscale properties. Atomic scale computational methods like DFT, molecular dynamics, molecular mechanics, Monte Carlo (MC) and Kinetic Monte Carlo (KMC), which have been used by an increasing number of authors [16, 42, 61, 80, 106, 109, 125–127], have gained a special interest to complement and verify experimental results. Moreover, KMC method has stood out due to its capacity to reach times comparable to experiments. The effect on dissolution of dislocations [10, 115], grain sizes [61] or surface roughness [109], the inherent topographies associated to the dissolution mechanisms [10, 16, 106, 115], the experimentally observed pulsating frequency at the nanoscale [116], or more recently the dissolution rate dependence with ΔG (see chapter 2) are some of the milestones achieved by KMC simulations.

Unfortunately, while many DFT, molecular dynamics and molecular mechanics programs are available both commercially and with free license [128–131], this is not the case with KMC. KMC simulations present the great advantage of being applicable in a multitude of fields, but also the disadvantage of being too specific to be programmed in a flexible and general package. SPPARKS [132] and MONTECOFFE [103] are two KMC tools that were created to provide researchers a tool with which conduct studies in the fields of materials science. Grain growth in annealed system [133], mesoscale evolution in electron beam welding [134], adsorption of methane in zeolites [103] or oxidation of CO over Pt nanoparticles [103] are some examples of the studies performed with these codes. In this sense, in the field of mineral dissolution there is not a general tool capable of studying the dissolution of any mineral. With that aim, we have developed KIMERA.

KIMERA, whose name is an acronym for *Kinetic Monte Carlo for Mineral Dissolution*, seeks for being a helpful and efficient code which allows to any user with a basic knowledge on the field and KMC to define and simulate the dissolution of a multitude of systems and minerals.

3.2 The KIMERA code

KIMERA aims to be broadly used either in big computer clusters or in personal computers. Therefore, we payed special attention to the implementation of user-friendly commands, a good performance and portability. It is written in the standard C++11 language, which ensures its portability. The program recognizes as input data a wide list of commands explained deeply in the code repository `https://mgp9999@bitbucket.org/mgp9999/kimera-publico.git`. Thanks to these commands, the user can define the simulated system and obtain output files for visualization and analysis as well as restarting files. The program is based on the *N-fold-way* algorithm, which ensures a good efficiency (see section 1.4.3) [90]. Moreover, to overcome the typical problem of KMC simulations of waste of computer power in fast and repeating events [105], we have implemented a Poisson approximation to handle opposite effects of dissolution and precipitation which shows no reduction of performance or biased results (see section 2.3.1 and equation 2.9). If faster simulations were needed, KIMERA has been parallelized using openMP library [135], which is an easy way to divide the workload of some loops of the program between the number of cores available.

3.2.1 Organization

KIMERA is written in the object oriented language C++11. The main feature of these languages is the division of the code into modules, named classes, for an easier organization. This way, subsequent modifications or updates of the code are handled in a controlled fashion, knowing the related pieces of code that may be affected by a change.

KIMERA is divided into 17 classes with a complex relation between them. The class diagram, a scheme of these relations, is shown in figure 3.1. Moreover, a brief description of the classes is

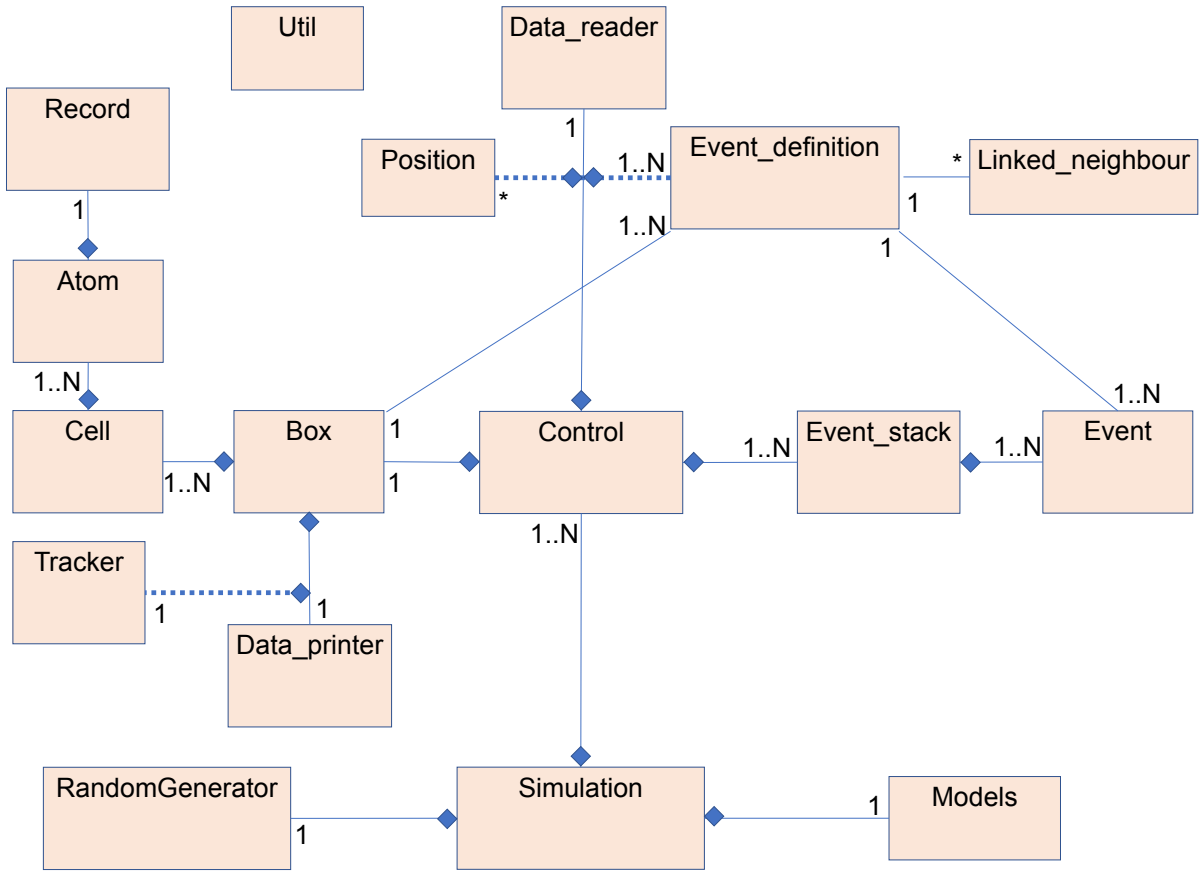

Figure 3.1: **KIMERA class diagram.** Numbers indicate the amount of objects or instances a class can invoke. Blue diamonds indicate that the existence of the object of a class is subordinated to the existence of one object of the other. For example a box is formed by 1 or more cells, but no cells can exist unless a box is created. The asterisk (*) is equivalent to (0..N). Note that the existence of the object of some classes are subordinated to the relation between classes, not to the class itself, like for example the *Tracker* class.

explained below:

- Starting from the highest level of dependency, the *Simulation* class is the most complex class in KIMERA. It unifies all the necessary elements to run a simulation. It is fed first by the *Models* class, which contains information about the definition of the dissolution and precipitation rates (equation 2.9). Secondly it is fed by the *RandomGenerator* class, critical in any KMC code. In our case the mt19937 random generator is used, which ensures high quality random numbers with high entropy [136]. Finally, *Simulation* class is feed by the *Control* class, other of the main classes of the code and explained below.

- *Control* class contains all the necessary parameters, physical constants and user specifications to run a simulation. It is fed by the system box and by the system events which in turn are fed by the reader of the input file via the *Event_definition* class.

- The box contains cells, and the cells contain atoms. Each atom keeps a record of the neighbouring atom list. Besides, since some of the properties of the simulation box are printed during the simulation steps, the *Tracker* class is in charge of saving the data from previous steps. On the other side, the events of the KMC method are stored and sorted in stacks.

- Other classes have support purposes. *Position* and *Linked_neighbour* classes help in the definition of the events. *Util* is a class used by the majority of the classes which contains general utilities as for example geometric relationships like coordinate system changes.

3.2.2 Operation

The workflow of the program can be divided in three parts (see figure 3.2a):

System definition

The user defines the essential parameters of the simulation in an input file. The order of the commands is important since some of them can overwrite previous ones, totally, or partially. In these cases KIMERA always takes into account the last command. Some important steps are:

- **The mineral structure**. The program input can either read it from an external '.xyz' file or can be defined by commands, or a combination of both. The '.xyz' file [137] is easily obtained by tools such as VESTA [15] from downloadable '.cif' files in mineralogical databases [138].

  In principle, KIMERA is thought to construct mineral surfaces replicating a small unit cell. Nevertheless it is also possible to define a complex system within a '.xyz' file and treat it as the whole system box. Coarse grained systems can be also simulated.

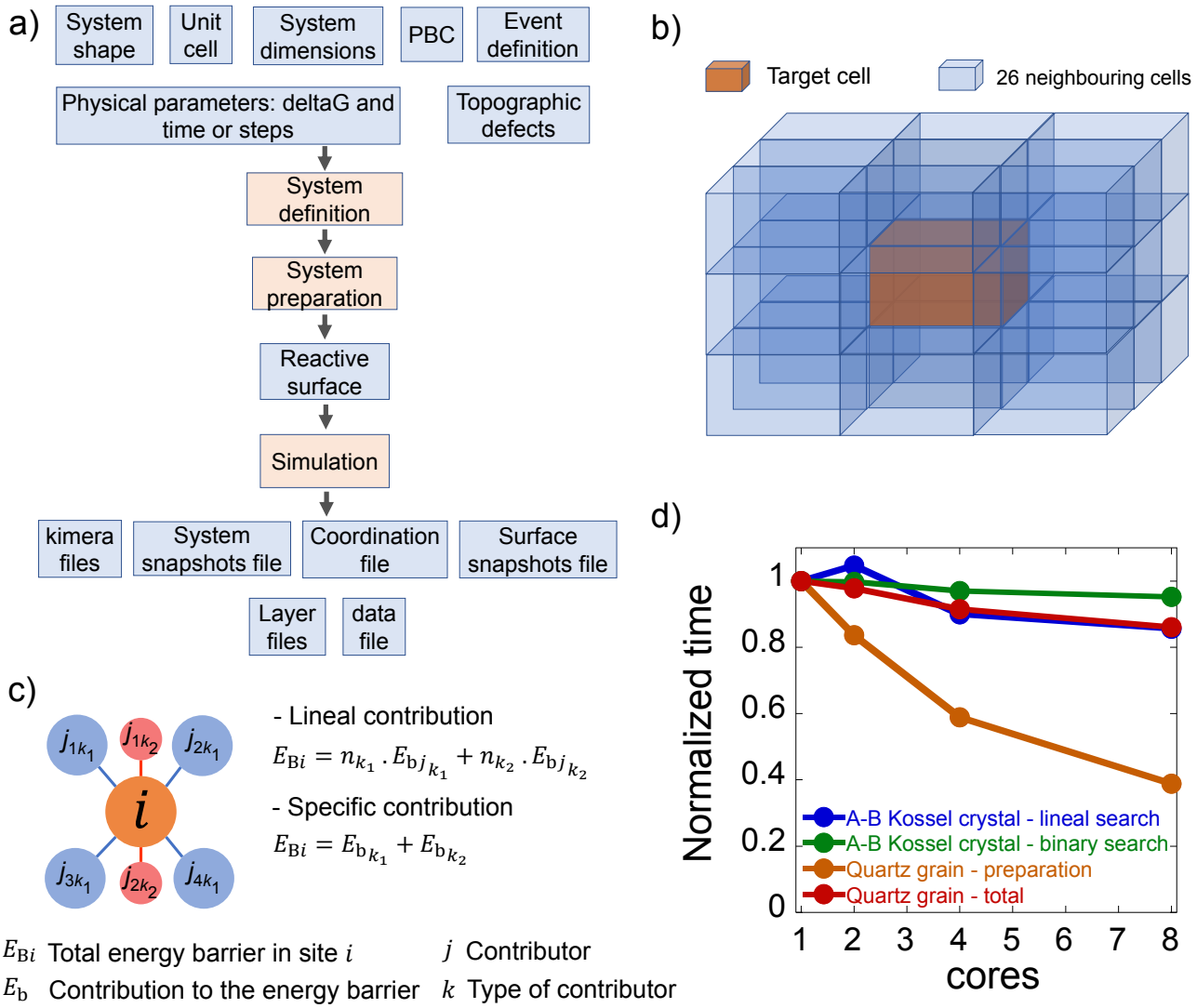

Figure 3.2: **KIMERA features**. a) Workflow b) 26 surroundings cells are checked to look for neighbours, linked and affected atoms, instead of the whole system for performing purposes. c) Example of lineal or specific definition of the energy barrier d) Program performance. Normalized simulation time of the examples with the number of cores. The dissolution of the A-B Kossel crystal case explained in next chapter ('configuration B' in section 4.3.2) is simulated with both lineal search, in blue, and binary search, in green. A simulation time of 18885 s is obtained for both search algorithms in our computer with 1 core. The total simulation time for the quartz grain example in red 2255 s with 1 core, and its preparation phase in orange 902 s

- **The system dimensions**. The program repeats the unit cell in the three spatial directions. Studies of different planes are possible by unit cell transformations with external programs such as VESTA [139]. KIMERA can apply periodic boundary conditions (PBC) in the three spatial directions.

- **System shape**. The program has commands to create different crystalline shapes of the system. For the moment the available geometries are cubic, spherical, parallelepiped, ellipsoidal, tick planes, or a combination of them. In order to build the initial system geometry, external tools such as WOLFRAM ALPHA or GEODEBRA3D can be helpful [140,141].

- **Topographic defects**. Insoluble regions, dislocations, impurities and vacancies can be defined in the system . There are two ways of defining impurities; it is possible to define them in the unit cell indicating their occupancy, or introducing them *ex post* once the system has been defined.

- **Event definition**. The dissolution and precipitation energy barrier for the possible events, as well as its pre-exponential factor, must be indicated (see equations 1.26 and 1.25). KIMERA supports both a lineal and a specific contribution to the energy barriers of each neighbour (see equations 1.37 and 1.43). Supposing n neighbours of an atom, KIMERA can set E_{D} and E_{P} as a linear (equation 3.1) or a specific function (equation 3.2) of each neighbour j [16,142] (see figure 3.2c):

$$E_{\mathrm{D}_k} = E_{\mathrm{d}} \cdot n \quad E_{\mathrm{P}_k} = E_{\mathrm{p}} \cdot n \tag{3.1}$$

$$E_{\mathrm{D}_k} = f(j) \quad E_{\mathrm{P}_k} = g(j) \tag{3.2}$$

Note that the 'flickering bond' model and its lineal simplification (equations 1.43 and 1.37 or 3.1) is a specific case of equation 3.2. Moreover, since the contribution to the energy barrier can be determined for several types of neighbours, k represents each set of contributors with the

same characteristics and E_{D_k} and E_{P_k} its contribution for dissolution and precipitation energy barrier respectively (see figure 3.2c).

$$E_D = \sum_{k=1}^{m} E_{D_k} \quad E_P = \sum_{k=1}^{m} E_{P_k} \tag{3.3}$$

With these two ways of defining the energy barrier, two different approaches can be considered to describe the dissolution events:

1 A **bond by bond** description: each linking bond breaks sequentially and when an atom has no bonds surrounding, it is released from the mineral.

2 A **site by site** description: all bonds reactions are unified in only one event, and each site dissolves with joint probability.

As an additional element, KIMERA supports the conditional event definition. 'Linked' are atoms linked to the neighbour that must exist to take into account the contribution of the latest to the energy barrier. 'Affected' are atoms that automatically dissolve when their parent atom does. These features provide enough versatility to define complex systems, even allowing to define n^{th} order neighbours. Furthermore, it is possible to define the events, based on ghost positions in the unit cell without physical meaning, to make a differentiation between atoms of the same type; for example it is possible to split the atoms of silica into Si1, Si2, etc in the unit cell and then define events for each sub-element.

- **Physical parameters**. Mineral dissolution rate is closely related to the temperature (see section 1.2.3). KIMERA accounts for the temperature directly in the energy barrier values since they are given in $k_B \cdot T$ units . Other key parameter is the Gibbs free energy ΔG (J mol^{-1}) that is related to the concentration of the mineral in the solvent (see section 1.2.1). Later on in section 3.3, we will generalize the ΔG definition for multicomponent minerals within the specific KIMERA framework. As ΔG is also an energy, it must be indicated also in $k_B \cdot T$ units. Other important parameters in mineral dissolution are the pH and other catalytic and inhibitory effects

(see section 1.2.4). These effects are reactions involving lower or higher energy barriers in specific surface sites [6, 31]. Therefore, the way to account for them is defining special sites with lower or higher E_D and E_P. These energy barrier values can be computed with *ab initio* methods or obtained from the bibliography.

There are two options for the simulation to finish. The simplest option is to indicate the number of simulation steps, that is, the number of events to accomplish. The other option is to specify the target time (s) until the simulation is going to run. Predicting the time scale beforehand in a complex system can be difficult. The user can request the program to do an estimation of it by considering the initial possible events. Given s initial sorted groups of rates corresponding to atom removals with different coordination $r'_1 < r'_2 < \cdots < r'_s$, the program approximates the total time for the system to dissolve as if all atoms N_a had the same rate value; the previous to the middle one.

$$t_{approx} = \frac{N_a}{r'_{\frac{s}{2}-1}} \tag{3.4}$$

This approximation arises from considering as limiting step the removal of the atom which leads to a kink atom, always with half of the mineral coordination (see section 2.2.1).

- **Optional parameters** related with the output files. As we will see, output files contain information of the system time evolution like snapshots for visualization or the quantity of dissolved atoms.

System preparation

Once KIMERA has read the input commands, taking into account the event definition and the PBC, it elaborates for each atom a list with all the neighbours, linked and affected atoms. The program searches and recognizes them in all the 26 surrounding cells (counting all the diagonal ones) and in its own one (see figure 3.2b) . This consideration is set for performing purposes, in contrast to checking the whole system.

The program can use the output file from previous simulations as starting point to improve its performance. If this file has been used, some previous commands have to be the same and some can change. In general, commands that affect the neighbourhood such as the periodicity or the event definition structure need to remain identical. In the repository of the code, compatible commands with this feature are highlighted. Most common uses are changes in the ΔG, or changes in the energy barriers.

From the neighbour data, the program elaborates a list with the reactive initial surface. Nevertheless, the surface can be modified *ad-hoc* by the user via commands since undesired surface sites can arise in systems with internal vacancies and impurities.

Simulation

As seen before in section 1.4.3 a key step of the KMC algorithm is to find a random event from the list of possible events looking at its rate [143] (see figure 1.10). This step is the most time consuming. There are two possible methods, the binary or the lineal search. By default the binary search method [102] is done, but the user can ask for the lineal search method. Despite the computational complexity of the latest is higher, it can be parallelized. Later, it is discussed the performance of both search methods in section 3.2.3 and figure 3.2d.

During the simulation the output files generated by KIMERA are:

- Initial KIMERA file of the system in its own format (see code repository) ('.initialkimerabox'). It is designed to save time in calculating neighbourhood, linked and affected atoms. A later simulation which reads this file will not need to do the preparation step.

- Final KIMERA file of the system ('.finalkimerabox'). When the simulation has finished, or has encountered an error, the system is printed in KIMERA format.

- File with system snapshots ('.box') in LAMMPS format [131] for visualization. As this file can contain a lot of data, it may be better to handle the surface file unless for checking reasons.

- File with surface snapshots ('.surface') in LAMMPS format.

- File with the time evolution of the following parameters (‘.data’): the total number of atoms dissolved of each type, its fraction, the surface dispersion, the gyradius (in no PBC systems) as well as all their derivatives.

- File with the mean coordination for each type of atom that have the atoms when dissolving (‘.meandiscoord’). This data is key to calculate correctly ΔG value as explained below.

- Files with the amount of atoms in each layer and each spatial direction (‘.alayer’, ‘.blayer’, ‘.clayer’). For example the ‘.clayer’ file contains the total number of atoms of the the cells in ab plane, layer by layer in c direction.

3.2.3 Parallelization level

The parallelization level of a program is defined as the maximun speedup that the program can have. The speedup of a program from parallelization is limited by how much of the program can be parallelized [144]. For example, if 90% of the program can be parallelized, the theoretical maximum speedup using parallel computing would be 10 times no matter how many processors are used.

We have used the openMP library [135] to parallelize our code. As we have seen, the program presents three well differentiated parts: the system definition, the system preparation, and the simulation itself. The last two are the more time consuming and thus define the total simulation parallelization level. In figure 3.2d we have plotted the performance of the example studied afterwards in a quartz grain (see section 3.5) and the performance of the simulations made for a AB Kossel crystal shown in the next chapter. The preparation phase of the Kossel crystal is very quick and hardly influences the total simulation time. Therefore, it is a good example to get the parallelization level of the simulation phase. A decrease of 5% by increasing the used cores from 1 to 8 is obtained when using binary search. With lineal search the decrease is higher, 16%. Such difference is due to the former search method cannot be parallelized. Although lineal search seems to be more efficient, the roles are expected to be swapped in simulations with bigger systems and a low number of cores. On the other hand, the quartz grain example presents a long system preparation time, which has been

tracked separately. Although the total time presents a reduction of 14% with 8 cores, the system preparation phase shows a good parallelization level with a reduction of 61%. Therefore, best strategy to reduce the simulation time in a study with the same system is to use several cores to print only the initial Kimera file, to later use it in a set of subsequent simulations with only one processor and the default binary search.

3.3 ΔG in a multicomponent mineral

KIMERA is the implementation of the dissolution model described in chapter 2. The model permits to obtain the dissolution rate dependence of a mineral with the local Gibbs free energy ΔG^* which is closely related with the concentration of the species of the mineral in the solvent. Nevertheless, the ΔG^*, which is the input parameter of KIMERA is not directly related with the experimental ΔG since it depends specifically on the Stern layer of each mineral. Therefore, some calculus have to be done thereupon to relate ΔG^* and ΔG. In equation 2.3 we calculated the ΔG for a single component mineral. Hereunder, we extend it to a multicomponent mineral within the formalist of KIMERA, that is, in its fashion to define the events and neighbours.

In a multicomponent mineral, macroscopic ΔG is given by coupling the concentration of each constituent element [81]. Assuming a mineral with l atoms types, m sets of contributors, and n_k neighbours for each contributor set, the Gibbs free energy difference, ΔG, is related with local ΔG^* by considering that the net dissolution rate of the kink atoms of each type ($\overline{n}_k$ for all k) is 0 when $\Delta G = 0$:

$$\Delta G = \sum_{i=1}^{l} \chi_i \cdot \overline{N}_i \cdot \left(\Delta G^* + \left(\sum_{k=1}^{m} E_{\mathrm{D}_k}(\overline{n}_k) - E_{\mathrm{P}_k}(\overline{n}_k) \right) - \ln \frac{f_{\mathrm{D}}}{f_{\mathrm{P}}} \right) \tag{3.5}$$

where χ_i is the fraction of atoms of type i, $\overline{N}_i$ is its average amount of broken bonds to dissolve. ΔG^* is introduced as input parameter in the code. $\overline{n}_k$ is the average number of neighbours of each contributor set to the atom type i in a bond breakage or formation, and $E_{\mathrm{D}}(\overline{n}_k)$ and $E_{\mathrm{P}}(\overline{n}_k)$ are their

respective energy barrier values.

Both χ_i and $\overline{n}_k$ can be obtained from the output data of KIMERA, from the '.data' and '.mean-discoord' files respectively. As these values can change with the considered ΔG^* value, the relation between ΔG^* and ΔG may not be constant. Nevertheless, in practice the deviation is not high and can be considered as constant by calculating them from simulation at far from equilibrium conditions, when $\Delta G^* \to -\infty$ and no precipitation events take place. The user must identify the value of $\overline{N}_i$ by recognising the number of broken bonds during a dissolution process. This differentiation arises, for example, if we want to group several bond breaking events in only one event of different f_f and E_B, such as a coarse grain simulation. In the example of the following section and in the simulations of the following chapters, the ΔG calculus is explicitly highlighted.

3.4 Code validation

As validation of our program, KIMERA is able to reproduce the models described in Kurkanskaya and Luttge's work [16] for quartz dissolution at far from equilibrium conditions. They consider each SiO_2 as a dissolution center with, a joint probability of dissolution within a single step. This can be interpreted as a coarse grain of a SiO_2 unit in each Si site. Moreover, by considering lineal (equation 1.37) or specific (equation 1.43) contribution to the site energy barrier from the number of the first and second neighbouring Si atoms, different models were proposed. Hereunder we have checked some of them.

The first coordination sphere model 'FCS' considers a lineal contribution to the energy barrier with the first neighbours.

$$E_\mathrm{B} = n_1 \cdot E_{\mathrm{B_{Si\text{-}Si1}}} \tag{3.6}$$

By applying it to the {001} plane of quartz, a random peak-and-valley topography is obtained (figure 3.3a corresponding to figure figure 3.4a). This topography was also obtained in our study in the four coordinated mineral in chapter 2 (see figure 2.7).

The second coordination sphere model 'SCS-L1' considers that the second neighbours contribute to the activation energy. Similarly, the lack of them after its replacement by hydroxyl group after a hydrolysis reaction also contributes in the same way.

$$E_{\mathrm{B}} = n_1 \cdot E_{\mathrm{B_{Si\text{-}Si1}}} + (n_2 + n_3) \cdot E_{\mathrm{B_{Si\text{-}Si2}}} \tag{3.7}$$

where n_2 and n_3 are respectively the second neighbouring positions occupied by silicon atoms and by hydrogens. Note that $n_2 + n_3 = 12$ in quartz. The application of 'SCS-L1' model in the $\{001\}$ plane of quartz results in the formation of hexagonal etch pit (see figure 3.3b corresponding to figure 3.4b).

The 'SCS-L2' model is an extension of the previous one since there is a differentiation in the hydroxyl contribution.

$$E_{\mathrm{B}} = n_1 \cdot E_{\mathrm{B_{Si\text{-}Si1}}} + n_2 \cdot E_{\mathrm{B_{Si\text{-}Si2}}} + n_3 \cdot E_{\mathrm{B_{Si\text{-}OH}}} \tag{3.8}$$

In the $\{001\}$ plane with $E_{\mathrm{B_{Si\text{-}OH}}} = 0$, the dissolving surfaces are formed by molecular chains oriented along the crystallographic directions [100], [010], and [110]. Secondly, when the contribution of hydrogens is half of the value of a second silicon ($2 \cdot E_{\mathrm{B_{Si\text{-}OH}}} = E_{\mathrm{B_{Si\text{-}Si}}}$), circular-like pits with rough edges are formed. And finally, when the contribution is the same ($E_{\mathrm{B_{Si\text{-}H}}} = E_{\mathrm{B_{Si\text{-}Si}}}$), the SCS-L1 is recovered and same hexagonal pits are reproduced (figures 3.3c, 3.3d and 3.3e corresponding to figure 3.4c, 3.3d and 3.4e respectively).

Quartz presents a stabilization effect on its surface. The hydroxyl groups attached to silicon atoms form a hydrogen bond network between them, increasing the dissolution energy barrier [16]. It can be represented as all the atoms over the surface are initially insoluble in comparison with the ones close to a dislocation. We named this stabilization effect as 'S2' according to the nomenclature given by Kurganskaya and Luttge [16]. Figure 3.3f corresponding to 3.4f, is obtained in the $\{100\}$ plane with the SCS-L2 model and the S2 method reporting rectangular pits. The FCS model in $\{100\}$ plane with S2 method reports squared pits (figure 3.3g which correspond to figure 3.4g). Finally triangular

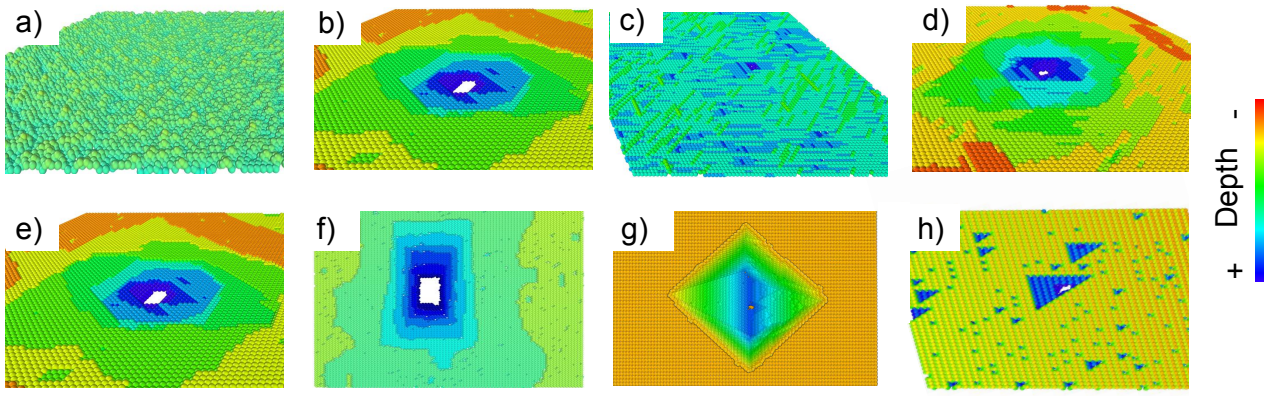

Figure 3.3: **KIMERA validation.** Reproduction of patterns with different models reported in Kurkanskaya and Luttge work [16]. a) Peak-and-valley topography in {001} plane, FSC model (figure 3.4a). b) Hexagonal etch pit in {001} plane, SCS-L1 model (figure 3.4b). c) Molecular chains along [100], [010], and [110] directions in {001} plane, SCS-L2 with no hydrogen contribution model (figure 3.4c). d) Circular-like pits with rough edges in {001} plane, SCS-L2 with some hydrogen contribution model (figure 3.4d). e) Hexagonal etch pit in {001} plane, SCS-L2 with total hydrogen contribution or SCS-L1 model (figure 3.4e). f) Rectangular etch pit in {100} plane, SCS-L2 model and S2 method (figure 3.4f). g) Squared etch pit in {100} plane, FCS model and S2 method (figure 3.4g). h) Triangular etch pit in {101} plane, FCS model (figure 3.4h).

pits are obtained in the {101} plane with FCS model (figure 3.3h which correspond to figure 3.4h).

Overall, KIMERA can reproduce all the tested models, which guarantees a correct implementation of the code.

3.5 Example. Dissolution of an ellipsoidal grain of quartz

In this section, we will specifically indicate the steps needed to make a simulation in KIMERA. We use SCS-L1 model in quartz dissolution, explained in the previous section. As extra ingredient, the system under study consist of an ellipsoidal grain (see figure 3.5a). KIMERA reads the commands from an input file containing the information of the simulation (see appendix A.1):

- System dimensions. A box in which we will define the ellipsoid is created with 50x40x30 unit cells.

- The unit cell parameters. For α-quartz $a = b = 5.01$, $c = 5.47$, $\alpha = \beta = 90^\circ$ and $\gamma = 120^\circ$.

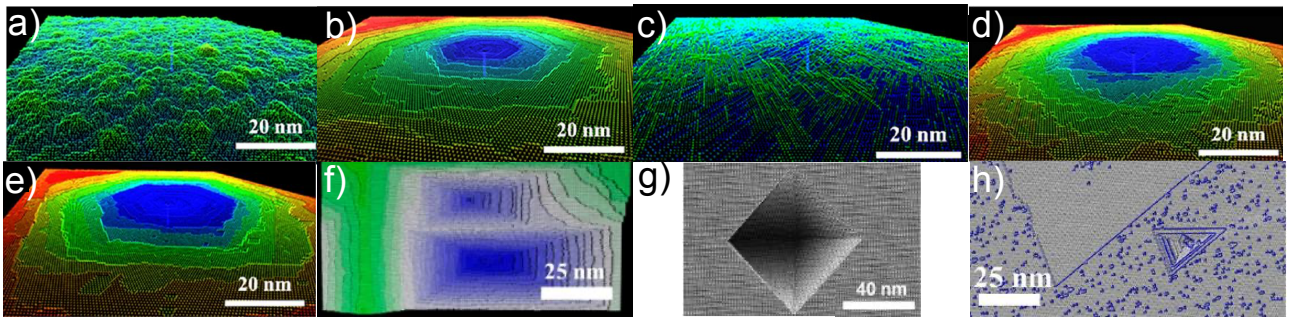

Figure 3.4: **Dissolution patterns in Quartz in Kurkanskaya and Luttge work.** Adapted from [16].

Inside the cell, we call a '.xyz' file containing the positions, which has been converted from a '.cif' file downloaded from a mineral database [138]. Oxygen atoms can be removed for performance purposes since they are not explicitly taken into account for the quartz dissolution reaction in this case. Remember that the dissolution of a SiO_2 is considered in a single step with a joint probability (equation 3.7).

- Physical parameters. The local $\Delta G^* = -100\ k_B T$ units, which ensures far from equilibrium conditions. The target time $t_{\text{target}} = 8.0 \cdot 10^{22}$ s, which is defined *ad-hoc* after the KIMERA time estimation (see equation 3.4).

- Topographic defects. An ellipsoid with radius in the three axes, $r_x = 65$ Å, $r_y = 85$ Å and $r_z = 75$ Å is chosen as the simulation system. A dislocation along the x axis is placed in the middle.

- Event definition. The energy barrier with first neighboring silicon is $E_{\text{D}_{\text{Si-Si1}}} = 28\ k_B T$ units and with second $E_{\text{D}_{\text{Si-Si2}}} = 4\ k_B T$ as considered by Kurkanskaya and Luttge work [16]. Precipitation energies of $E_{\text{P}_{\text{Si-Si1}}} = 10\ k_B T$ and $E_{\text{P}_{\text{Si-Si2}}} = 1\ k_B T$ are considered as a first approximation. All the four first silicon neighbours are at 3.09832 Å. If an atom is surrounded by the four first neighbours, it is considered to be in bulk. 12 second silicon neighbours are at 5.01 Å. Finally, the fundamental frequency values are $f_D = f_P = 1.0 \cdot 10^{12}$ s^{-1} [23].

The relation between ΔG^* and ΔG is calculated by the user using equation 3.5 looking at the

Si-Si-3.09832	Si-Si-5.0100	Si-Si-5.66774	Si-Si-4.42416	ΔG
1.95	1.92	1.92	1.95	$1.95 \cdot (\Delta G^* + 52.47)$

Table 3.1: **Average bond breakage in SCS-L1 model and ΔG^* and ΔG relation**. Average breakage value for each bond for the quartz grain example and the ΔG^* and ΔG relation.

'.meandiscoord' file to get the average breakage of atoms (see table 3.1).

$$\begin{aligned} \Delta G =& 1.95 \cdot (\Delta G^* + \\ & (10.0 \cdot 1.95 + 1.0 \cdot 1.92 + 1.0 \cdot 1.92 + 1.0 \cdot 1.95) + \\ & (28.0 \cdot 1.95 + 4.0 \cdot 1.92 + 4.0 \cdot 1.92 + 4.0 \cdot 1.95)) = \\ & 1.95 \cdot (\Delta G^* + 52.47) \end{aligned} \tag{3.9}$$

Figure 3.5 reports the dissolution rate versus ΔG and the time evolution of the grain. The grain dissolves maintaining an ellipsoidal shape with an irregular surface until its complete dissolution. The dissolution rate changes constantly as the exposed surface decreases. Therefore, we report the values when only half of the forming atoms remain. The surface area is taken as a geometrical approximation in this point (see figure 3.5b), $S_{1/2} = 4 \cdot 10^{-16}$ m^2.

The results show little influence of the dislocation in the dissolution rate . The local coordination at the dislocation does not decrease with respect to other grain regions, so it is not a preferential spot for dissolution. In this case the dissolution rate decreased gradually while getting close to equilibrium following a typical TST curve [6].

This example input file and the '.xyz' file needed are included in appendix A.1 or in the examples folder of the code repository.

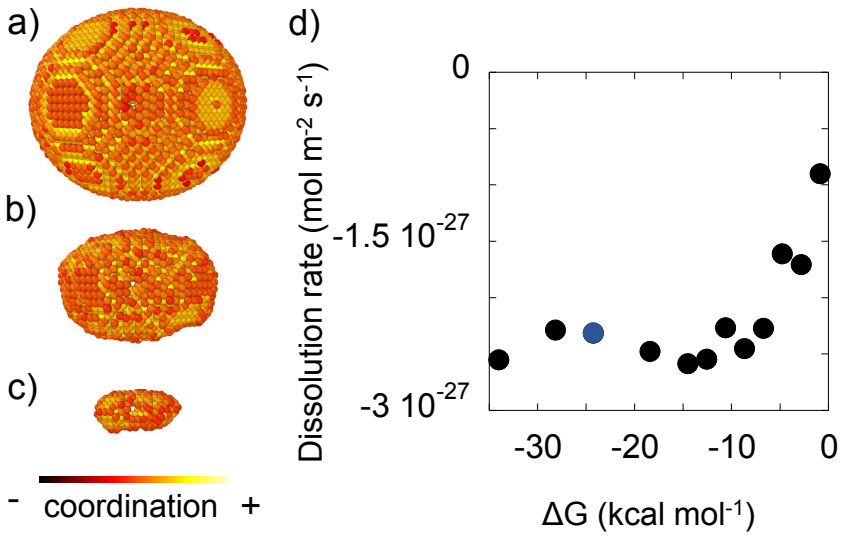

Figure 3.5: **Quartz grain dissolution study with** ΔG. a) Initial grain. b) Grain after half of the forming atoms have dissolved. c) 10 % of the atoms remain. d) Dissolution rate versus ΔG curve. Blue point corresponds to the simulation of the topographies in a-c, though similar topography evolution is obtained in any other point. The visual representation is done using OVITO program.

3.6 Conclusions and outlook

In this chapter we have introduced KIMERA, an open source KMC code to study the mineral dissolution. The code offers portability thanks to its implementation in C++11 language, and a good performance thanks to efficient algorithms and its parallelization feature. Besides, it ensures great versatility thanks to the possibility of performing studies with specific atomistic structures or coarse grains. As validation of our code we have successfully reproduced the topographies obtained for the quartz dissolution in the bibliography [16] with three different models. Moreover, we have specified the necessary steps in one example, though more examples will be shown in following chapters.

Future work will include: 1) an improvement and widening of the event definition, to even consider a differentiation of ΔG^*, f_D and f_P with positions, 2) an extension of the code to consider growth and 3) the development of a tool, webpage or IDE to create and display the system of study.

KIMERA is available as open-source software under the GNU General Public License. Thus, KIMERA can be used free of charge, everyone can contribute to the software, extend it to his own needs and share newly developed plug-ins with other users. The C++ source code of KIMERA

can be downloaded from the bitbucket repository `https://mgp9999@bitbucket.org/mgp9999/kimera-publico.git`

Chapter 4: Dissolution studies in AB Kossel crystals

4.1 Introduction

KIMERA is a flexible and powerful code that gives us a great versatility to study dissolution with the complexity of a real mineral. If the microscopic parameters are known by means of *ab initio* simulations, we can obtain the time evolution of the mineral dissolution and thus other related macroscopic parameters like the activation energy or the surface topographies. Nevertheless, most of the required parameters remain unknown and further *ab initio* investigations are needed. Therefore despite general studies may not report quantitative values, they do provide an idea of the evolution of the system and can reveal unexpected phenomena, as shown in chapter 2.

In this chapter we study the dissolution of a Kossel crystal formed by two atoms, A and B, differently distributed within the system. From a systematic study of several configurations and limit cases, a mapping of the dissolution rate dependence with ΔG and their respective topographical features are revealed. Although the studied configurations and model parameters may not directly correspond to any natural mineral, the results gathered in this chapter will help to foresee the expected dissolution path in many of them and the phenomena arising from the impurities and other point defects in the mineral structure. Besides, this study is expandable to greater scales with coarse grained models, which can be of great interest in industrial applications.

4.2 Model and methods

The systems studied in this chapter are formed by two elements, A and B. By disposing them with different distribution in the Kossel crystal, 5 configurations are built. Note that other configurations are identical by symmetry. Moreover, the additional case of a random distribution of A and B atoms is included. The unit cell of the 6 used configurations are shown in figure 4.1 (configurations A-F).

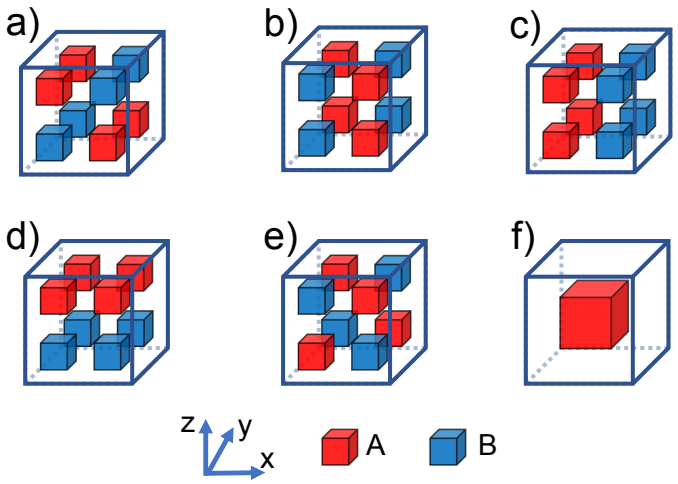

Figure 4.1: **Unit cells of studied cases**. Cubes can represent both an atom or a group of 8 atoms each in one corner. Red cubes represent A atoms and blue ones B atoms. Two colored cube represent that the atom, or group of atoms, can be A or B with the same chance.

As additional element, we have included configurations with same unit cell but considering each cube as a group of 2x2x2 atoms, each atom in each cube vertex. We have labeled all the configurations according to their unit cell if figure 4.1. 2x2x2 systems are labeled as configurations A2-F2.

For each system, the unit cell is replicated in the three spatial directions to form a system of 120x120x30 atoms. If the typical distance between atoms is 2.5 Å [117], the systems have a surface of $\sim$ 30 x 30 nm. Periodic boundary conditions (PBC) in x and y axes are considered to threat them as infinite slabs. Finally, a dislocation of 20 atoms depth and 2x2 atoms width is set in the center of the system, which corresponds to a dislocation density of $\sim 1.1 \cdot 10^{15}$ m^{-2}. The systems are exposed to dissolution in the $\{001\}$ plane.

We select the lineal model in equation 1.37 or 3.1, where E_{da} and E_{pa} are the dissolution and precipitation energy barriers for an adatom. We have chosen a dissolution energy barrier relation of $E_{\text{da}_{\text{A-A}}} = 12\ k_{\text{B}}T$ units for A-A atoms and $E_{\text{da}_{\text{B-B}}} = 4\ k_{\text{B}}T$ units for B-B atoms, which are respectively the higher and lower limit value for most of the minerals [115]. For the A-B interaction the energy barrier is obtained from the Lorentz-Berthelot rule [145], $E_{\text{da}_{\text{A-B}}} = \sqrt{E_{\text{da}_{\text{A-A}}} \cdot E_{\text{da}_{\text{B-B}}}} = 6.92\ k_{\text{B}}T$ units. These values are fixed in all cases. On the other hand, we have taken as precipitation energy barrier 8 different values for each case. In the higher limit case the same values as for the dissolution energy

barrier are taken $E_{\mathrm{pa_{A\text{-}A}}} = E_{\mathrm{da_{A\text{-}A}}} = 12\ k_{\mathrm{B}}T$, $E_{\mathrm{pa_{B\text{-}B}}} = E_{\mathrm{da_{B\text{-}B}}} = 4\ k_{\mathrm{B}}T$ and $E_{\mathrm{pa_{A\text{-}B}}} = E_{\mathrm{da_{A\text{-}B}}} = 6.92\ k_{\mathrm{B}}T$. In the lower limit case, $E_{\mathrm{pa_{A\text{-}A}}} = E_{\mathrm{pa_{B\text{-}B}}} = E_{\mathrm{pa_{A\text{-}B}}} = 1\ k_{\mathrm{B}}T$. The 6 left cases are all the possible combinations between them. Therefore, we have for each configuration, 1 set of dissolution energies and 8 sets of precipitation energies. Even though the choice of values is very unlikely to represent any natural mineral, this systematic study allows to foresee the expected behaviour with other energy barrier values or even in other configurations.

4.2.1 Input for the KIMERA code

In this section we show the necessary steps to create the simulations in the KIMERA program. We describe the steps in a general way, indicating some of the particularities of each case. The input KIMERA files for configuration B and F are included in the appendix A.2.

- The **system dimensions** are indicated; 60x60x15 unit cells. In the random case (configuration F) the dimensions are 120x120x30 units cells. Since its unit cell is formed by only one atom, the total system size is the same.

- The **unit cell parameters**. In the Kossel crystal $\alpha = \beta = \gamma = 90^{\circ}$ and if the interatomic distance is 2.5 Å, which is a typical distance reported for minerals [117], $a = b = c = 5$ Å. Inside the cell, we define the 8 positions of the atoms and later on is replicated. The positions in absolute coordinates are: (0,0,0), (2.5,0,0), (0,0,2.5), (2.5,0,2.5), (0,2.5,0), (2.5,2.5,0), (0,2.5,2.5) and (2.5,2.5,2.5) Å. In configurations A-E, each position is defined as A or B according to its unit cell (see figure 4.1). In configuration F only one position is defined in the center of the unit cell of $a = b = c = 2.5$ Å with an occupancy of 0.5 for each atom type. In configurations A2-B2 all the positions are initially defined as A atoms to later redefine them as B type using additional KIMERA commands.

- We set periodic boundary conditions (**PBC**) along x and y axes.

- **Physical parameters** of the simulation. As we see in equation 3.4, the target time varies in each case due to each different dissolution rate. For example, in configuration B $t_{\mathrm{target}} = 4.0 \cdot 10^{-1}$ s

and in configuration E2 $t_{\text{target}} = 4.0 \cdot 10^2$ s. Therefore, a better strategy is to indicate the total number of steps for the system to completely dissolve, around $4 \cdot 10^5$. The local ΔG^* is initially set to a very low value $\Delta G^* = -100\ k_{\text{B}}T$ units to ensure far from equilibrium conditions and calculate the ΔG and ΔG^* relation (see section 3.3).

- **Event definition**. We specify the dissolution and precipitation energy barriers with the lineal model (see equation 3.1). The fundamental frequency is $2.6 \cdot 10^{12}$ s^{-1} at 300 K. KIMERA also requires the number of neighbours that a bulk atom has to later define the initial reactive surface, for both for A and B atoms. For example in configuration B, a bulk A atom has 2 A and 4 B neighbours. A bulk B atom has 4 A and 2 B neighbours. In configuration B2, the relation is swapped, a bulk A atom has 4 A and 2 B neighbours and a bulk B atom has 2 A and 4 B neighbours. In configuration E2, a bulk A or B atom has 3 A type neighbours and 3 B neighbours.

- **Topographic defects**. We define the last plane $z = 0$ as insoluble and we include one finite dislocation in the center with 20 atoms depth. Since there are atoms inside the dislocation that have less coordination than the corresponding one to a bulk site, the program recognised them as initial reactive surface. We make them insoluble as they are not accessible to the solvent.

- Finally, the **output data** is asked to the program, including the '.data', and '.meandiscoord', needed to relate ΔG and ΔG^*, and '.surface' files for visualization purposes.

4.3 Results

For all the cases, an initial simulation far from equilibrium is done. Then, we can relate ΔG^* and ΔG with equation 3.5 from the data reported in '.data' and '.meandiscoord' files. Table 4.1 shows the relation for each configuration and each precipitation energy barrier set.

By changing the input ΔG^* parameter we obtain the dissolution versus ΔG dependence. The large amount of data to be processed causes some curves to have low resolution. In general we have used

	$\Delta G = a \cdot \Delta G^* + b$																			
	Configuration																			
	A		B		C		D		F		A2		B2		C2		D2		E2		F2	
$E_{\text{paA-A}}$, $E_{\text{paB-B}}$, $E_{\text{paA-B}}$	a	b	a	b	a	b	a	b	a	b	a	b	a	b	a	b	a	b	a	b	a	b
1,1,1	3	58.4	3	56.3	3	71.4	3	57.7	3.135	67.3	3	57.7	2	71.4	1.75	47	3	57.9	3	58.5	2	63.9
1,1,6.92		17		18.3		24		34		25.5		34		24		26.3		47.5		25.0		28.6
1,4,1		52.4		50.8		47.4		46		51.3		45.7		47.4		20.7		44.7		49.4		35.3
1,4,6.92		11		12.8		0		22		9.5		22		0		0		34.38		15.6		0
12,1,1		47.4		43.5		71.4		35.7		57.8		35.7		71.4		47		23.5		42.6		63.9
12,1,6.92		6		5.5		24		12		16.0		12		24		26.3		13.1		9.17		28.6
12,4,1		41.4		38		47.4		23.7		41.8		23.7		47.4		20.7		10.36		33.5		35.3
12,4,6.92		0		0		0		0		0		0		0		0		0		0		0

Table 4.1: ΔG^* **and** ΔG **relation**. The relation, in $k_B T$ units, is calculated for each configuration and precipitation energy barrier set with equation 3.5.

a finer focus in the onset near ΔG_{crit}. As we will see below, the nature of the onset can be due to topography, as we have seen in chapter 2, or to the activation of the dissolution of the constituent elements.

4.3.1 Configuration A

By repeating the unit cell in figure 4.1a in the three spatial dimensions, a mineral consisting of alternated atom chains of A and B type along y and z axes is produced. The compilation of the dissolution rate dependence with ΔG is shown in figure 4.2d. All studied cases present a congruent dissolution with a sigmoid shape except from the light green case with $E_{\text{daA-A}} = E_{\text{paA-A}}$, $E_{\text{daB-B}} = E_{\text{paB-B}}$ and $E_{\text{daA-B}} = E_{\text{paA-B}}$ where the typical TST behaviour is recovered. The onset of the dissolution rate is obtained at different ΔG values. The sorting of this ΔG value can be divided into two groups. The first group on the right of the graph in figure 4.2d consists of the 4 greenish and blued coloured cases. They are characterized by having a high precipitation energy for A atoms $E_{\text{paA-A}} = 12\ k_{\text{B}}T$ units. The onset of the members of this group are sorter in such a way that the higher the E_{pa} values, the closer to equilibrium. The second group, consisting of the blackish and brownish cases and characterized by having a low precipitation energy for A atoms $E_{\text{daA-A}} = E_{\text{paA-A}} = 1\ k_{\text{B}}T$ units, are sorted in the other way around. The higher the E_{pa} values are, the further to equilibrium the onset is. Such sorting is presented in some cases, as we will see in following configurations.

Regarding to the topography, the dissolution is produced longitudinally in the direction of the chains of B atoms, as expected, due to their easier dissolution. The onset in all the cases is produced when the chains of A atoms start to dissolve. The dislocation induces a local and small increase of the dissolution rate. Its effect is also longitudinal and it is determined by its initial size. A particular topography is given at the beginning of the onset in cases where A and B atoms have similar likelihood to dissolve (dark blue and dark green cases in figure 4.2c,d). In this case, the topographic effect of the dislocation gains importance and the smooth layers are sequentially removed by step retreat. This dissolution mode quickly disappears with a small deviation from equilibrium.

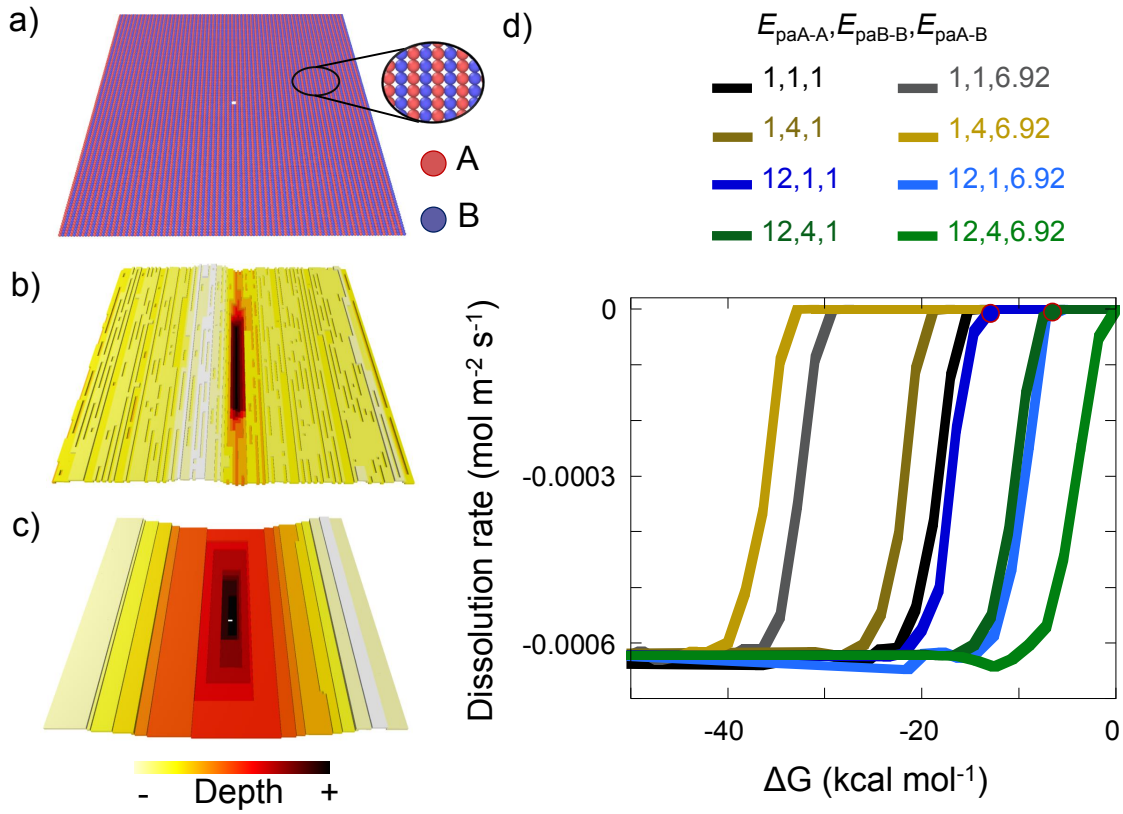

Figure 4.2: **Study in configuration A**. a) Initial surface system. b) Typical dissolution pattern during the dissolution at far from equilibrium conditions. c) Particular topography given in blue and green cases at the beginning of the onset (blue and green points in the graphic) when B and A atoms have similar dissolution likelihood. d) Dissolution rate versus ΔG for both A and B atoms. OVITO program is used for visualization [8].

4.3.2 Configuration B

By repeating the unit cell in figure 4.1b in the three spatial dimensions, a mineral consisting of alternated atom chains of A and B type along x and y axes is produced. Note that this configuration would correspond to the same system as configuration A, but the dissolution takes place in another crystallographic direction. The compilation of the dissolution rate dependence with ΔG is shown in figure 4.3e. Same as before, all studied cases present a congruent dissolution with a sigmoid shape except from the light green case with $E_{\text{daA-A}} = E_{\text{paA-A}}$, $E_{\text{daB-B}} = E_{\text{paB-B}}$ and $E_{\text{daA-B}} = E_{\text{paA-B}}$ where the typical TST behaviour is recovered. In this case, the sorting of the dissolution rate onset is highly influenced by the $E_{\text{daA-B}}$ and $E_{\text{paA-B}}$ relation. This is because a A-B bond breakage is the most frequent in this mineral. For an atom on the surface, 4 out of its 5 bonds are A-B. As a consequence, the sorting of the onset is mixed as shown in the graph in figure 4.3e.

Regarding to the topography, the dissolution is produced similarly to a Kossel crystal with only one element and $E_{\text{da}} = 7\ k_{\text{B}}T$ units (see figure 2.2). The onset is produced by a circular opening of the dislocation, which is the main source of dissolution. Moreover, by decreasing ΔG spontaneous opening (mechanism III) is produced (see figure 4.3b). Particular topographies appear at the beginning of the onset. If $E_{\text{paA-A}} = 12\ k_{\text{B}}T$ units, the dislocation opening has a squared shape rotated 45º around the z axis (see figure 4.3c and rounded red points in figure 4.3e). If $E_{\text{paA-A}} = 1\ k_{\text{B}}T$ units, the dislocation opening has also a squared shape but it is not rotated (see figure 4.3d and rounded grey points in figure 4.3e). These dissolution modes quickly disappear with a small deviation from equilibrium. The origin of these particular topographies resides in the difficulty of dissolution of A and B atoms respectively. In the first case, once A atoms have dissolved, B quickly dissolves. Therefore the dissolution topography is determined by the diagonal disposition of A atoms. In the second case both kind of atoms dissolve with similar rate thus the patterns produced is not rotated.

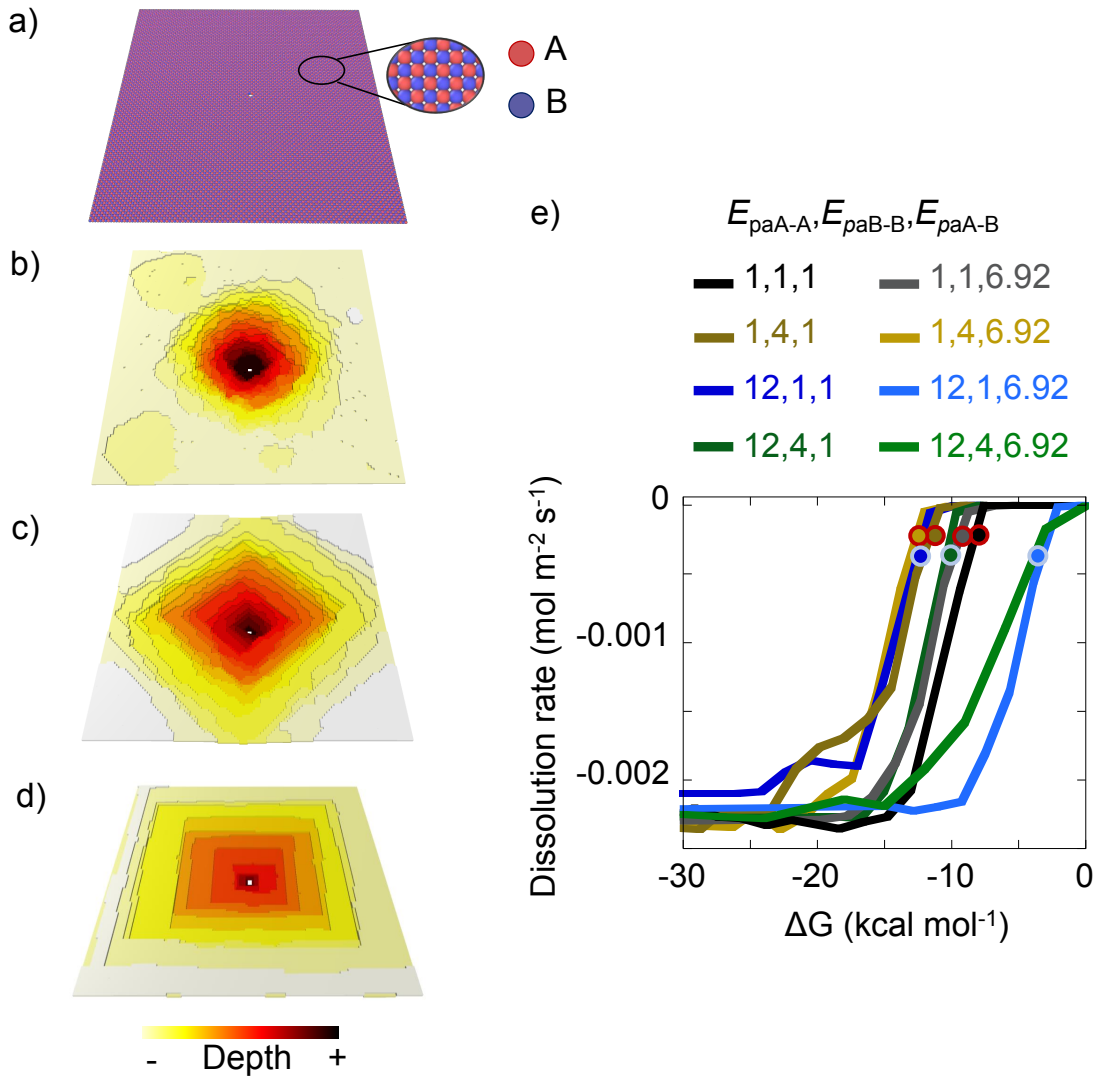

Figure 4.3: **Study in configuration B**. a) Initial surface system. b) Typical dissolution pattern during the dissolution at far from equilibrium conditions. c) Particular topography given in blackish and brownish cases at the beginning of the onset (red rounded points in the graphic) when A atoms has lower dissolution likelihood. d) Particular topography given in blued and dark green cases at the beginning of the onset (grey rounded points in the graphic) when A and B atoms has similar dissolution likelihood. e) Dissolution rate versus ΔG for both A and B atoms.

4.3.3 Configuration C

By repeating the unit cell in figure 4.1c in the three spatial dimensions, a mineral consisting of alternated layers of A and B type along y axis is produced. The compilation of the dissolution rate dependence with ΔG is shown in figure 4.4c,d.

This case has the particularity that the dissolution is incongruent [146] and B atoms dissolves much faster than A atoms. According to the topography shown in figure 4.4b, B layers dissolve quickly leaving alternating A layers exposed to dissolution. Such topography lacks of physical meaning at atomic scales since a reconfiguration of remaining atoms is expected to happen, changing the energy barriers. This reconfiguration is not considered in our model thus only the dissolution rates at the very initial stages of the dissolution can be reported. Note that if higher scales are considered by doing a coarse grained study, the configuration in 4.4b may be possible.

In figure 4.4c,d the dissolution rate for A and B atoms is respectively shown. Depending on the atom type and energy barrier values, the dissolution rate onset is produced at different ΔG positions. The origin of this onset is produced when the A or B layers start to dissolve. The dislocation represents a local and small increase of the dissolution rate of both atom types. Its effect is longitudinal and it is determined by the its initial size (figure 4.4b). At far from equilibrium in the dissolution plateau, A atoms present a dissolution rate around four order of magnitude lower than B atoms. Among all the cases there are three, the grey one, the light brown one and the light green one which are stable and present no dissolution when $\Delta G = 0$ for both atom types. The rest of the cases would dissolve as soon as they are in contact with the solvent so minerals with such characteristics would be difficult to be found in nature.

4.3.4 Configuration D

By repeating the unit cell in figure 4.1d in the three spatial dimensions, a mineral consisting of alternated layers of A and B type along z axis is produced. Note that this configuration would correspond to the same system as configuration C, but the dissolution takes place in another crystallographic

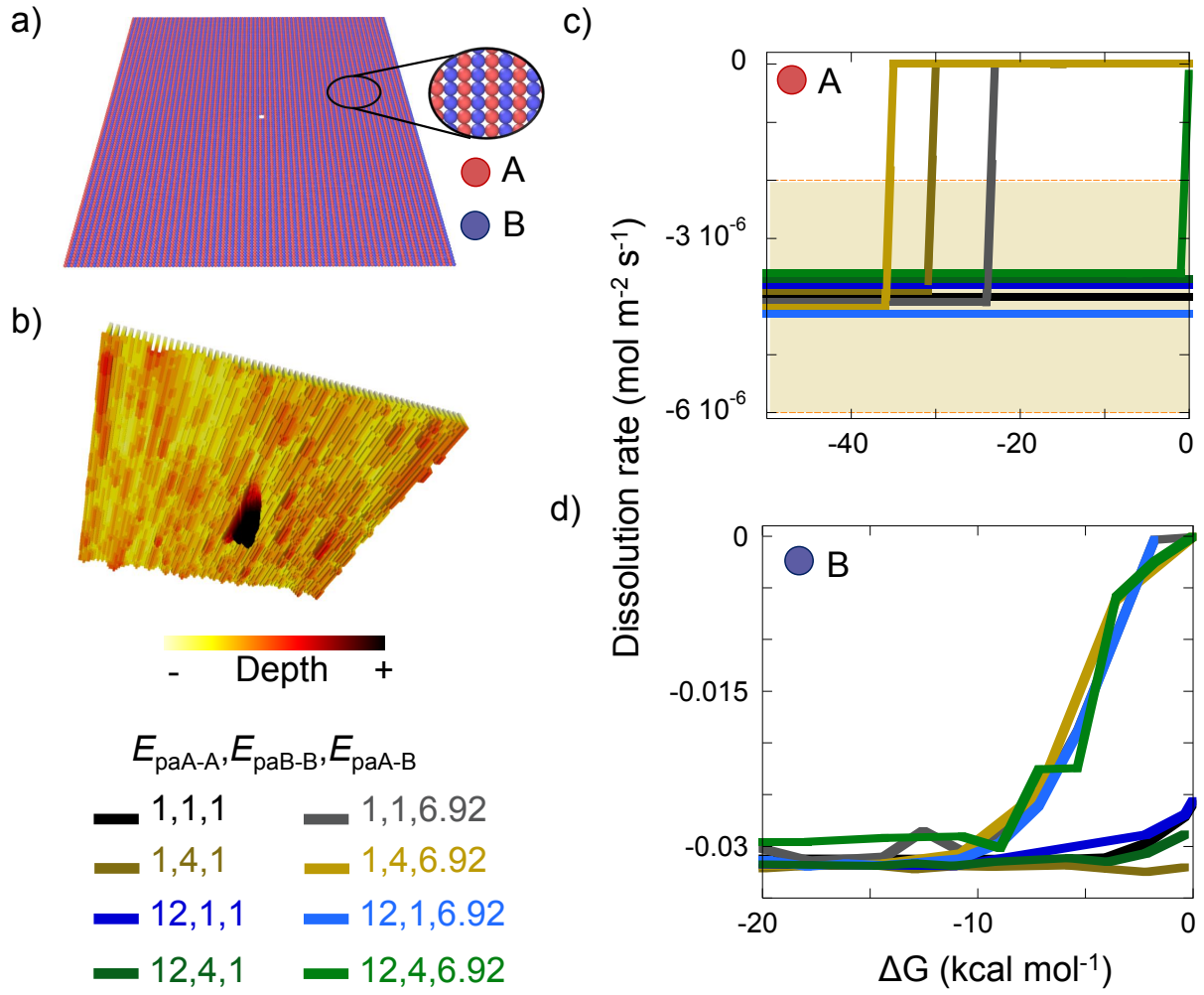

Figure 4.4: **Study in configuration C**. a) Initial surface system. b) Typical dissolution pattern during the dissolution at far from equilibrium conditions. Bottom view of the reactive surface is shown for visualization purposes. c) Dissolution rate versus ΔG for A atoms and d) B atoms. Orange area shows the dispersion of the dissolution plateau values for A atoms.

direction. The compilation of the dissolution rate dependence with ΔG is shown in figure 4.5d. All studied cases present a congruent dissolution with a sigmoid shape except from the light green case with $E_{\text{daA-A}} = E_{\text{paA-A}}$, $E_{\text{daB-B}} = E_{\text{paB-B}}$ and $E_{\text{daA-B}} = E_{\text{paA-B}}$ where the typical TST behaviour is recovered.

Similarly to configuration A (see section 4.3.1), the dissolution rate onset are divided into two groups. A first group, with high precipitation energy for A atoms $E_{\text{paA-A}} = 12\ k_{\text{B}}T$ units, has its onset at low ΔG values. The second group, with low precipitation energy for A atoms $E_{\text{paA-A}} = 1\ k_{\text{B}}T$ units has its onset at higher ΔG values. The cases in both groups are sorted differently depending on the $E_{\text{paB-B}}$ and $E_{\text{paA-B}}$ values.

Regarding to the topography, the dissolution is produced similarly to a Kossel crystal with only one element and $E_{\text{da}} = 12\ k_{\text{B}}T$ units (see figure 2.2). The onset is produced by the layer by layer opening of the dislocation. Once A atoms are removed, B atoms quickly remove. A particular topography is given at the beginning of the onset for dark blue and dark green cases. When A and B atoms have similar likelihood to dissolve, the dislocation opening is not so sharp and the subsequent layers opening happens before the complete dissolution of the layer (see figure 4.5c).

4.3.5 Configuration E

By repeating the unit cell in figure 4.1e in the three spatial dimensions, a mineral consisting of alternated atoms of A and B type along the three axes is produced. This mineral consist only of A-B bonds thus it would be like a mineral of only one atom type with $E_{\text{da}} = 6.92\ k_{\text{B}}T$ units. As this case has been previously studied in chapter 2 (see figure 2.2) with very close values of $E_{\text{da}} = 7$ and $E_{\text{pa}} = 7$, $E_{\text{pa}} = 1\ k_{\text{B}}T$ units, no further study is done here.

4.3.6 Configuration F

The random distribution of A and B atoms in a mineral is studied (see figure 4.1f). The compilation of the dissolution rate dependence for both atom types with ΔG is shown in figure 4.6cd. The reported

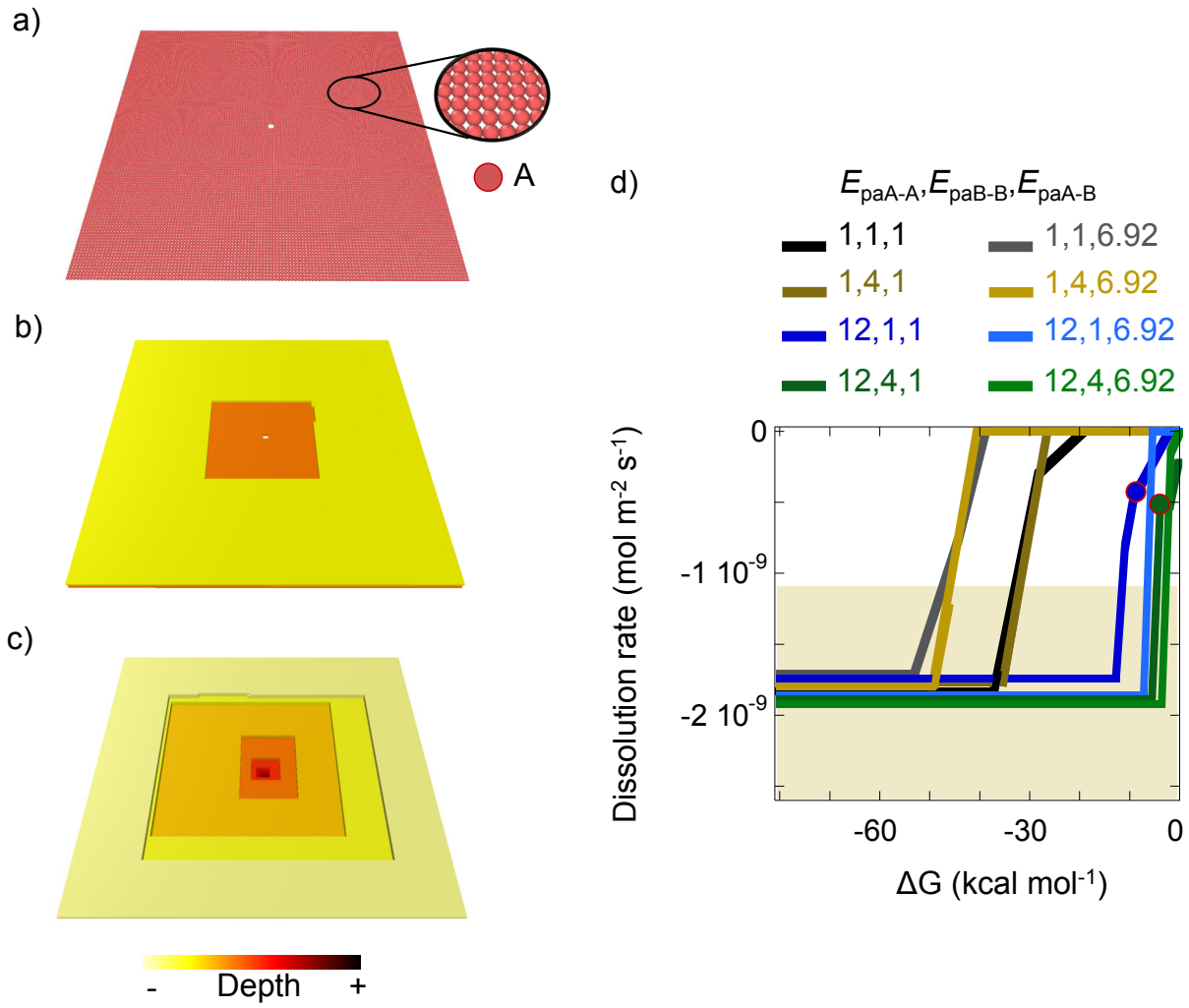

Figure 4.5: **Study in configuration D**. a) Initial surface system. b) Typical dissolution pattern during the dissolution at far from equilibrium conditions. c) Particular topography given in blue and green cases at the beginning of the onset (blue and green points in the graphic) when B and A atoms have similar dissolution likelihood. d) Dissolution rate versus ΔG for both A and B atoms. Orange area shows the dispersion of the dissolution plateau values.

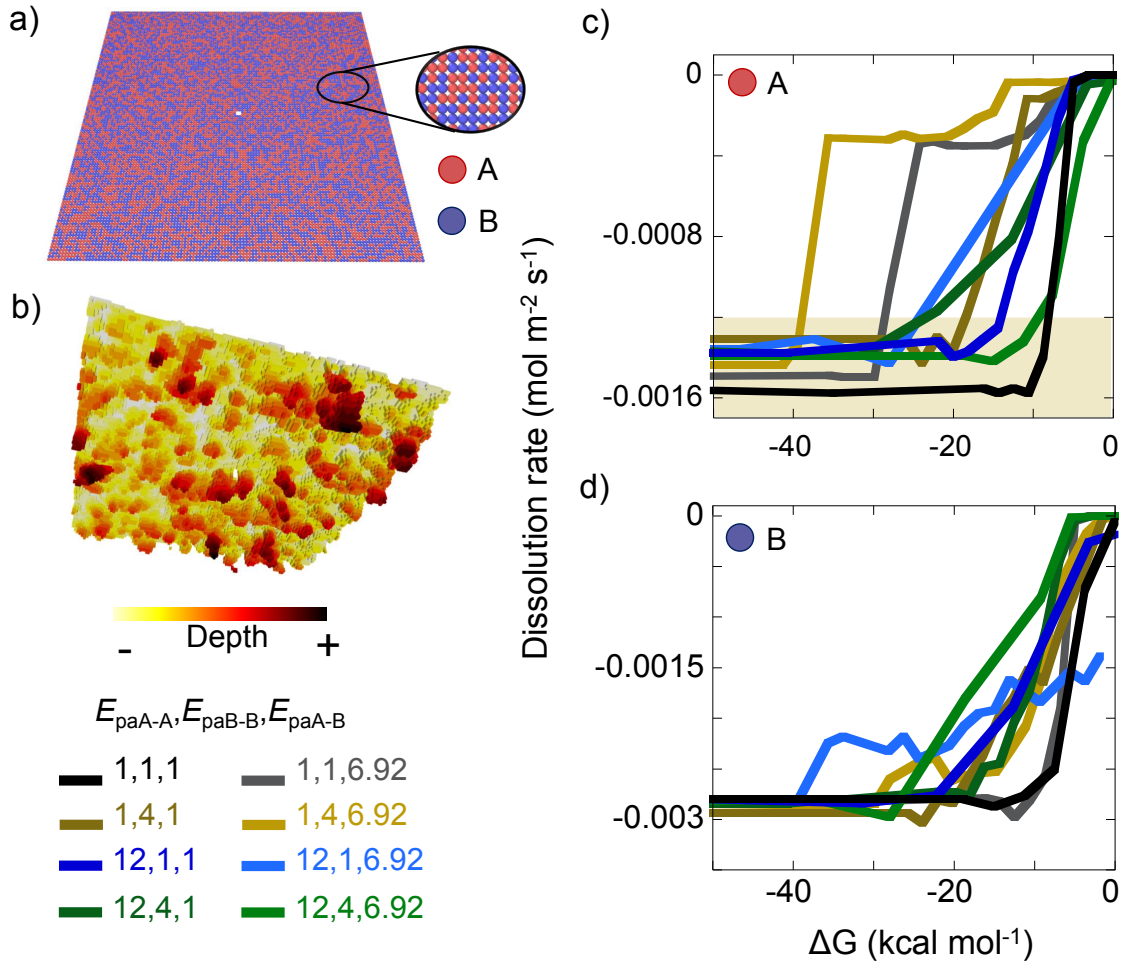

Figure 4.6: **Study in random configuration F**. a) Initial surface system. b) Typical dissolution pattern during the dissolution at far from equilibrium conditions. Bottom view of the reactive surface is shown for visualization purposes. c) Dissolution rate versus ΔG for A atoms and d) B atoms. Orange area shows the dispersion of the dissolution plateau values for A atoms.

topography in figure 4.6b shows a random pattern with deeper dissolution spots where B atoms density is higher. The dislocation does not affect the dissolution. As we cannot assure that this topography is possible without reconfiguration, especially in cases where only B atoms are dissolving leaving random A atom structures, we report the dissolution rate at the very initial stages.

All studied cases present an incongruent dissolution and most of them a sigmoid shape curve. B atoms dissolution rate in the plateau is around 4-5 times higher than for A atoms. The activation of the dissolution of each atom type sets the dissolution onset. A atoms present, for the two brownish and the grey curves, two well differentiated onsets. Such effect arises from this specific configuration

where each atom may have a wide range of possible bonds. First onset is related to a decrease of coordination with B atoms due to an higher reactivity of A-B bonds. Second onset is related to an higher reactivity of A-A bonds. This important two onset phenomena could be expected in the dissolution of glasses and amorphous metal alloys, and to authors knowledge, it has not yet been experimentally observed.

The blued cases present a dissolution of B atoms at $\Delta G = 0$ and would dissolve as soon as they are in contact with the solvent. Minerals with such characteristics would be difficult to be found in nature.

4.3.7 Configuration A2

By repeating the unit cell in figure 4.1a in the three spatial dimensions, a mineral consisting of alternated 2x2 squared atom chains of A and B type along y and z axes is produced. The compilation of the dissolution rate dependence with ΔG is shown in figure 4.7c. All studied cases present a congruent dissolution with a sigmoid shape except from the light green case with $E_{\text{daA-A}} = E_{\text{paA-A}}$, $E_{\text{daB-B}} = E_{\text{paB-B}}$ and $E_{\text{daA-B}} = E_{\text{paA-B}}$ where the typical TST behaviour is recovered. The onset of the dissolution rate is obtained at different ΔG values. Similarly to configuration A and D (see section 4.3.1 and 4.3.4), the dissolution rate onset are divided into two groups. A first group, with high precipitation energy for A atoms $E_{\text{paA-A}} = 12\ k_{\text{B}}T$ units, has its onset at low ΔG values. The second group, with low precipitation energy for A atoms $E_{\text{paA-A}} = 1\ k_{\text{B}}T$ units has its onset at higher ΔG values. The cases in both groups are sorted differently depending on the $E_{\text{paB-B}}$ and $E_{\text{paA-B}}$ values.

Regarding to the topography, the dissolution is produced longitudinally in the direction of the chains of B atoms, as expected, due to their easier dissolution (see figure 4.3.7b). The onset in all the cases is produced when the chains of A atoms start to dissolve. The dislocation represents a local and small increase of the dissolution rate. Its effect is also longitudinal and it is determined by the its initial size.

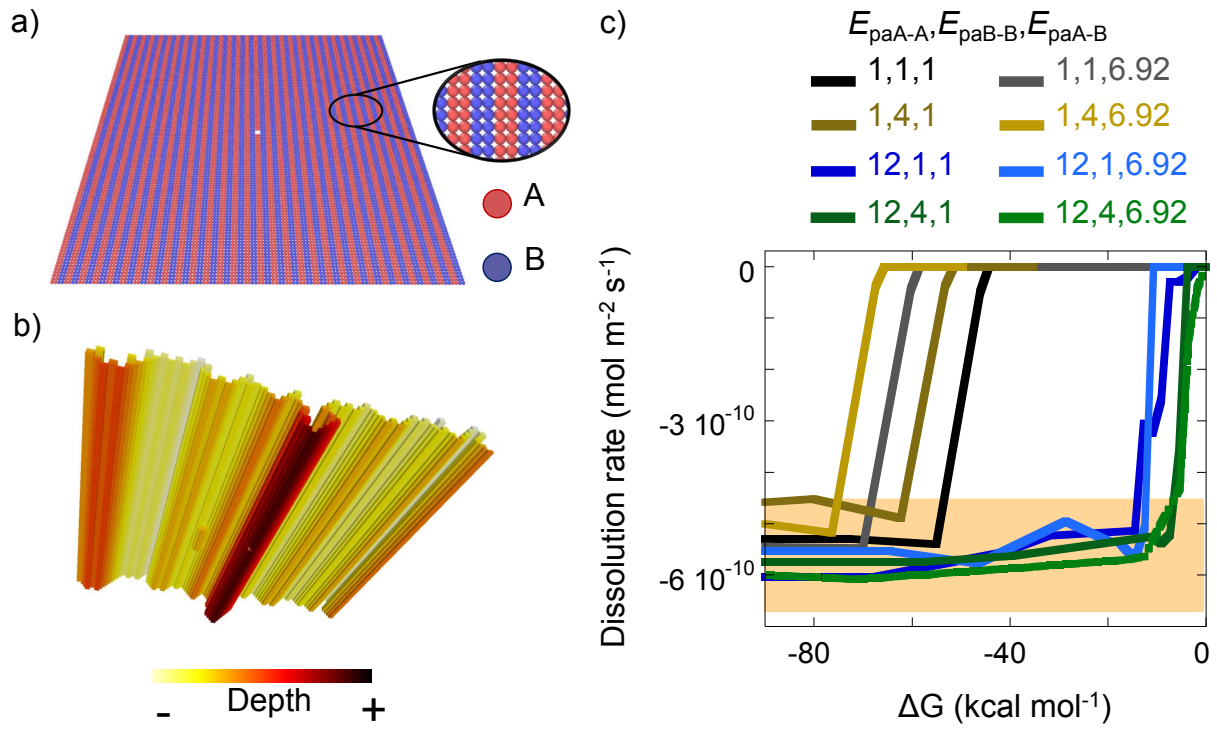

Figure 4.7: **Study in configuration A2**. a) Initial surface system. b) Typical dissolution pattern during the dissolution at far from equilibrium conditions. Bottom view of the reactive surface is shown for visualization purposes. c) Dissolution rate versus ΔG for both A and B atoms. Orange area shows the dispersion of the dissolution plateau values

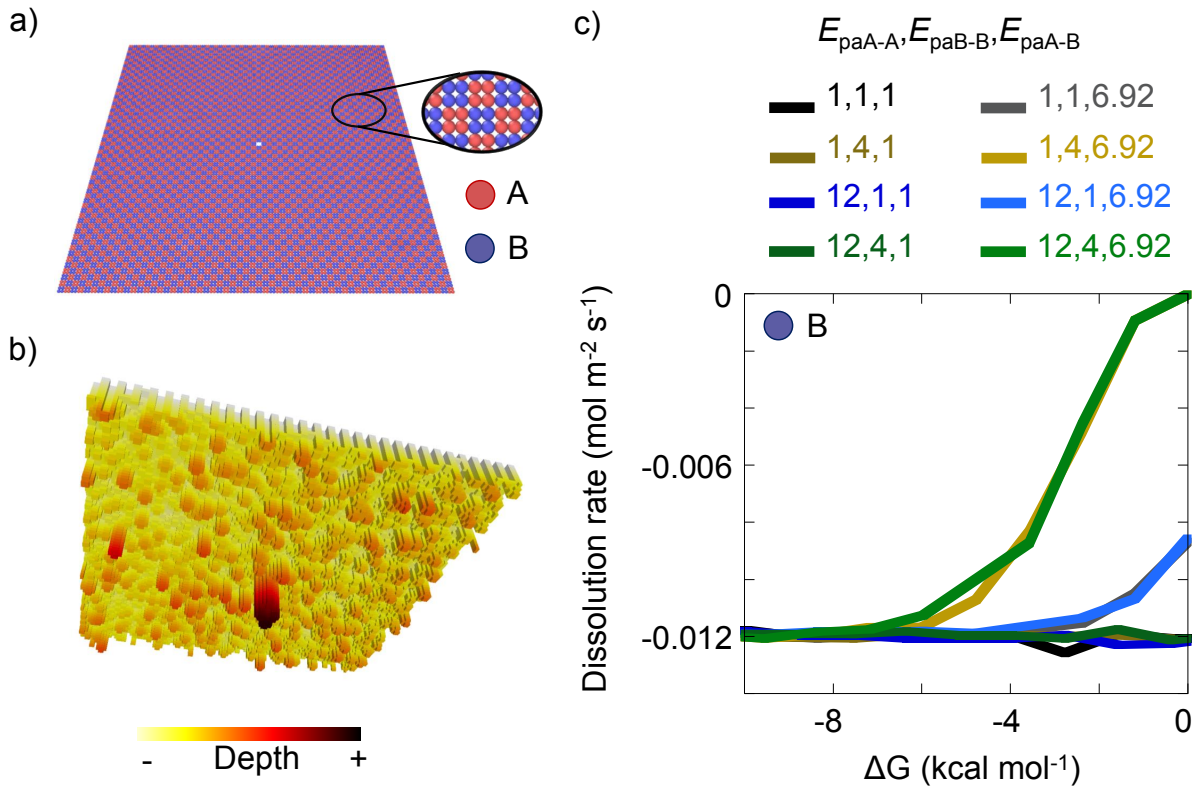

Figure 4.8: **Study in configuration B2** . a) Initial surface system. b) Typical dissolution pattern during the dissolution at far from equilibrium conditions. Bottom view of the reactive surface is shown for visualization purposes. c) Dissolution rate versus ΔG for B atoms.

4.3.8 Configuration B2

By repeating the unit cell in figure 4.1b in the three spatial dimensions, a mineral consisting of alternated 2x2 squared atom chains of A and B type along x and y axes is produced. The topography in figure 4.8b shows that only B atoms dissolve with a local effect of the dislocation. Since this is unlikely to happen without mineral reconfiguration, only the dissolution rate at very initial stages is reported. The compilation of the dissolution rate dependence of B atoms with ΔG is shown in figure 4.8c. All cases except from the light green and the light brown ones show dissolution at $\Delta G = 0$ so minerals with such characteristics would be difficult to be found in nature.

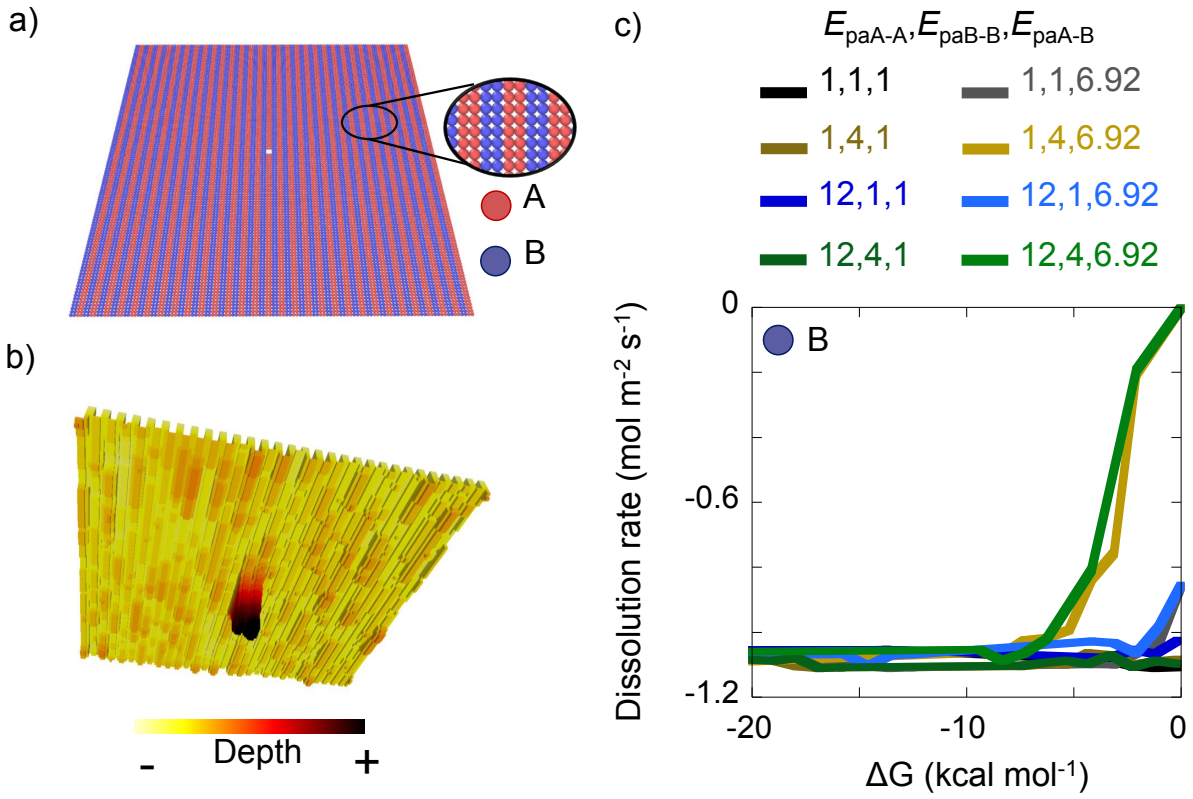

Figure 4.9: **Study in configuration C2** . a) Initial surface system. b) Typical dissolution pattern during the dissolution at far from equilibrium conditions. Bottom view of the reactive surface is shown for visualization purposes. c) Dissolution rate versus ΔG for B atoms.

4.3.9 Configuration C2

By repeating the unit cell in figure 4.1c in the three spatial dimensions, a mineral consisting of alternated layers of 2 atoms length along the y axis is produced. Same as the previous case, the topography in figure 4.9b shows that only B atoms dissolve with a local effect of the dislocation. Since this is unlikely to happen without mineral reconfiguration, only the dissolution rate at very initial stages is reported. The compilation of the dissolution rate dependence of B atoms with ΔG is shown in figure 4.9c. All cases except from the light green and the light brown ones show dissolution at $\Delta G = 0$.

4.3.10 Configuration D2

By repeating the unit cell in figure 4.1d in the three spatial dimensions, a mineral consisting of alternated layers of 2 atoms length along the z axis is produced. The compilation of the dissolution rate dependence with ΔG is shown in figure 4.10d. Topographies and dissolution curves follow a very similar behaviour to configuration D studied before (see section 4.3.4). In the following three small differences are pointed. First, the dissolution rate is lower, approaching closely to the one obtained in the one element Kossel crystal case with $E_{\mathrm{da}} = 12\ k_{\mathrm{B}}T$ units studied in chapter 2. This is because to the limiting dissolution step has identical neighbourhood, and thus also the same E_{D}, yet the number of accessible atoms once this dissolves are greater. Secondly and related also with the small change in neighbourhood, the onset obtained in this configuration is more separated in ΔG. Finally, the particular configuration shown in figure 4.10c is given in all the four cases when $E_{\mathrm{paA\text{-}A}} = 12\ k_{\mathrm{B}}T$ units at the begining of the onset (red rounded points in figure 4.10d).

4.3.11 Configuration E2

By repeating the unit cell in figure 4.1e in the three spatial dimensions, a mineral consisting of alternated groups of 2x2x2 atoms of A and B type along the three axes is produced. The compilation of the dissolution rate dependence with ΔG is shown in figure 4.11d. All studied cases present a congruent dissolution with a sigmoid shape except from the light green case with $E_{\mathrm{daA\text{-}A}} = E_{\mathrm{paA\text{-}A}}$, $E_{\mathrm{daB\text{-}B}} = E_{\mathrm{paB\text{-}B}}$ and $E_{\mathrm{daA\text{-}B}} = E_{\mathrm{paA\text{-}B}}$ where the typical TST behaviour is recovered. As some previous cases (see sections 4.3.1, 4.3.4 and 4.3.10) the dissolution rate onset are divided into two groups. A first group, with high precipitation energy for A atoms $E_{\mathrm{paA\text{-}A}} = 12\ k_{\mathrm{B}}T$ units, has its onset at low ΔG values. The second group, with low precipitation energy for A atoms $E_{\mathrm{paA\text{-}A}} = 1\ k_{\mathrm{B}}T$ units has its onset at higher ΔG values. The cases in both groups are sorted differently depending on the $E_{\mathrm{paB\text{-}B}}$ and $E_{\mathrm{paA\text{-}B}}$ values.

Regarding to the topography in general, the dissolution is produced randomly over the surface with no effect of the dislocation. A atoms groups are the limiting factor and set the dissolution rate.

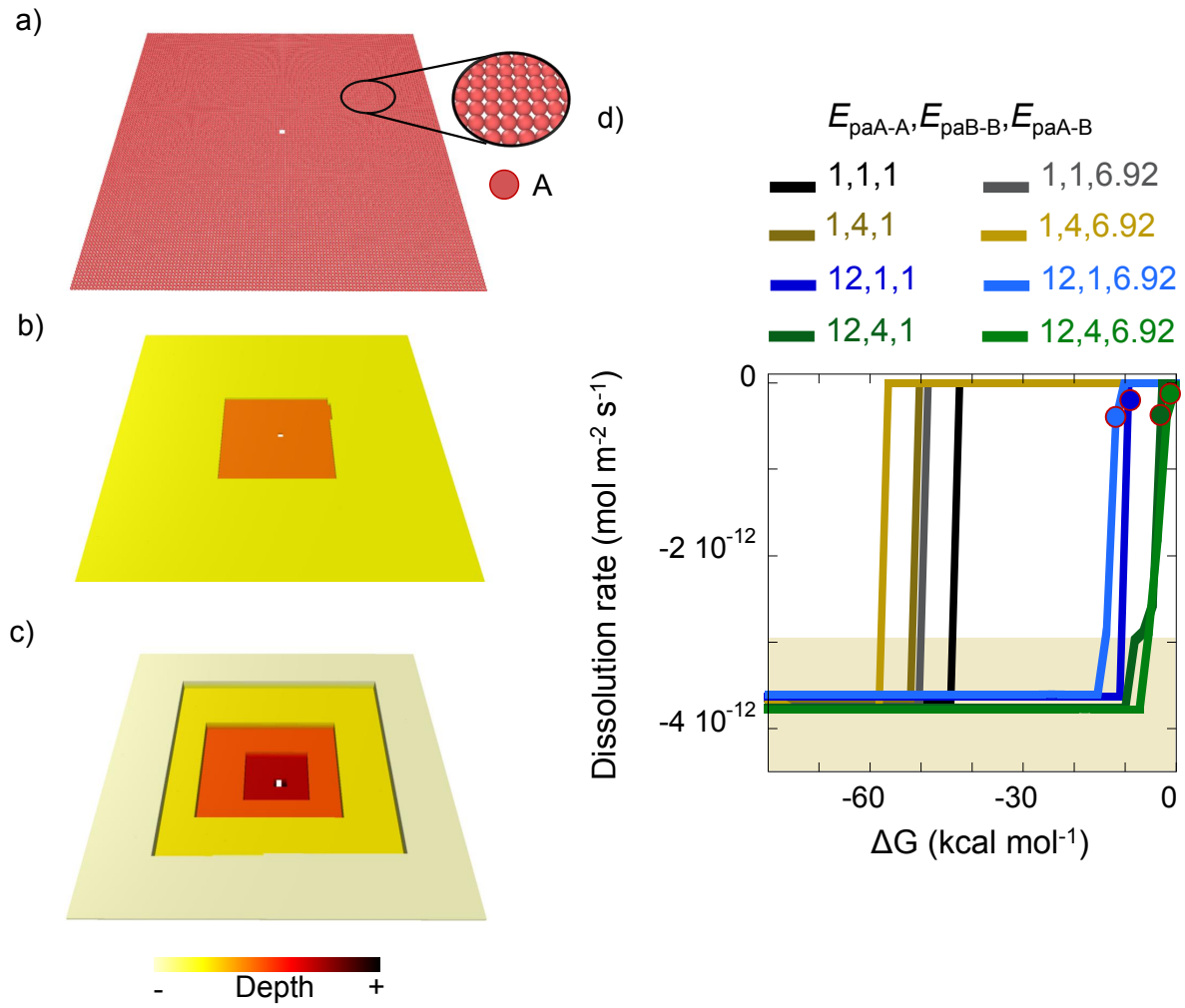

Figure 4.10: **Study in configuration D2**. a) Initial surface system. b) Typical dissolution pattern during the dissolution at far from equilibrium conditions. c) Particular topography given in blued and greenish cases at the beginning of the onset (red rounded points in the graphic) when B and A atoms have similar dissolution likelihood. d) Dissolution rate versus ΔG for both A and B atoms. Orange area shows the dispersion of the dissolution plateau values.

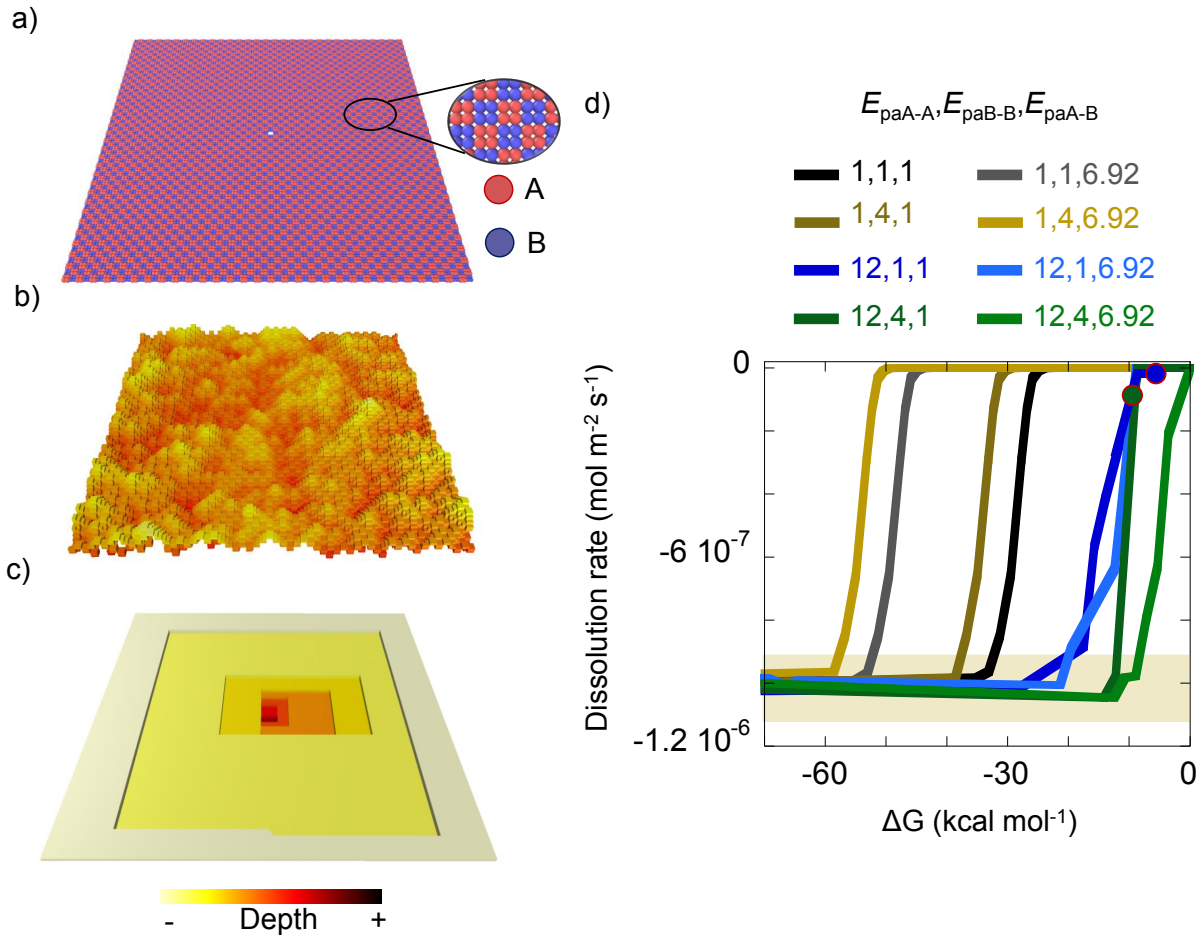

Figure 4.11: **Study in configuration E2**. a) Initial surface system. b) Typical dissolution pattern during the dissolution at far from equilibrium conditions. c) Particular topography given in dark blue and dark green cases at the beginning of the onset (red rounded points in the graphic) when B and A atoms have similar dissolution likelihood. d) Dissolution rate versus ΔG for both A and B atoms. Orange area shows the dispersion of the dissolution plateau values.

The onset in all the cases is produced when they start to dissolve. A particular topography is given at the beginning of the onset in cases where A and B atoms has similar likelihood to dissolve. (dark blue and dark green cases in figure 4.2c,d). In this case the topographic effect of the dislocation gains importance and the smooth layers are sequentially removed by step retreat. This dissolution mode quickly disappears with a small deviation from equilibrium.

4.3.12 Configuration F2

The random distribution of grains of 2x2x2 A or B atoms in a mineral is studied (see figure 4.1f). The compilation of the dissolution rate dependence for B atoms with ΔG is shown in figure 4.6c. The topography in figure 4.12b follows a similar behaviour to configuration F studied before (see section 4.3.6). It shows a random pattern produced by the dissolution of B atoms where the dislocation has no influence. Nevertheless, A atoms do not dissolve in this case. As we cannot assure that this topography is possible without reconfiguration, we only report the dissolution rate at the very initial stages. Since dark coloured cases present dissolution at $\Delta G = 0$, minerals with such characteristics would be difficult to be found in nature.

4.4 Conclusions and outlook

In this chapter we have studied the dissolution of a general Kossel crystal consisting of two elements, A and B. 12 different configurations, along with 8 different sets of energy barrier values, have been considered in this systematic study to elaborate a mapping of the dissolution rate dependence with ΔG and their topographical features. Some configurations show expected results by comparing them with the study in a single element Kossel crystal in chapter 2. Results show that both the distribution and the energy values determine the dissolution rate, which could differ between elements leading to a incongruent dissolution. Moreover, the dissolution rate onset may be produced, apart from the known dislocation opening effect, by the disparity of the activation of the dissolution of each element at different ΔG conditions. In this sense, we have suggested that glasses and amorphous

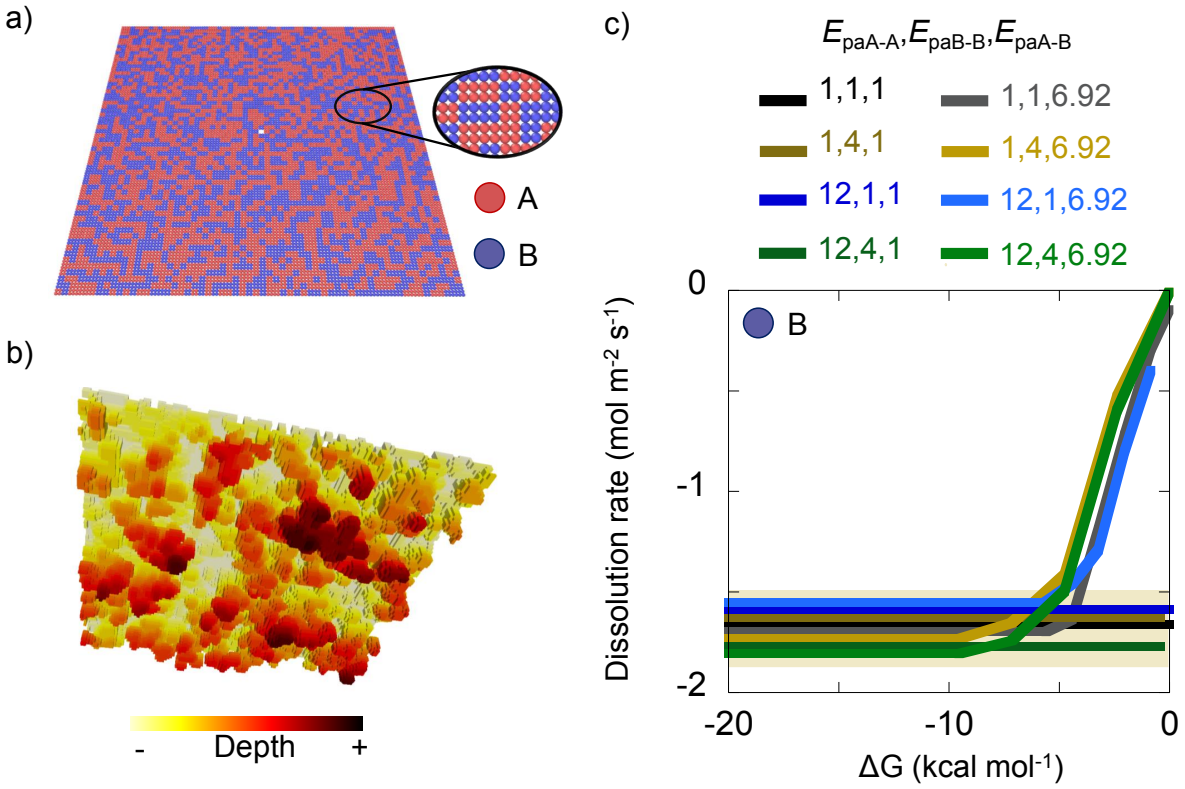

Figure 4.12: **Study in random configuration F2**. a) Initial surface system. b) Typical dissolution pattern during the dissolution at far from equilibrium conditions. Bottom view of the reactive surface is shown for visualization purposes. c) Dissolution rate versus ΔG for B atoms. Orange area shows the dispersion of the dissolution plateau values.

alloys could present two (or more) well differentiated dissolution rate onsets. Finally, our model is able to recognise the unfeasibility of some of the configurations and energy values.

Though there is place to improvement in more elaborated models with finer detail, the results of this chapter are expected to serve as checking of the validity in future studies, or to foresee phenomena emerging for other configurations or value sets. In this sense, a major concern relies on the effect of impurities and other point defects in the mineral structure. Although we can get an idea of the dissolution rate taking into account that B atoms could be treated as gaps in a limit case, a more complete study can be performed with the defect and impurity densities, or with certain structures. Moreover, the capability of KIMERA to elaborate coarse grained models will help to extend the studies to greater scales, which are especially important in industrial applications.

Chapter 5: The Dissolution of Quartz

5.1 Introduction

Silicates constitute the most abundant group of minerals in the Earth's crust and their interface with water covers a 71 % of the earth surface [107]. Besides, the wide use of the different silicate polymorphs for industrial purposes such as semiconductors [147], construction [148], insulation [37] or chemical catalysis [42,149] has encouraged the study of its interaction with water [3,6,72]. In this sense, several studies have focused on the hydration of one of the most abundant and ubiquitous polymorph, quartz (see equation 5.1).

$$SiO_2\ (s) + 2H_2O \rightarrow H_4SiO_4\ (aq) \tag{5.1}$$

Experimentally, the variation of dissolution rates with pH [1,3,150], temperature [1,17,19] or Gibbs free energy (ΔG) [20,46] have been widely studied thanks to the improvement of experimental techniques such as atomic force microscopy (AFM) (see section 1.3.2.3) [20,72,151]. The dissolution rate of quartz is low due to a high activation energy of 90.1 ± 2.5 kJ mol^{-1} [6,19] which remains almost constant no matter the plane under consideration [17,151]. The dissolution rate varies with pH follows a U shape curve with the minimum at pH $\simeq$ 4.8 (see figure 1.6) [3]. Other effects have been investigated, as the dissolution enhancement by salts of NaCl, KCl, LiCl or $MgCl_2$ [59], the variety of etch pit shapes depending on the plane and solvent [17,18,20,72,151–153] or the constant dissolution rate with the dislocation density [46]. In general, experiments have identified the nanoscale as the origin of the macroscopic dissolution dynamics. At this scale, atomistic simulations represent a powerful tool to study and verify the specific mechanisms involved. Simulations have achieved several milestones. First, *ab initio* calculations have been carried out to obtain the energy barrier of the main reactive sites of quartz [22,23,32,44,45,107,154–158] and hence to identify the limiting

reactions which govern the dissolution process according to the transition state theory (TST) [6]. Besides, they have revealed the importance of the structural network strength and stability provided by the Si-O-Si [156] and by the hydrogen bonds formed at the quartz-water interface [44].

Second, Monte Carlo simulations have confirmed the stepwise mechanism ($Q_4 \rightarrow Q_3 \rightarrow Q_2 \rightarrow Q_1 \rightarrow Q_0$) as the preferential way for quartz dissolution [107]. Here the Q_n notation represents the number of bridging oxygen atoms a Si atom has. A bulk site with four bridging oxygen atoms (Q_4) loses them one by one in hydrolisys reactions until it is released in the form of free silicic acid $Si(OH)_4$ (Q_0) (see figure 5.1). Kurganskaya and Luttge [16] gathered these effects and bibliography energy barrier values to develop a KMC model able to reproduce the experimental topographies in different planes and conditions by modifying certain mechanistic parameters (see section 3.4).

Unfortunately current KMC models are not able to reproduce jointly the experimental activation energy and dissolution rate. An activation energy of $E_a \sim 149$ kJ mol^{-1} [45], much greater than the experimental one of $87-92$ kJ mol^{-1} [19], would be necessary to get the experimental dissolution rate of $\sim 10^{-13}$ mol m^{-2} s^{-1} at 300 K. The other way around, by considering the experimental activation energy $E_a \sim 90$, the dissolution rate would be much higher $\sim 10^{-2}$ mol m^{-2} s^{-1}. Pelmenschikov *et al.* [23] suggested the existence of a self healing effect, where a precipitation step could explain a reduction of the net dissolution rate keeping the low activation energy.

The main objective of this chapter is to explain the inconsistency between the dissolution rate and activation energy of α-quartz, altogether with the etch pit morphology on the surface. For that we consider a sequential and independent breakage of bridging oxygen bonds. Moreover, using the model described in chapter 2, we have obtained its dissolution rate dependence with Gibbs free energy.

5.2 Theory

As explained in chapters 1 and 2, the reaction rate in KMC is computed using an Arrhenius equation (see equation 1.26) [6]:

$$r'_{\mathrm{D}} = f_{\mathrm{D}} \cdot \exp\left(-\frac{E_{\mathrm{D}}}{k_{\mathrm{B}} \cdot T}\right) \tag{5.2}$$

where r'_{D} is the rate for the dissolution reaction to happen (s^{-1}), E_{D} is the energy barrier (J mol^{-1}) and f_{D} is a pre-exponential factor that represents the frequency with which the system tries to overcome that barrier (s^{-1}). The pre-exponential is determined by the amount of reactive sites and the time needed to activate them, following the equation [6]:

$$f_{\mathrm{D}} = C_{\mathrm{s}} \cdot X_{\mathrm{H_2O}} \cdot \frac{k_{\mathrm{B}} \cdot T}{h} \cdot \frac{q^{\ddagger}}{q^{\mathrm{P}}} \tag{5.3}$$

where C_{s} is the number of reactive sites on the surface, $X_{\mathrm{H_2O}}$ is the fraction of them occupied by water molecules, $k_{\mathrm{B}} \cdot T/h$ is the called fundamental frequency (see equation 1.23) with h the Planck constant, and q are the partition functions of the transition state $q^{\ddagger}$ and the precipitated state q^{P} (see figure 5.1). Typically the partition function ratio for most minerals is equal to the unity since the vibrational frequencies of the solid are similar to vibrational frequencies in the transition state and therefore $q^{\ddagger} = q^{\mathrm{P}}$. Nevertheless, for minerals with rigid frameworks like the quartz, where the motion of the atoms is strongly constrained by the vicinity, the ratio may be much lower with $q^{\ddagger} << q^{\mathrm{P}}$. For quartz, an approximated partition function was obtained from the vibrational frequencies ν (s^{-1}) of the activated complex (the transition state ‡) and the adsortion complex (the precipitated state P) of disiloxane hydrolysis by *ab initio* calculations (see equation 1.32) [6, 24] .

$$\frac{q^{\ddagger}}{q^{\mathrm{P}}} = \frac{\Pi_l \left(1 - \exp\left(-\frac{h \cdot \nu_l^{\mathrm{P}}}{k_{\mathrm{B}} \cdot T}\right)\right)}{\Pi_l \left(1 - \exp\left(-\frac{h \cdot \nu_l^{\ddagger}}{k_{\mathrm{B}} \cdot T}\right)\right)} \tag{5.4}$$

Equation 5.2 reports the dissolution at far from equilibrium conditions since no precipitation is happening. Close to equilibrium, precipitation effect gain importance and therefore a precipitation term needs to be considered to get the ΔG dependence (see section 2.2).

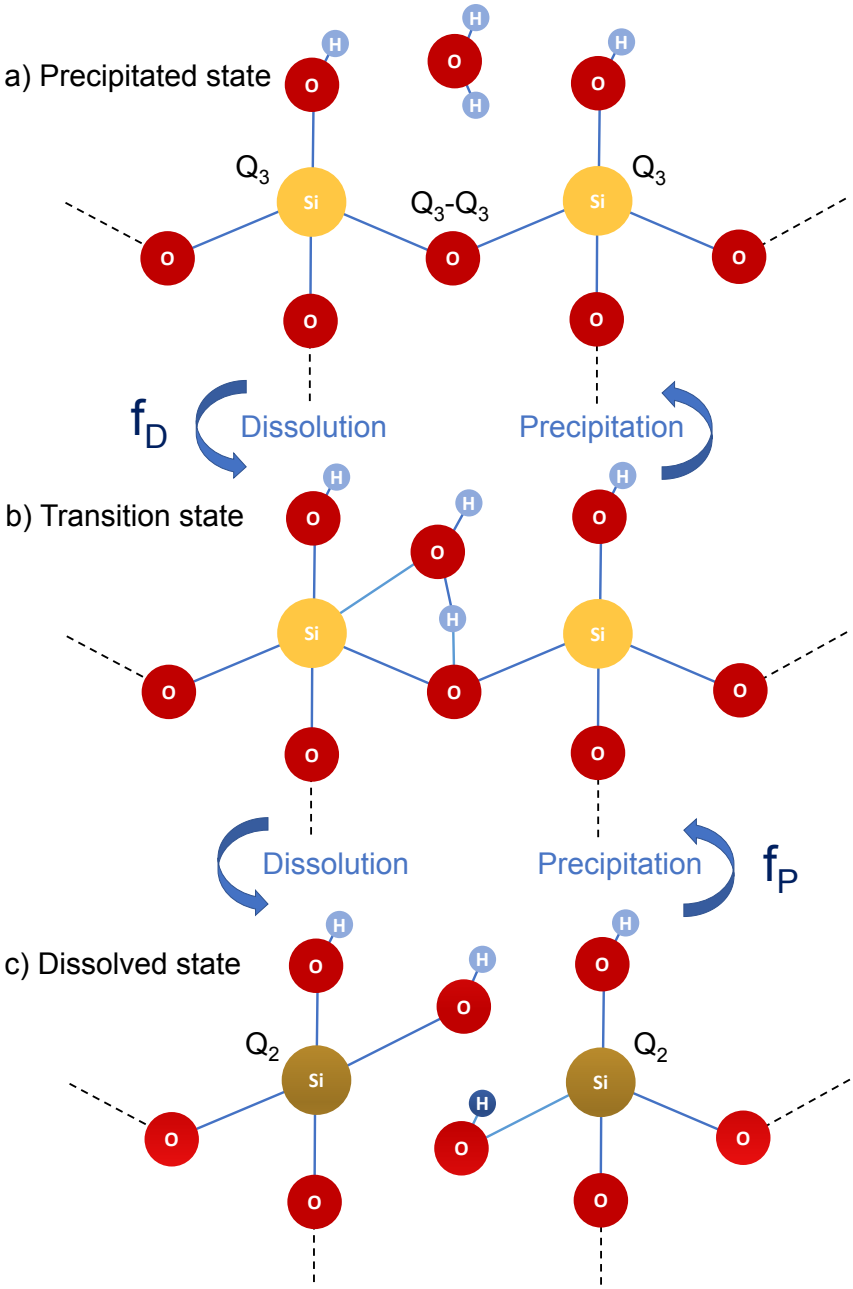

Figure 5.1: **Dissolution and precipitation of quartz**. Schematic representation of bond breakage (and formation) process in quartz. a) A water molecule gets close to the linked oxygen atom in a Q_3-Q_3 position. b) The transition state represents the limiting step to overcome. c) The water molecule transfers its protons to break the joining bond to form two Q_2 silicon atoms. f_D and f_P are the frequencies with which the system tries to break an form the bond respectively.

$$r'_{\mathrm{P}} = f_{\mathrm{P}} \cdot \exp\left(-\frac{E_{\mathrm{P}} - \Delta G^{*}}{k_{\mathrm{B}} \cdot T}\right) \tag{5.5}$$

which is analogous to equation 5.2 and it becomes important at close to equilibrium conditions when local Gibbs free energy ΔG^{*} (kJ mol^{-1}) is close to 0. The precipitation pre-exponential f_{P} has a similar expression to f_{D} (equation 5.3), but may not be necessarily the same since dissolution and precipitation states may have different vibrational frequencies (see figure 5.1). To recapitulate:

$$r'_{\mathrm{D}} = C_{\mathrm{S}} \cdot X_{\mathrm{H_2O}} \cdot \frac{k_{\mathrm{B}} \cdot T}{h} \cdot \frac{q^{\ddagger}}{q^{\mathrm{P}}} \cdot \exp\left(-\frac{E_{\mathrm{D}}}{k_{\mathrm{B}} \cdot T}\right) \tag{5.6}$$

$$r'_{\mathrm{P}} = C_{\mathrm{S}} \cdot X_{\mathrm{H_2O}} \cdot \frac{k_{\mathrm{B}} \cdot T}{h} \cdot \frac{q^{\ddagger}}{q^{\mathrm{D}}} \cdot \exp\left(-\frac{E_{\mathrm{P}} - \Delta G^{*}}{k_{\mathrm{B}} \cdot T}\right) \tag{5.7}$$

Quartz dissolution in pure water is a clear example of a surface limiting reaction over a wide range of temperatures [57]. The concentration close to the surface is expected not to be influenced by a macroscopic concentration gradient within the diffusive layer (see case 2 in figure 1.4). Nevertheless, at positions on the surface, it is expected to be deviated by the quartz dissolution or precipitation susceptibility, that is, the relation between E_{D} and E_{P} (see section 2.2.1). Local ΔG^{*} can be directly related with the macroscopic ΔG by the expression 5.8 taking into account that the dissolution and precipitation rates, r'_{D} and r'_{P} are equal when $\Delta G = 0$.

$$\Delta G = \Delta G^{*} + E_{\mathrm{D}} - E_{\mathrm{P}} - \ln \frac{f_{\mathrm{D}}}{f_{\mathrm{P}}} \tag{5.8}$$

The macroscopic ΔG is experimentally calculated from the ratio of the ion activity product Π of the dissolved material in water and the thermodynamic solubility product K_{s}. In the case of quartz it is possible to use the concentration ratio because the activity of silicic acid is close to unity (see section 1.2.1) [20, 24].

$$\Delta G = R \cdot T \cdot \ln\left(\Pi / K_{\mathrm{s}}\right) = R \cdot T \cdot \ln\left(C / C_{\mathrm{e}}\right) \tag{5.9}$$

where C and C_e are the measured and equilibrium concentration of H_4SiO_4 respectively (mM).

The final aspect to be considered is the determination of E_D and E_P. According to Lasaga and Luttge the dissolution and precipitation energy barriers for a site in the surface E_D and E_P can be written as the sum of the contribution of the n surrounding bonds (see equation 1.43) [81].

$$E_D = \sum_{i=1}^{n} E_{di} \quad E_P = \sum_{i=1}^{n} E_{pi} \tag{5.10}$$

This equality arises from the 'flickering-bond' model to mimic the bond breakage-reformation processes in one step; the net dissolution probability is the conditional probability of every single bond breakage. As approximation, most works have considered to have a lineal contribution (see equation 1.37) [16,61,81,115,142]

$$E_D = E_d \cdot n \quad E_P = E_p \cdot n \tag{5.11}$$

Kurkanskaya and Luttge's work [16] studied the quartz dissolution with both models in equations 5.10 and 5.11 at far from equilibrium conditions and evinced the role played by the surface relaxation and hydrogen network (tessellation) [44], adding to the surface an stabilization against dissolution able to change the morphology of opening etch pits (see section 3.4). Nevertheless, such models overestimate the activation energy. The approximation taken in the models of conditional probability is not suitable for quartz dissolution since at far from equilibrium conditions there would not be the effect of bond reformation. In the next section, a model with similar consideration as taken by Nangia and Garrison [107] with sequential and independent detachment of bridging bonds is presented.

5.3 Model and methods

The mechanism of dissolution consists of the sequential hydrolysis of oxygen bond forming the Si-O-Si network [107,159] (see figure 5.1). Each oxygen atom reaction can be considered as independent of the previous one. Thus, the possible event for a Q_n-Q_m bonding oxygen atom is to react forming

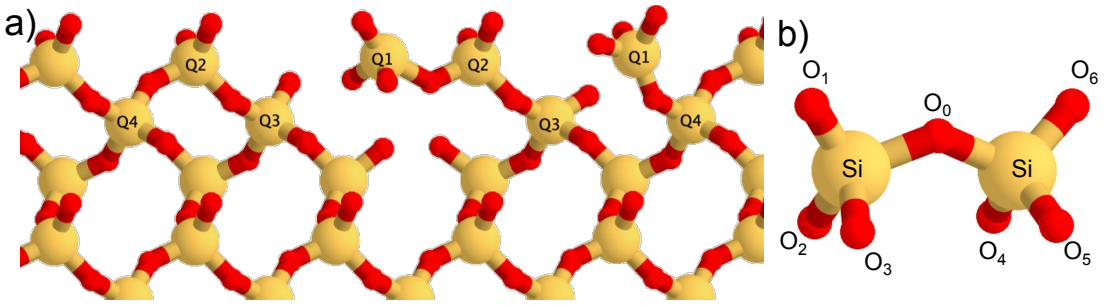

Figure 5.2: **Quartz bond structure**. Si-O-Si bond distribution and surroundings within the α-quartz structure.

two Si sites Q_{n-1} and Q_{m-1}. Once the last oxygen atom surrounding a silicon atom has reacted, the silicon atom is released in the form of silicic acid $Si(OH)_4$. *Ab initio* calculations report a wide range of energy values for the oxygen bond hydrolysis [22, 23, 154–158] . Despite the wide range of values reported, three aspects can be inferred. First, there is a great difference between the energy barriers computed for relaxed clusters, where the atoms positions and angles are let reach a minimum energy state [154, 155], and non-relaxed clusters [22, 23, 156–158]. Secondly, there is a difference depending on the connectivity of the silicate units. And finally, E_P is approximately a 20% lower than E_D for Q_1-Q_m ($m \in [1,4]$) and approximately equal to E_D for Q_2-Q_4. Such differences highlight the dependence of the hydrolysis energy barrier with the surroundings.

In this work, we consider the above mentioned connectivity by evaluating the number of unreacted oxygen atoms around the oxygen atom of interest. All of them are in a cutoff distance of 2.58 ± 0.01 Å. If one hydrolysis reaction occurs in one of these neighbouring linking oxygen atoms, the bond breaks reducing the connectivity and, consequently, the energy barrier for the hydrolysis of the oxygen atom of interest. To account for the breakage, in the simulation the linking oxygen atom just disappears from the system. This way we can define the energy barrier for a hydrolysis as a function of the surrounding oxygen atoms. We take the non-relaxed energy barrier values reported by Pelmenschikov *et al.* [22, 23] since they represent the longest data set with self-consistency. Bibliographic and model values are presented in table 5.1.

Two approximations are needed to solve the lack of certain values. First, a Q_2-Q_2 and a Q_1-Q_3 site, a Q_1-Q_4 and a Q_2-Q_3 site, and a Q_3-Q_3 and a Q_2-Q_4 site are energetically equivalent because

Bond	Bibliografic E_D	Bibliografic E_P	E_D	E_P	Surrounding oxygen atoms
Q1-Q1	71 [22]		-	-	0
Q1-Q2	157' [154]	122' [154]	75	60	1
Q1-Q3	102' [155] 112 [156] 152' [154]	116' [154] 128' [155]	85	70	2
Q1-Q4	92 [22] 94 [157] 100 [23] 155' [154]	60 [157] 110 [23] 112' [154]	95	80	3
Q2-Q2	138' [155]	141' [155]	85	70	2
Q2-Q3	206' [155]	187' [155]	95	80	3
Q2-Q4	105 [23] 131 [157]	110 [23] 131 [157]	105	105	4
Q3-Q3	162 [158]		105	105	4
Q3-Q4	138 [22]		135	135	5
Q4-Q4	200 [22]		-	-	6

Table 5.1: **Model values**. Energy barrier values with the bond surroundings in kJ mol^{-1}. ' indicates values for relaxed configurations. There is a preference for Pelmenschikov *et al.* values [22, 23].

they have the same number of surrounding oxygen atoms. Second, to authors knowledge E_P values for Q_3-Q_3 and Q_3-Q_4 have not been reported, so the same values than for E_D are taken.

Simulations are performed in α-quartz in {001}, {100} and {101} planes. Around 5 million atoms are distributed in a system of 240x240x10 unit cells for the {001} plane, 70x100x70 for the {100} plane and 80x80x80 for the {101} plane. The surface areas are $\sim 1.25 \cdot 10^{-14}$ m^2, $\sim 1.92 \cdot 10^{-15}$ m^2 and $\sim 2.28 \cdot 10^{-15}$ m^2 respectively. With one dislocation per system, dislocation densities of $5.2 \cdot 10^{14}$ m^{-2}, $4.4 \cdot 10^{14}$ m^{-2} and $8 \cdot 10^{13}$ m^{-2} are respectively considered, which lay within the range of experimental values (10^9 - 10^{14} m^{-2}) [46, 160]. Finally, periodic conditions are considered and only surface atoms can react. All the data visualization has been made using OVITO program [8].

As we said before, the surface relaxation and the formation of hydrogen bond network may change drastically the energy barrier value of the hydrolysis reaction (see table 5.1) and provide an extra stabilization able to change the morphology of the opening etch pits (see section 3.4) [16]. As limit case for all the simulations, and following the work by Kurkanskaya and Luttge, the terrace atoms, or atoms on the surface out of the dislocation, are considered not to react.

The '.xyz' file containing the quartz unit cell [161], and the input files needed to run the simulations in {001} plane are included in appendix A.3.

5.3.1 Input for the KIMERA code

In this section the necessary steps to create the simulations into KIMERA program are indicated. In the following we describe the free dissolution case in {001} plane at 473 K (see appendix A.3.1):

- **System dimensions**. A box is created with 240x240x10 units cells is created with PBC along a and b axes.

- The **unit cell parameters**. $a = b = 5.01$, $c = 5.47$, $\alpha = \beta = 90^\circ$ and $\gamma = 120^\circ$. The '.xyz file is called, but in this case, in contrast to the section 3.5 example, the oxygen atoms do play an important role and they cannot be removed.

- We define a **target step** $S_{\text{target}} = 1000000$ which is approximately a quarter of the amount of silicon and oxygen atoms forming the system and it is enough to get results of its evolution.

- **Topographic defects**. We define in the center of the plane a dislocation and inner atoms removed from the initial surface.

- **Event definition**. The $E_{\text{D}}(n)$ and $E_{\text{P}}(n)$ for the linking oxygen bond is directly related with the number of oxygen atoms within 2.585 Å (see table 5.1). The presence of 6 surrounding oxygen atoms indicates that the considered one is in a bulk position and, therefore, it is not reactive. Besides, a silicon atom must be automatically released if all of its four surrounding oxygen atoms have reacted. Finally, the fundamental frequency values $f_{\text{D}} = f_{\text{P}} = 2.45 \cdot 10^{10}$ s^{-1} are used [24]. The $\Delta G^* = -200\ k_{\text{B}}T$ value sets very far from equilibrium conditions.

The next step is to determine the relation between ΔG^* and ΔG. From the '.meandiscoord' file, most oxygen atoms react when three oxygen atoms are around ($\overline{n} = 3$). That means that the reference position to determine the ΔG value is a Q_1-Q_4 site. The energy barrier for this site is $E_{\text{D}} = 24.1$ and $E_{\text{P}} = 20.3\ k_{\text{B}}T$ units at 473 K (see table 5.1). Therefore, the relation between ΔG^* and ΔG is as follows in equation 5.12

$$\Delta G(k_B T) = 1.0 \cdot (\Delta G^* + (24.1 - 20.3)) = \Delta G^* + 3.8 \tag{5.12}$$

Note that with this model the number of broken bonds is $\overline{N}_i = 1$ (see equation 3.5), not like in the SCS-L1 model shown in section 3.5 where the broken bonds corresponded to the number of surrounding silicon atoms.

5.4 Results

Three aspects of α-quartz are studied: the morphology of etch pits, the dissolution rate dependence with temperature and the dissolution rate dependence with ΔG.

Before moving to them and in order to get the correct dissolution rate, calculating the pre-exponential factors f_D and f_P (see equations 5.6 and 5.7) is necessary. C_s, or the density of reactive sites, is implicitly considered in the simulation system. X_{H_2O}, or the fraction of sites that are attacked by water molecules within a $k_B \cdot T/h \cdot q^{\ddagger}/q^P$ time, is related to the activity coefficient, thus, it is expected to be close to the unity $X_{H_2O} = 1$ [20, 24]. $q^{\ddagger}/q^P$ or the ratio of frequencies between the equilibrium and the activated complex can be calculated from the data reported by Casey for the frequencies of disiloxane-water cluster [6, 24] and is presented in table 5.2.

An equivalent procedure has to be followed to calculate f_P. Although this quantity is not important at far from equilibrium conditions, the relation f_D/f_P may determine the dissolution rate at close to equilibrium ones (see equation 5.8). Up to authors' knowledge $q^{\ddagger}/q^D$ have not been reported. As the system is expected to be equally constrained by the rest of the structure in the dissolved state as in the transition state (see figure 5.1b and 5.1c), this quantity should be close to the unity $q^{\ddagger}/q^D = 1$. Although we have used this ratio, we have also studied the limit case when $q^{\ddagger}/q^D = q^{\ddagger}/q^P$ ($f_P = f_D$) for comparison.

T(K)	$\frac{q^{\ddagger}}{q^{\mathrm{P}}} \cdot 10^{-3}$
300	7.84
400	3.74
473	2.48
500	2.18
600	1.45
700	1.05
800	0.81
900	0.65

Table 5.2: **Partition function values with temperature**. Values calculated with equation 5.4 and table 1 in [24].

5.4.1 Dissolution patterns

Experimental dissolution patterns formed in α-quartz have been subject of study in several experimental works [16–18, 20, 72, 151, 153] as they could be a way of recognising immediately the crystallographic plane or the pH and temperature conditions to which dissolution takes place. It must be taken into account that some patterns may be produced due to a higher scale effect, as for example macroscopic fractures or a fluctuating concentration of material. Figure 5.3 reports the dissolution patterns obtained from our simulation in free dissolution and with stabilization (no reacting terraces) at far from equilibrium conditions and temperatures of 300 K and 900 K. Starting from a perfect plane with one dislocation in the system, the snapshots are taken in the best time to appreciate the characteristic topography. There is an excellent match between the patterns reported with the considered model and the obtained experimentally. At 300 K in the {001} plane, the free dissolution presents molecular chains oriented along the [100], [010], and [110] crystallographic directions in a similar way than figure 3.3c or figure 3.4c. By applying the stabilization, V-shape striations are produced along the [110] direction. By increasing the temperature the striations broaden. Striations have been reported by Luttge in hydrothermal conditions though the recognition of its plane or direction was not possible [16]. For the {100} plane, the dislocation slightly involves a preferential site for the dissolution following a rectangular pyramidal shape with long sides along

[010] direction. The stabilization clarifies this shape and it transforms into a circular one at high temperature. This shape has been reported in the {100} plane both in KOH solution [17,72,151] and in water [20]. Finally in the {101} plane similar effect to the previous one is produced but the pit shape is distorted into a trapezoidal semipyramidal one with parallel sides along [010] direction, which has been reported for the {101} plane in KOH solution [18,153].

It has been checked in all cases that the selection of planes with Q_2 or Q_3 terminations with the stabilization does not imply any change in the pit shape.

The increase of temperature provokes, on the one hand, randomness in free dissolution and, on the other hand circular shapes with stabilization. These effects are expected since the difference between exponential terms for the reactive atoms is reduced and, therefore, the dissolution is homogenized. Besides, the tessellation effect has been demonstrated essential to reproduce the correct dissolution patterns in quartz.

Other experimental topographies like V shape pits for {100} plane or triangular and pentagonal ones for {101} plane are not found in our simulations [16], which suggests that they are due to macroscopic conditions or effects not considered here like fractures or fluctuating ion concentrations in the solvent.

One remarkable side effect of the pits topography, apart from the recognition of planes and conditions of dissolution, is that it is possible to get an idea of energy barrier relation of the exposed sites. For example, in the {100} case rectangular shapes are produce, because in the long sides of the pit most of the oxygen atoms are in a Q_3-Q_4 position meanwhile in the short ones, most of them are in a Q_2-Q_4 position. The closest the relation between the energy barrier of these two sites, the more squared the shape of the pits (or circular if they have an equal low value). Similarly, the higher the difference, the more elongated the rectangular pit is. In a extreme case, V-shaped striations may be produced. This energy barrier change is expected in catalytic conditions or with pH variations. [16,45,154]. We cannot say the same about the {101} case. All sides of the pit have similar density of Q_2-Q_4 and Q_3-Q_4 sites and therefore no different energy barrier relation could change the pit shape into a triangular or pentagonal one.

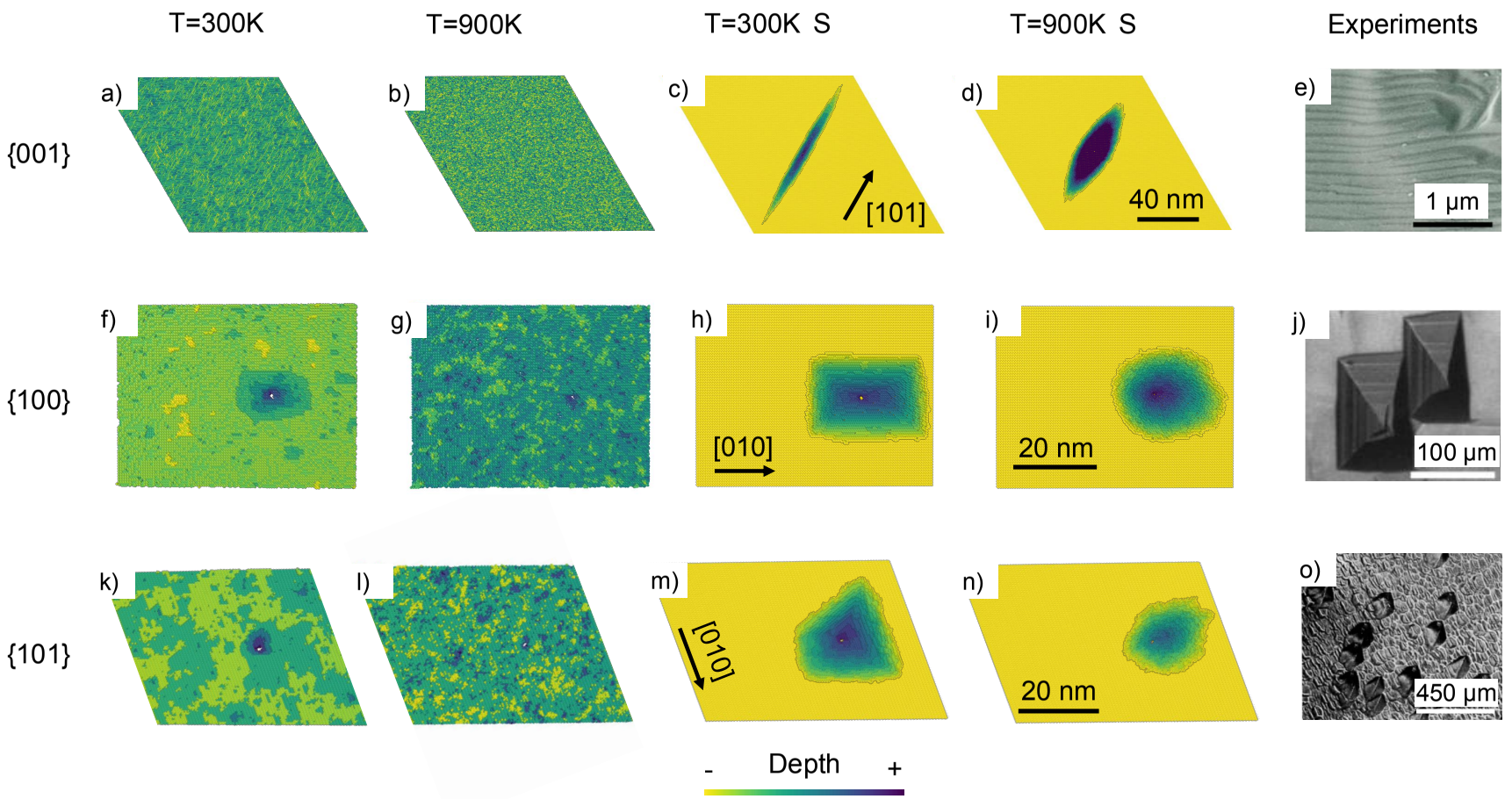

Figure 5.3: **Quartz dissolution patterns**. Topography and etch pit shape for {001}, {100} and {101} planes in free dissolution and with stabilization (S) at 300 and 900 K. The shapes are: a) Small molecular chains along the [100] [010] and [110] directions. b) Random dissolution pattern. c) Elongated V-shape pit. d) Ellipsoidal V-shape pit. e) Striations formed on quartz dissolved at hydrothermal conditions [16]. The face and direction could not be identified. f) Fuzzy rectangular pyramidal pit at the dislocation. g) Random dissolution pattern. h) Rectangular pyramidal pit at the dislocation. i) Circular pit at the dislocation. j) Rectangular pyramidal pits formed at the {100} plane etched by KOH [17] k) Fuzzy trapezoidal semipyramidal pit at the dislocation. l) Random dissolution pattern. m) Trapezoidal semipyramidal pit at the dislocation. n) Semielliptical pit at the dislocation. o) Trapezoidal semipyramidal etch pits observed on {101} face etched by KOH [18].

5.4.2 Dissolution rate with temperature and activation energy

The global (or apparent [6]) activation energy for a dissolving mineral is calculated from the Arrhenius equation as the slope of the natural logarithm of the dissolution constant ($\ln k$) versus the inverse of temperature ($1/T$) (see section 1.2.3).

$$k = A' \cdot \exp\left(-\frac{E_a}{R \cdot T}\right) \tag{5.13}$$

In the case of quartz the activation energy is only affected by the limiting reactions taking place in the surface since transport of the dissolved material does not act as limitant in a wide range of temperatures (see figure 1.5) [57]. The energy barrier of this reactions changes locally depending on the surroundings, as shown in the model section, and each surface may have a different activation energy. Experiments have reported a narrow difference in between activation energy of 87 kJ mol^{-1} in the {101} plane and 90 kJ mol^{-1} in the {100} plane in KOH solutions [17,151]. Usually experiments are done using grains, where all the different planes contribute to the overall activation energy (see section 1.2.5). In addition, it is necessary to highlight that the pre-exponential factor f_D also affects it since it changes with temperature (see table 5.2).

Before getting the activation energy results it is necessary to point out what criterion has been taken for the dissolution rate measures since it is no constant. During dissolution there is a short period of inactivity when first exposed Si-O-Si bonds break but no silicon atoms are released. After this period, the silicon dissolution rate increases quickly to finally reach a steady state. The data is taken from this steady slope (see red line in figure 5.4a). A different approach must be considered for the dissolution with stabilization. Since only very few Si-O-Si bonds are initially exposed to dissolution, the initial inactivity period is much smaller, almost nonexistent. Then the dissolution rate increases gradually reaching a maximum rate value when the pit has coalesced. The surface stabilization effect is lost and the dissolution rate converges on the free dissolution case. The quickness of the coalescence is determined by the etch pit shape and the plane. In the {001} plane the lineal striations coalesce slower than the rectangular or the trapezoidal pits in the {100} or {101} planes, since it

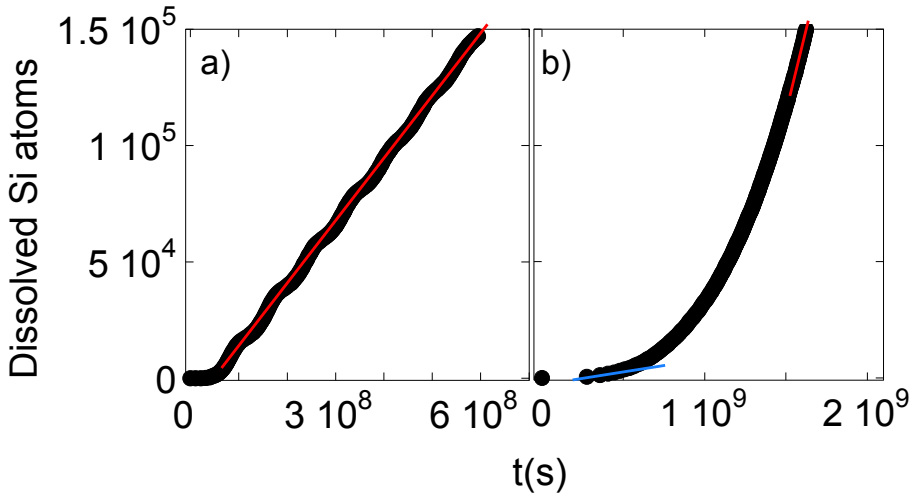

Figure 5.4: **Criteria to get the dissolution rate.** Released silicon atoms with time in {100} plane at 300K. a) Free dissolution. The slope of the red line is the upper limit dissolution rate. b) Stabilized. The slope of the blue line is the bottom limit dissolution rate. The slope of the red lines are the same.

takes more time to cover all the surface. Due to the impossibility to know when the experimental measurements are taken, the case where the pits have just opened has been considered. The slope is taken from the very first points when the silicon atoms have started to dissolve (blue line in figure 5.4b). Note that the needed time for the system to dissolve is in the order of years, hence it probably represents a valid limit case to compare with experiments.

In figure 5.5a reported values of the dependence of dissolution rate with temperature at far from equilibrium conditions for the three α-quartz planes, with and without stabilization, are compared with the experimental rates reported in pure water (pH= 7) [19]. The values obtained in this work for the activation, presented in table 5.3, are slightly higher than the experimental activation energy $E_{\text{a.exp.}} = 90.1 \pm 2.5$ kJ mol^{-1}. The global activation energy has been taken as the middle value between top and bottom ones; $E_{\text{a}} = 94.7 \pm 1.9$ kJ mol^{-1}. As seen, there is a small difference among the six cases. Besides, experimental rates are within the simulations range and change from $\{101\} < \{100\} < \{001\}$ to $\{001\} < \{100\} < \{101\}$ when considering stabilization. This matches with the change in the surface stabilization calculated by DFT [162]. However, this match may be accidental since other works have found no relation between dissolution rate and surface energies in other minerals like β-belite, γ-belite and alite [43, 126, 127].

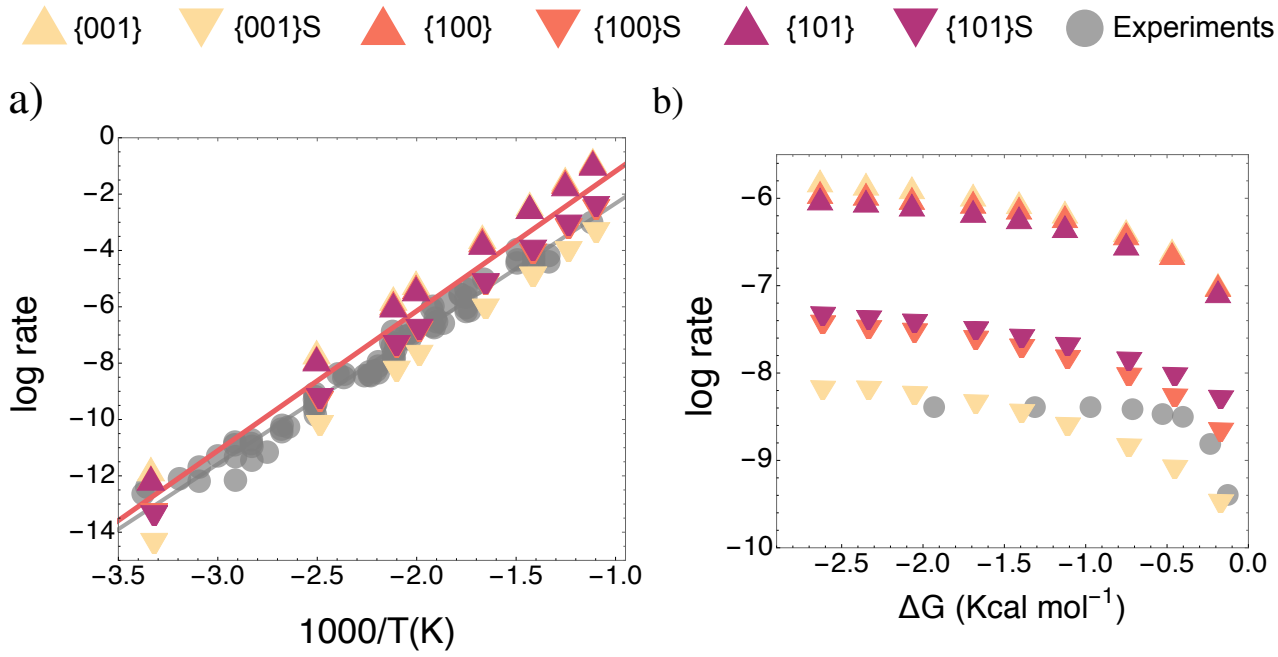

Figure 5.5: **Dissolution rate with temperature and ΔG.** Comparison of the experimental data with the proposed α-quartz dissolution model for {001}, {100} and {101} planes with and without stabilization (S). a) Dissolution rate with temperature. Grey points are experimental ones at pH $= 7$ [19]. From the slope of coloured triangular points is calculated the activation energy in each case in table 5.3. b) Dissolution rate with ΔG. Grey points are experimental ones at pH $= 5.7$ and $T = 473$ K [20].

Plane	Simulation E_a
{001}	94.4 ± 0.2
{001} S	94.9 ± 0.3
{100}	96.4 ± 0.2
{100} S	93.1 ± 0.3
{101}	96.2 ± 0.3
{101} S	94.6 ± 0.2
	$E_a = 94.7 \pm 1.9$

Table 5.3: **Activation energies**. Measured activation energies in each plane from figure 5.5a.

The activation energy result has an important implication. The self healing effect suggested by Pelminschekov et al. [23], although it is important at close to equilibrium conditions, is no needed to explain the discrepancy between the experimental value and the reported for the limiting step of Q_2-Q_4 breakage. According to their work, the fact that the Q_2-Q_4 site has the same energy barrier for the formation than for its breakage and presumably with higher frequency ($f_P > f_D$) would change the limiting step to the breakage of a Q_1-Q_4 site. Nevertheless, by considering far from equilibrium conditions, no bonds reformation or dehydroxylation is allowed, and such proposed mechanism does not happen. Our simulations recognise in all cases the Q_2-Q_4 site with an energy barrier of 105 kJ mol^{-1} as the limiting step. Yet the decay of the pre-exponential factor f_D with temperature results in a global activation energy of $\sim$ 95 kJ mol^{-1} which is fortuitously very close to the Q_1-Q_4 breakage.

Despite the simulations lie in the reported range of experimental dissolution rates, two aspects that could improve our results must be pointed out. First, the activation energy difference could be explained by the dissolution boost from a small fraction ($\sim 5-18\%$) of deprotonated surface sites due to pH with smaller energy barrier [45]. However, a lower activation energy would imply a higher dissolution rate. Hence, and opposed to the above, f_D value is expected to be smaller. The f_D value used in this work was calculated for a disiloxane-water cluster [24]. Such cluster does not have the surrounding oxygen atoms presented in a silica one. In the latter, the movement or vibrational modes of the transition state is expected to be more constrained and, therefore, the partition function should be smaller. This would result in a lower dissolution rate, approaching to the experimental ones.

5.4.3 Dissolution rate with ΔG

Predicting the dissolution rate dependence with Gibbs free energy is still a hot topic in mineral dissolution. The typical curve where the dissolution increases sharply from $\Delta G = 0$ to reach gradually the plateau predicted by the TST has been overshadowed by experimental curves following a sigmoid function (see section 1.2.1) [31,49,50]. In chapter 2, it has been shown that such sigmoidal shapes have a topographic origin, and some minerals like quartz may conserve the typical TST shape due to its specific atomic structure or even because of the E_D and E_P relation.

α-Quartz dissolution rate dependence with ΔG for our simulations is represented in figure 5.5b at a temperature of 473 K. The experimental values from Dove's work are included [20]. The experimental pH $= 5.7$ ensures very low deprotonation effect [45]. The Dove's curve follows a typical TST trend which reaches the plateau when the SiO_2 concentration is $C \simeq 16$ mM (the concentration in equilibrium is $C_e = 3.98$ mM [20]). Our simulations report a higher dissolution rate than the experiments, which strengthens the hypothesis of a f_D overestimation, although the shape of the curves follows similar TST behaviour. In our case the plateau is reached at a higher concentration, when $C \simeq 38$ mM. Discrepancies may arise, on the one hand, because some processes may happen due to higher scale fluctuation of the concentration. For example, at close to equilibrium conditions, quartz may precipitate into hillocks in the $\{001\}$ plane meanwhile the rest are dissolving [16]. On the other hand, because the expected null dissolution rate at $\Delta G = 0$ is not reproduced. This is due to our implicit consideration of the precipitation as a diminution of the net dissolution rate. Such approximation fails at very close to equilibrium conditions since the growth effect gains importance. A symmetric equation to describe growth would report, at $\Delta G = 0$, an opposed dissolution rate value, resulting in a net 0 rate. Therefore, closest points to $\Delta G = 0$ are expected to go sharply to 0, like the experimental ones.

Although one could think that the consideration of perfect surfaces instead of a real grain would change the global activation energy or dissolution rate due to a higher fraction of lower coordinated atoms, this is not the case. Dove *et al.* [20] reported no increase in the dissolution rate with increase in the surface roughness. Similarly, Blum *et al.* observed no increase in dissolution as the number of dislocations increases [46]. These two facts can be explained since the limiting Q_2-Q_4 site is always present, either at corners or at close to dislocation positions. The density of this site in the surface is constant at a steady state of dissolution if the grain size effect is neglected. The number of dislocations affect the quickness with which the steady state is reached [46]. Nevertheless, neither the number of dislocations nor the generated pit shape have any impact afterwards.

As proof of this scenario, we have studied the dissolution of the wulff shape of quartz, which is the geometry with minimum energy of a mineral. For quartz it is a prism with hexagonal section and

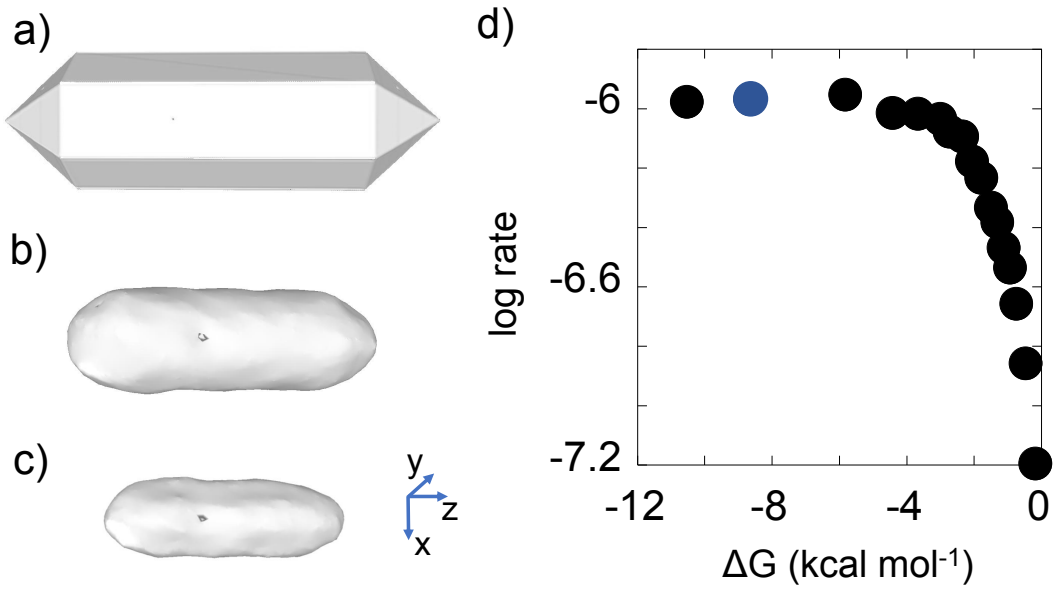

Figure 5.6: **Quartz wulff shape dissolution study with** ΔG. a) Initial state. b) Wulff shape after half of the forming atoms have dissolved. c) 25 % of the atoms remain. d) Dissolution rate versus ΔG curve. Blue point corresponds to the simulation of the topographies in a-c, though similar topographies are obtained in any other point. The visual representation is done using OVITO program.

pyramidal tips [163] (see figure 5.6a). As additional element, one dislocation is placed transversally in the center of the {100} plane, and another one perpendicular to the previous and longitudinally to the wulff shape. During dissolution, the initial wulff shape is distorted into an elongated grain which reduces its size until the complete extinction, with no effect of the dislocations. The surface area and the dissolution rate values are calculated at the time when the grain has lost half of its atoms (see figure 5.6b). The estimated surface area is $S_{1/2} = 3.3 \cdot 10^{-16}$ m^2. Results of dissolution rate with ΔG at 473 K in free dissolution is shown in figure 5.6d. As expected, it shows same results than for the three infinite plane cases in free dissolution (see figure 5.5b).

Finally, in figure 5.7 the limit case in which $q^{\ddagger}/q^{\mathrm{D}} = q^{\ddagger}/q^{\mathrm{P}}$ ($f_{\mathrm{P}} = f_{\mathrm{D}}$) for the free dissolution case in {100} plane is compared with the simulation results when $q^{\ddagger}/q^{\mathrm{D}} = 1$, showing no change. Such result is specific of α-quartz structure. Differences are expected in more complex minerals since the mechanism activation (dissolution of initial irregularities, dislocation opening and spontaneous pits opening) may be shifted to more negative ΔG values by increasing f_{P} (see equation 2.13).

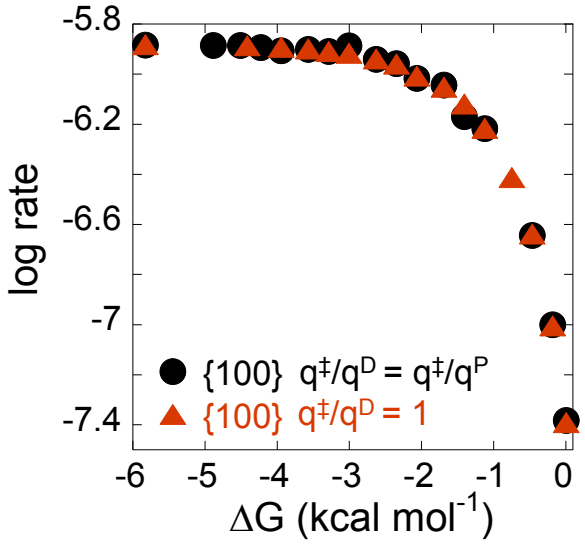

Figure 5.7: $f_{\mathbf{D}}$ **and** $f_{\mathbf{P}}$ **relation.** Comparison of simulations with $q^{\ddagger}/q^{\mathrm{D}} = q^{\ddagger}/q^{\mathrm{P}}$ and $q^{\ddagger}/q^{\mathrm{D}} = 1$ for the free dissolution case in $\{100\}$ plane.

5.5 Conclusions and outlook

In this chapter quartz dissolution has been studied by KMC simulations. A model where the Si-O-Si bond is hydrolyzed with variable energy barrier as a function of the Si connectivity is proposed to describe the dissolution. As a result, the obtained etch pit shapes during dissolution, dissolution rates, activation energies and dissolution rate dependence with ΔG are in agreement with the experiments. We found striations in the $\{001\}$ plane along the [110] direction, rectangular pyramidal pits in the $\{100\}$ plane with the longest sides along the [010] direction and trapezoidal semipyramidal pits with the two parallel sides along the [010] direction. A stabilization effect, which gives initial stability to atoms on the surface that are not close to a dislocation, is needed to correctly reproduce them. Secondly, the global activation energy, $E_{\mathrm{a}} = 94.7 \pm 1.9$ kJ mol^{-1} , is in agreement with experimental value, despite the dissolution rates are slightly higher. This suggests that vibrational modes calculated by DFT for the disiloxane-water cluster, despite they represents a reasonable first estimation, are not good enough and a more accurate calculation is needed in a proper silica cluster. Besides, since in the simulations the Q_2-Q_4 bond breakage with 105 kJ mol^{-1} has been recognized as the limiting step and yet the global activation energy is similar to a Q_1-Q_4 bond breakage (95 kJ mol^{-1}), there is no

need to invoke the existence of a self healing effect to explain such energy reduction [23]. Finally, experimental dissolution rate dependence with ΔG follows a typical TST curve whose trend has been reproduced with our simulations. Results support the model extension proposed in chapter 2, yet further investigations are needed.

Despite the good results, there is still room to the improvement. Computationally, DFT future works can be focused on obtaining better f_{D} and f_{P} values or filling in the blank spaces in energy barrier values, also for deprotonated and protonated sites. Explicit consideration of precipitation in KMC simulations would improve the points close to $\Delta G = 0$, and could also allow to study precipitation and growth. It would also be possible to repeat this study under catalytic conditions by setting a fraction of the sites with smaller energy barrier. Experimental work could be focused on measuring the dissolution rate dependence with temperature and ΔG in perfect planes without any deprotonation effect, that is, at low pH [45]. For that, there are new promising experimental methodologies like Digital holographic microscopy (DHM) which would be able to measure the local concentration of the mineral in water close to the surface (see section 1.3.2.4).

Chapter 6: The Dissolution of Alite

6.1 Introduction

Portland cement is the most used material by the mankind, just after water [40]. Its low cost in comparison with its relatively low environmental impact and performance, its workability and its worldwide availability make cement a major ingredient in almost any engineering work. In fact, the production of the huge volume of cement consumed accounts for 5–8% of man-made CO_2 emissions [50]. Among all the possible solutions, understanding the processes behind cement hydration would improve its performance and reduce its environmental impact.

In the hydration process, cement powder is mixed with water to create a moldable phase which hardens in a matter of hours. The calorimetric curve in figure 6.1 shows the typical evolution of released heat during cement hydration, which is proportional to the hydration rate. Briefly, alite ($Ca_3Si_2O_5$), or C_3S in cement chemistry notation (see appendix B), and other reactants in cement like belite (C_2S) and tricalcium aluminate (C_3A) react with water to form later a calcium silicate hydrate phase of variable composition, the C–S–H gel, and crystalline side products like portlandite (CH) (see equation 6.1).

$$Ca_3SiO_5 + 5.3\ H_2O \rightarrow Ca_{1.7}Si(OH)_4 + 1.3\ Ca(OH)_2 \tag{6.1}$$

The hydration process can be divided into 5 differentiated phases according to the evolution of the calorimetry (see figure 6.1). Some of the knowledge behind each phase is as follows:

1) The dissolution phase. The quick dissolution of C_3S releases $Si(OH)_4$ and $Ca(OH)_2$ ions to solution. The concentration of $Si(OH)_4$ reaches a maximum value and begins to reduce as the first C-S-H gel is formed. C_3A reacts very fast with water, even faster than alite. Nevertheless, this process, known as flash setting, is not desired since it reduces the workability of cement at

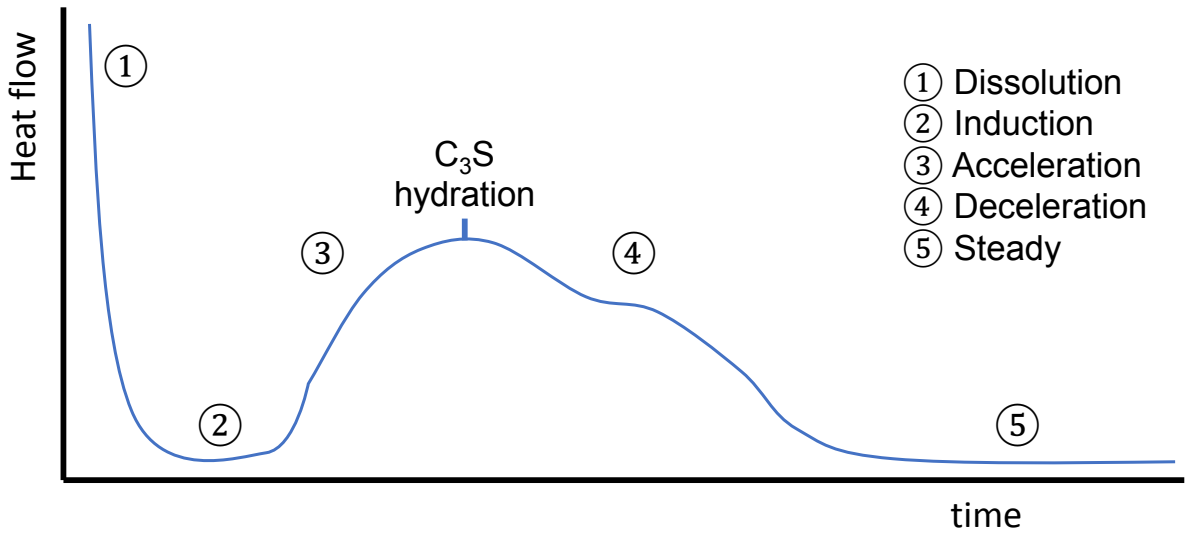

Figure 6.1: **Cement hydration curve**. Schematic representation of heat evolution versus the hydration time of ordinary Portland cement pastes.

early ages of the hydration process. To avoid the flash-setting, retardants such as gypsum are added to the clinker [40].

2) The induction period or dormant phase. The reaction rate is low. During this period, the water-cement mix remains moldeable and provides cement its important workability feature; the named open window.

3) The acceleration phase. Portlandite starts to precipitate and C-S-H gel is produced forming a colloidal three dimensional structure, which confers cement its strength [164].

4) Deceleration phase. After several hours, portlandite and C-S-H formation rate slowly decreases.

5) Steady phase. In this stage the microstructure of C-S-H gel becomes denser. It is considered that the hydration is virtually finished after one year, though the process could continue over years, as well as the evolution of C-S-H gel and cement paste microstructure [165]

Over the years, many theories have been proposed to explain the calorimetry curve of cement hydration and particularly the origin of the dormant period [50]. All of them identify the released heat with dissolution reactions of reactants like C_3S and C_3A or with precipitation reactions like portlandite

or C-S-H formation. The possible explanations of the dormant period that involve a reduction of the dissolution rate are: the existence of protective [166–172] and semi-permeable [173,174] membranes that inhibit the dissolution rate, a change of the local or superficial concentration in the Stern layer [175,176], or a direct phenomenon related with the dislocations [177–180]. On the other hand, other explanation includes a reduction of portlandite precipitation because of the poisoning effect of silicates [176,181], and another one relies the heat flow on the C–S–H growth, which is delayed by the dissolution of products [50,93,164,180,182–184].

Based on mineral dissolution theory, the recent work by Nicoleau *et al.* [114,185] described briefly in section 1.4.5.3 has considered alite dissolution as the main responsible of the four last phases (2-5) in the calorimetry curve, with no apparent contribution from portlandite precipitation, C-S-H growth, or the change of the local concentration. After the initial peak, the origin of the induction period would correspond to a small contribution of the dislocation opening effect, produced even at close to equilibrium conditions [21,34]. The acceleration stage would be produced by to the gradual dislocation opening, increasing alite dissolution rate and thus the released heat. Finally, the dissolution of alite would decrease in the deceleration phase due to the dislocation coalescence and grain extinction.

We cannot overlook the existence of an alternative and very important current of thought about the origin of the dissolution rate evolution of C_3S. Many researchers have proposed that the dissolution is controlled by the nucleation and growth of C-S-H, and to a less extent, Portlandite. A very schematic explanation will be as follows: initially, the C-S-H gel nucleates mainly on favorable spots on the clinker surfaces, nucleation seeds, or spontaneously in solution. The C-S-H grows in 3D since there is a continuous increase of its formation rate until coalescence with the C-S-H growing from other sites. At that point, the C-S-H growth rate starts to decrease due to the lack of free space. The nucleation and growth of C-S-H is directly related to the ion concentration in the pore solution, and the undersaturation state varies accordingly. Therefore, the more C-S-H is produced, the further from equilibrium conditions, enhancing the alite dissolution. Many models have been developed following this theory, mainly based on the Avrami model of heterogenous nucleation [186] and the Boundary

nucleation and growth (BNG) of homogeneous nucleation [187], with different modifications and extensions to take into account factors like confinement, pore solution chemistry, presence of seeds, C-S-H morphology and densification, etc [93, 125, 164, 188–197].

In this chapter we will focus on the interpretation given by the mineral dissolution theory, without considering the precipitation and growth of C-S-H. We will take mineral dissolution as the starting point for a 'computational experiment' to investigate what would be the underlaying mechanism that could explain the acceleration and deceleration of the alite dissolution rate. The results do not imply that the mineral dissolution theory is correct and the nucleation and growth is not. It is plausible that both theories are necessary to explain the hydration of alite. In fact, some authors suggest that mineral dissolution is the main responsible of the acceleration period while C-S-H growth will be the limiting mechanism for the deceleration [198].

6.2 Methods and Alite Dissolution Model

There is plenty of experimental information about alite dissolution in the bibliography [12, 21, 34, 50, 185]. Nevertheless, *ab initio* studies about the processes at atomic scale happening behind are still subject of study [43]. Due to the lack of information of alite dissolution and precipitation energy barriers, we choose to perform a general study within the framework of a Kossel crystal (see section 1.4.4). The dimension of the Kossel crystal under study are 200 x 200 x 80 sites for a total of $\sim$ 3200000, with periodic boundary conditions. Considering each site as a C_3S unit, the distance between them is $\sim$ 4.9 Å [199], which leads to a system size of $\sim$ 100 x 100 x 40 nm. One dislocation is placed in the center of the *xy* plane, which results in a dislocation density of 10^{12} m^{-2} and lies into the known dislocation density range for minerals $10^{10} - 10^{14}$ m^{-2} [62]. The dissolution of the {001} plane is studied, though results in {100} and {010} would be identical in a Kossel crystal.

The same model presented in chapter 2 is used here as implemented in KIMERA program. The dissolution and precipitation events probability are given by equations 2.1 and 2.2:

$$r'_{\mathrm{D}} = f_{\mathrm{D}} \cdot \exp\left(-\frac{E_{\mathrm{D}}}{k_{\mathrm{B}} \cdot T}\right) \tag{6.2}$$

$$r'_{\mathrm{P}} = f_{\mathrm{P}} \cdot \exp\left(-\frac{E_{\mathrm{P}} - \Delta G^{*}}{k_{\mathrm{B}} \cdot T}\right) \tag{6.3}$$

The first step is to determine the dissolution and precipitation energy barriers and their respective pre-exponential factors f_{D} and f_{P}. As we lack these parameters, we do a guess of them based on the experimental results and observations in the bibliography. First, we know that the experimental activation energy is about 49-51 kJ mol^{-1} [21, 200]. Secondly, it is observed a diminution of the activation energy when alite grains reduce their size from about 51 to 44 kJ mol^{-1} [200]. As we know that the activation energy is related to the dissolution energy barrier E_{D} (see section 2.4.4), the diminution can be explained by an increase of the fraction of atoms in kink sites respect to the atoms in perfect planes when the grain size is reduced. Therefore, we can directly relate these activation energies to the E_{D} of a kink position and to the E_{D} of an atom close to a dislocation position, with coordination 3 and 4 respectively (see figure 1.11 and table 6.1). The E_{D} for the rest of the positions are supposed to follow a linear trend with these two values. Thirdly, since the vibrational frequencies of alite atoms are not highly constrained like in quartz (see sections 1.4.1 and 5.2), a value of $f_{\mathrm{D}} \sim 10^{13}$ s^{-1} at 300 K is expected [6]. Nevertheless alite dissolution rate experiments report about $1-2$ order of magnitude of the Arrhenius pre-exponential factor A' higher than quartz (see equation 1.10 and figure 1.9), which suggest that f_{D} is below the $4.7 \cdot 10^{10}$ s^{-1} considered at 300 K for quartz in the previous chapter (see table 5.2 and equation 5.3). Such discrepancy may be explained by the passivation produced in the alite surface at its initial stages of hydration [201]. The fraction of reaction sites on the alite surface could be much lower due to a thin layer of hydration products blocks the way to water molecules to react. Therefore the activity coefficient of alite hydration reaction could be $\gamma << 1$ (see section 1.2.1 and equation 1.25). A value around $f_{\mathrm{D}} \sim 10^{8} - 10^{9}$ s^{-1} is considered, though its exact determination will be done *ad-hoc* to better reproduce the experimental data. Final step is to determine the E_{P} and f_{P} values. We have considered $f_{\mathrm{P}} = f_{\mathrm{D}}$, and have selected

f_D (s^{-1})	f_P (s^{-1})	E_D (kJ mol^{-1})	E_P (kJ mol^{-1})	First neightbours
$1.8 \cdot 10^9$	$1.8 \cdot 10^9$	33	33	1
		38	28.75	2
		44	25.75	3
		50	22.5	4
		55	18.25	5
		-	-	6

Table 6.1: **Alite dissolution model parameters**. Proposed model parameters for alite dissolution. Bulk atoms with 6 first neighbours do not react.

E_P values according to the best fitting of the dissolution rate with ΔG curve to experiments. Note that other combinations of values with the same experimental fitting would reproduce same experimental phenomenology and distribution of dissolution mechanisms. In table 6.1 the model parameters to reproduce alite dissolution rate and its activation energy are shown. Appendix A.4 contains the necessary input file to perform the simulation in KIMERA program.

6.3 Results

6.3.1 Dissolution rate and activation energy with ΔG

Simulations using the parameters in table 6.1 are fitted to the experimental results in [21]. This experimental dataset is obtained from vertical scanning interferometry (VSI) experiments on the surface of alite (see section 1.3.2.2), as they compare better to simulations in a infinite plane than experiments in powder samples. Results are shown in figure 6.2. The dissolution rate with ΔG follows a sigmoid function equal to experiments. The simulations shows hardly any dissolution rate at close to equilibrium conditions, where a perfect plane topography is obtained, typical of mechanism I. Once we are far enough from equilibrium at ΔG_{crit}, the dislocation starts to open, producing typical patterns of mechanism II and increasing the dissolution rate (see section 1.2.1). When the dissolution plateau is reached, plenty of spontaneous pit opening is produced on the surface, leading to a pattern governed by mechanism III. The empirical fitting proposed in equation 2.18 reports a critical $\Delta G_{crit} = -11$

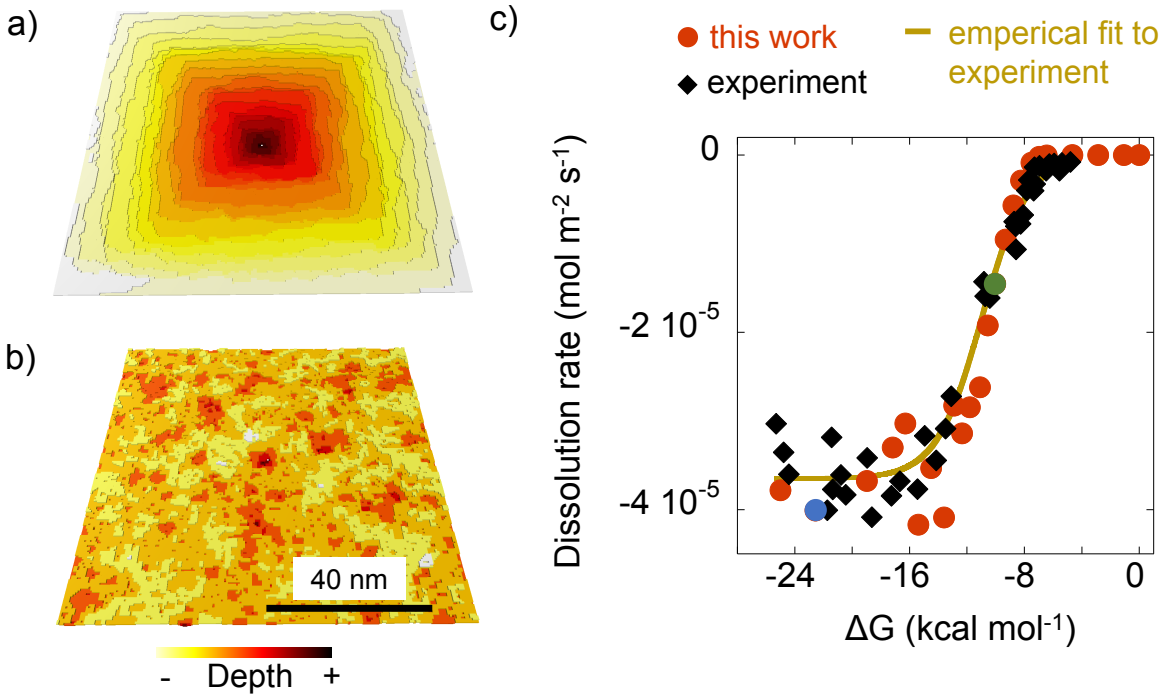

Figure 6.2: **Alite dissolution rate with** ΔG. a) Dissolution pattern during the dissolution close to ΔG_{crit} showing pit opening (mechanism II). The simulation corresponds to the green point. b) Dissolution pattern at far from equilibrium conditions showing spontaneous pit opening (mechanism III). The simulation corresponds to the blue point c) Dissolution rate versus ΔG fitted for the experiment in [21].

kcal mol^{-1}.

As we saw in section 2.4.4, the activation energy for a Kossel crystal depends on the dissolution mechanism. If there is no change of f_{D} with temperature, the activation energy for mechanism I is given by the E_{D} of an atom of a kink site $E_{\text{a m.I}} = 44$ kJ mol^{-1}, the activation energy for mechanism II is given by the E_{D} of an atom close to a dislocation $E_{\text{a m.II}} = 50$ kJ mol^{-1}, and similarly for mechanism III, but with a slight influence of the E_{D} of an atom in a perfect surface, thus $E_{\text{a m.III}} \sim 51$ kJ mol^{-1}. The transition between mechanisms is gradual, so values between $44 - 51$ kJ mol^{-1} are expected along all the ΔG curve. In order to check this behaviour, in figure 6.3 we plot the natural logarithm of the dissolution rate versus $1/T$ at far for equilibrium conditions and at ΔG_{crit} region for five temperatures: 300, 350, 400, 450 and 600 K. In table 6.2 the activation energy results are shown. As observed, they are the excepted ones. Moreover, the A' values obtained in the lineal fitting

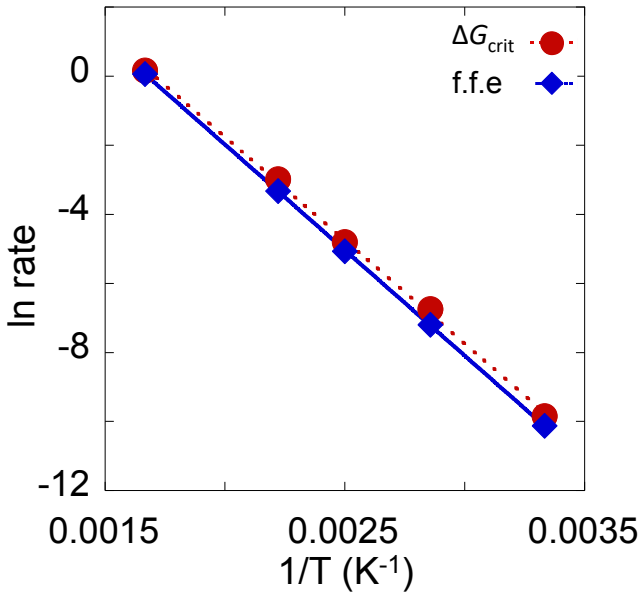

Figure 6.3: **Alite activation energy**. Natural logarithm of the dissolution rate versus the inverse of temperature at far from equilibrium conditions (f.f.e) and ΔG_{crit} values.

	E_a (kJ mol^{-1})	A' (mol m^{-2} s^{-1})
ΔG_{crit}	49.8 ± 0.9	$(27 \pm 8) \cdot 10^3$
f.f.e	50.8 ± 0.2	$(28.1 \pm 1.5) \cdot 10^3$

Table 6.2: **Activation energy and pre-exponential factor**. Reported values in figure 6.3 at far from equilibrium conditions (f.f.e) and ΔG_{crit} values.

is consistent with the experiments since $\log A' = 4.3 - 4.5$, as observed in figure 1.9.

Experiments report an unsuspected low activation energy of $13 - 26$ kJ mol^{-1} at far from equilibrium conditions, in the dissolution plateau [21]. Juilland *et al.* demonstrated that such low values in the activation energy are obtained due to the diffusion is the limiting step of the dissolution process and hence there is a change of limiting step when dissolution rate increases due to ΔG (see section 1.2.2). In equation 1.9 we have shown that a higher diffusive layer produces a decrease in the dissolution rate. Therefore, the 'real' dissolution rate by considering no diffusion effect is expected to be higher in the dissolution plateau and thus our model values in table 6.1 slightly different. Experimental determination of alite dissolution rate with digital holographic microscopic (DHM)

(see section 1.3.2.4) or rotating disk techniques (see section 1.3.1.2), where the diffusion effect is controlled, would help to adjust them.

6.3.2 Impact of the pits coalescence on the dissolution rate

Nicoleau *et al.* [12,114,185] have proposed that during cement hydration alite dissolves in conditions close to equilibrium, because ion diffusion within cement matrix is not high enough to displace the ions from close to surface positions [114]. Moreover, the conditions remain almost constant since the diffusivity is not reduced by the formation of hydration products. Therefore, it is expected that alite dissolves in cement matrix close to the ΔG_{crit} region, showing mechanism II with preferable dissolution of the dislocations (see figure 6.2a). Besides, Nicoleau *et al.* have proposed alite dissolution rate as the only responsible for the calorimetric curve shape of Portland cement hydration. After the acceleration phase due to an increase of the dissolution rate of alite grains, the deceleration phase is produced because of their gradual extinction along with the coalescence of the pits in their surfaces. The former explanation is intuitive; the smaller the grain the smaller the surface able to react. However, our study indicates that the coalescence of pits does not produce a decrease of the dissolution rate, as demonstrated below.

In the black curve of figure 6.4, we have represented the time evolution of the dissolution rate of our simulation highlighted with a green point at ΔG_{crit} in figure 6.2c. The dissolution rate is directly related to the calorimetric curve [185]. As it can be seen, the dissolution rate increases gradually until short beyond the coalescence region due to the initial inertia, which later stabilizes in a constant value. Therefore, coalescence is not suitable as an explanation for the deceleration phase of cement calorimetric curve. In order to check this statement with finer focus, figure 6.5 represents the time evolution of the coordination of the surface sites, which it is directly related to the dissolution rate. At the beginning of the simulation, all the sites on the surface except from the ones close to a dislocation have coordination 5, as expected in a perfect plane. The number of sites in this position decreases when the dislocation starts to open, increasing the number of sites with coordination 3 and 4. When the dislocation coalesces, the number of sites with each coordination stabilises and remains constant.

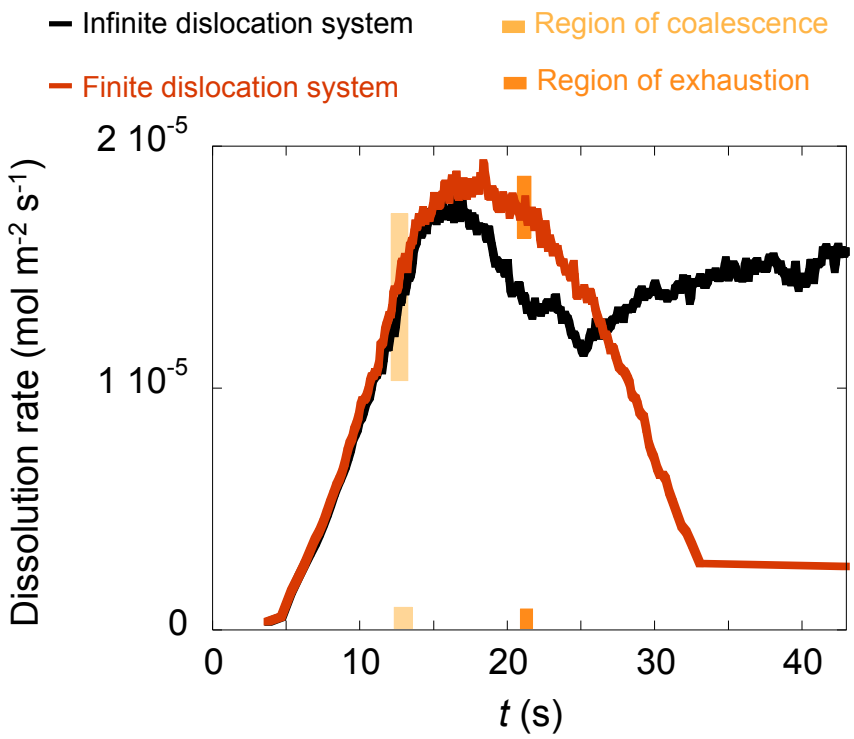

Figure 6.4: **Dislocation coalescence and exhaustion in alite**. Time evolution of the dissolution rate. Black curve shows the evolution of a system with a infinite dislocation, corresponding to the green point in figure 6.2c. Red curve corresponds to a system with a finite dislocation with a depth equal to half of the system's thickness. Both simulations in the coalescence region shows the same topography observed in figure 6.2a.

Moreover, the sum of surface sites with all the different coordinations, which is related to the surface area, keeps almost constant during all the dissolution process. Since the number of reactive sites and the surface area do not change in the coalesce region, a dissolution rate diminution due to coalescence is not possible. Note that this result is not unique for alite dissolution in this ΔG conditions but it is extensible to any pit coalescence.

Another effect that may reduce the dissolution rate is the named dislocation exhaustion [202]. As dislocations are the preferable spot for dissolution, dislocation density decreases with time. We can represent the dislocation exhaustion by considering that the dislocation placed in the middle of our system has a depth equal to half of the system's thickness. We do the same simulation with same ΔG_{crit} value and compare it to the previous black curve in figure 6.4. Initial stages are similar since the system is initially identical to the one considered before. Once the exhaustion region is

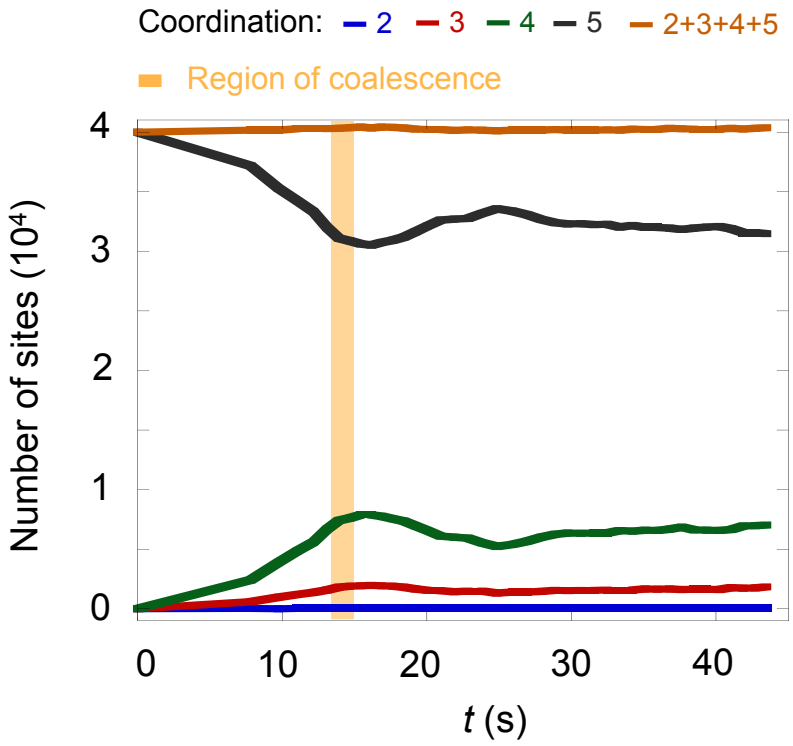

Figure 6.5: **Surface coordination**. Time evolution of the coordination of the surface sites for the black curve in figure 6.4. Coordination stabilises close to the coalescence region values. The number of 1 coordinated sites are overlapped by the number of 2 coordinated sites. In both cases they are constantly close to 0. Orange line represents the total number of sites forming the surface.

reached, its dissolution rate decreases, as long as the steps created by the dislocation disappear (see figure 6.2a), leading to a very flat surface. The dissolution rate is then determined by the pace of the spontaneous pit opening, which at ΔG_{crit} is very slow; the lower the closer to the equilibrium. Observing these results, we can suggest that dislocation exhaustion may be the another possible explanation for the deceleration phase.

6.4 Conclusions and outlook

In this chapter alite dissolution has been studied using a Kossel crystal structure and the kinetic model proposed in this thesis. In a first step, the model parameters have been fitted to the experimental results and observations. As a result, the experimental activation energy $E_{\text{a}} = 44 - 51$ kJ mol^{-1} and the pre-exponential Arrhenius factor $A' = 27 \pm 8 \cdot 10^3$ mol m^{-2} s^{-1} have been successfully reproduced, along with the experimental sigmoid function of the dissolution rate with ΔG.

In a second step, the variation with the coalescence and exhaustion of the dislocations has been studied. It has been demonstrated that the coalescence does not imply a reduction of the dissolution rate and thus it is not involved in the deceleration phase of cement hydration as proposed in the bibliography. Nevertheless, the dislocation exhaustion involves an extra explanation to such dissolution rate reduction.

The future experimental research may explore the validity of the dislocation exhaustion phenomenon. On the other hand, though both the Kossel crystal and the kinetic model have demonstrated to be useful to describe alite dissolution, *ab initio* simulations may focus on getting the necessary parameters to describe alite hydration reaction with higher accuracy in the proper alite atomic structure.

Abstract

Mineral dissolution is a fundamental process in geochemistry and materials science. Numerous experimental and computational works have aimed to understand the dissolution processes and the mechanisms at atomic level to improve industrial applications and harness the nature processes. A considerable number of models have been proposed to describe the factors influencing the mineral dissolution rate, like temperature, pH, Gibbs free energy difference between the solid and the solution, ionic diffusion or system topography and size, providing a great set of tools to foresee behaviours and phenomena. Nevertheless, one of those factors, the mineral dissolution rate with Gibbs free energy (ΔG) was in the spotlight because an unexpected sigmoidal function was observed in the experiments. In this thesis, we have extended the kinetic model, that is one of the most recent and complete models in the bibliography, and improve the Kinetic Monte Carlo (KMC) method, which suppose its perfect complement due to its ability to bring the results to scales comparable to experiments, to demonstrate that such sigmoid function was the result of the subtle interplay between dissolution and precipitation reactions in the mineral surface. This important result has been checked in a Kossel crystal, a generic system to represent the topography of any mineral. It has served as a starting point to study the ΔG dependence within the specific atomic structure of any other mineral. Other side results are the dissolution rate dependence with the dislocation density or the surface roughness, the demonstration of the impossibility for minerals with simpler structure than a Kossel crystal to recreate such sigmoid function, or the prediction of the possible existence of unreported dissolution mechanisms.

In a second part of the thesis in chapter 3, we have developed an efficient and complete KMC computational program named KIMERA. If the possible elemental reactions in the mineral surface and their respective model values are well known, which are available from atomistic simulations, KIMERA is able to simulate the dissolution of any mineral at atomic scale at any condition of temperature, pH or ΔG, obtaining parameters and mineral topographies comparable to experiments. We have checked this powerful tool and the proposed dissolution model by studying the dissolution

of quartz; one of the most studied minerals of the bibliography. We have reproduced perfectly its mineral topography and dissolution rate dependence with temperature. Besides, we have confirmed the experimentally reported invariability of the dissolution rate with quartz dislocation density or grain morphology. In the dissolution rate dependence with ΔG, although more accurate results are possible through finer model parameters, our simulations report the same function shape than in experiments.

We have also used KIMERA program to elaborate a study of several configurations of a Kossel crystal with two types of particles and different set of model values. Apart from recognising the unfeasibility of some of the them, with this systematic study we have elaborated a map of the possible topographies and phenomena, allowing to foresee results of future studies with other model values or even configurations.

Finally, we have done a study of the dissolution of alite, one of the main components of Portland cement and whose dissolution is the main responsible of its properties. After recognising parameters of our model from experimental observations, we have proved wrong the assumption taken in the bibliography that the dislocation coalescence reduces the mineral dissolution rate. Moreover, we have proposed dislocation exhaustion as a plausible explanation to the deceleration phase in the cement hydration process; although it requires experimental validation.

Atomistic simulations along with the KMC method have proved in this thesis to be a powerful tool to study mineral dissolution and explain experimental results. The development of our model and the publication of KIMERA represent two great advances and ensure us and other scientists continuity on improving the knowledge in the field of mineral dissolution. Future work will focus, firstly, on continuing the study of the dissolution of other minerals; Secondly, on extending the model with another important factor in the dissolution rate, the effect of diffusivity; and finally, on improving KIMERA to study precipitation.

Bibliography

[1] James L Palandri and Yousif K Kharaka. A compilation of rate parameters of water-mineral interaction kinetics for application to geochemical modeling. Technical report, Geological Survey Menlo Park CA, 2004.

[2] Jean Colombani. Measurement of the pure dissolution rate constant of a mineral in water. *Geochimica et Cosmochimica Acta*, 72(23):5634–5640, 2008.

[3] Susan Louise Brantley, James David Kubicki, and Art F White. *Kinetics of water-rock interaction*, volume 168. Springer, 2008.

[4] DR Boomer, CC McCune, and HS Fogler. Rotating disk apparatus for reaction rate studies in corrosive liquid environments. *Review of Scientific Instruments*, 43(2):225–229, 1972.

[5] John Kaszuba, Bruce Yardley, and Muriel Andreani. Experimental perspectives of mineral dissolution and precipitation due to carbon dioxide-water-rock interactions. *Reviews in Mineralogy and Geochemistry*, 77(1):153–188, 2013.

[6] Antonio C Lasaga. *Kinetic theory in the earth sciences*. Princeton university press, 2014.

[7] Antonio C Lasaga and Alex E Blum. Surface chemistry, etch pits and mineral-water reactions. *Geochimica et Cosmochimica Acta*, 50(10):2363–2379, 1986.

[8] Alexander Stukowski. Visualization and analysis of atomistic simulation data with ovito–the open visualization tool. *Modelling and Simulation in Materials Science and Engineering*, 18(1):015012, 2010.

[9] T.E. Burch, K.L. Nagy, and A.C. Lasaga. Free energy dependence of albite dissolution kinetics at 80^{o}c and ph 8.8. *Chemical Geology*, 105(1):137 – 162, 1993.

[10] A. C. Lasaga and A. Lüttge. Variation of crystal dissolution rate based on a dissolution stepwave model. *Science*, 291(1998):2400–2404, 2001.

[11] Jordi Cama, Jiwchar Ganor, Carles Ayora, and C Antonio Lasaga. Smectite dissolution kinetics at 80 c and ph 8.8. *Geochimica et Cosmochimica Acta*, 64(15):2701–2717, 2000.

[12] L Nicoleau, A Nonat, and D Perrey. Cement and Concrete Research The di- and tricalcium silicate dissolutions. *Cement and Concrete Research*, 47:14–30, 2013.

[13] Aaron S Taylor, Joel D Blum, and Antonio C Lasaga. The dependence of labradorite dissolution and sr isotope release rates on solution saturation state. *Geochimica et Cosmochimica Acta*, 64(14):2389–2400, 2000.

[14] Jean-Marie Gautier, Eric H Oelkers, and Jacques Schott. Experimental study of k-feldspar dissolution rates as a function of chemical affinity at 150 c and ph 9. *Geochimica et Cosmochimica Acta*, 58(21):4549–4560, 1994.

[15] Koichi Momma and Fujio Izumi. Vesta: a three-dimensional visualization system for electronic and structural analysis. *Journal of Applied Crystallography*, 41(3):653–658, 2008.

[16] Inna Kurganskaya and Andreas Lüttge. Kinetic Monte Carlo Simulations of Silicate Dissolution: Model Complexity and Parametrization. *The Journal of Physical Chemistry C*, 117(47):24894–24906, nov 2013.

[17] Andrew J Gratz, Peter Bird, and Glenn B Quiro. Dissolution of quartz in aqueous basic solution, 106–236 c: Surface kinetics of "perfect" crystallographic faces. *Geochimica et Cosmochimica Acta*, 54(11):2911–2922, 1990.

[18] AR Patel, OP Bahl, and AS Vagh. Etching of rhombohedral cleavages of quartz. *Acta Crystallographica*, 19(5):757–758, 1965.

[19] Jefferson W Tester, W Gabriel Worley, Bruce A Robinson, Charles O Grigsby, and Jeffrey L Feerer. Correlating quartz dissolution kinetics in pure water from 25 to 625 c. *Geochimica et Cosmochimica Acta*, 58(11):2407–2420, 1994.

[20] Patricia M Dove, Nizhou Han, and James J De Yoreo. Mechanisms of classical crystal growth theory explain quartz and silicate dissolution behavior. *Proceedings of the National Academy of Sciences*, 102(43):15357–15362, 2005.

[21] P. Juilland and E. Gallucci. Morpho-topological investigation of the mechanisms and kinetic regimes of alite dissolution. *Cement and Concrete Research*, 76:180–191, 2015.

[22] Alexander Pelmenschikov, Helene Strandh, Lars GM Pettersson, and Jerzy Leszczynski. Lattice resistance to hydrolysis of si- o- si bonds of silicate minerals: ab initio calculations of a single water attack onto the (001) and (111) β-cristobalite surfaces. *The Journal of Physical Chemistry B*, 104(24):5779–5783, 2000.

[23] Alexander Pelmenschikov, Jerzy Leszczynski, and Lars GM Pettersson. Mechanism of dissolution of neutral silica surfaces: Including effect of self-healing. *The Journal of Physical Chemistry A*, 105(41):9528–9532, 2001.

[24] Wlliam H Casey, Antonio C Lasaga, and GV Gibbs. Mechanisms of silica dissolution as inferred from the kinetic isotope effect. *Geochimica et Cosmochimica Acta*, 54(12):3369–3378, 1990.

[25] Hans-Rudolf Wenk and Andrey Bulakh. *Minerals: their constitution and origin*. Cambridge University Press, 2016.

[26] Charles W Chesterman and K Lowe. Field guide to north american rocks and minerals. *The Audubon Society. New York, New York. Alfred A Knopf*, 1978.

[27] Jacobus Henricus van't Hoff. *Studies in chemical dynamics*. Chemical publishing Company, 1896.

[28] Michael F Hochella and Art F White. *Mineral-water interface geochemistry*, volume 23. Walter de Gruyter GmbH & Co KG, 2018.

[29] Nico Van Breemen and Peter Buurman. *Soil formation*. Springer Science & Business Media, 2002.

[30] Karsten Kalbitz, Stephen Solinger, J-H Park, Beate Michalzik, and Egbert Matzner. Controls on the dynamics of dissolved organic matter in soils: a review. *Soil science*, 165(4):277–304, 2000.

[31] Susan Louise Brantley. Reaction kinetics of primary rock-forming minerals under ambient conditions. *Treatise on geochemistry*, 5:605, 2003.

[32] Christin P Morrow, Shikha Nangia, and Barbara J Garrison. Ab initio investigation of dissolution mechanisms in aluminosilicate minerals. *The Journal of Physical Chemistry A*, 113(7):1343–1352, 2009.

[33] Jordi Cama and Jiwchar Ganor. Dissolution kinetics of clay minerals. In *Developments in Clay Science*, volume 6, pages 101–153. Elsevier, 2015.

[34] Patrick Juilland, Luc Nicoleau, Rolf S Arvidson, and Emmanuel Gallucci. Advances in dissolution understanding and their implications for cement hydration. *RILEM Technical Letters*, 2:90–98, 2017.

[35] H Roy Krouse, Christian A Viau, Leslie S Eliuk, Akira Ueda, and Stan Halas. Chemical and isotopic evidence of thermochemical sulphate reduction by light hydrocarbon gases in deep carbonate reservoirs. *Nature*, 333(6172):415, 1988.

[36] Martin Canals and Jean Dominique Meunier. A model for porosity reduction in quartzite reservoirs by quartz cementation. *Geochimica et Cosmochimica Acta*, 59(4):699–709, 1995.

[37] Roberto Garay Martinez, Eunate Goiti, Gudrun Reichenauer, Shanyu Zhao, Matthias Koebel, and Aitor Barrio. Thermal assessment of ambient pressure dried silica aerogel composite boards at laboratory and field scale. *Energy and Buildings*, 128:111–118, 2016.

[38] Alexander S Brand, Justin M Gorham, and Jeffrey W Bullard. Dissolution rate spectra of β-dicalcium silicate in water of varying activity. *Cement and Concrete Research*, 118:69–83, 2019.

[39] Andrew G Stack, Paolo Raiteri, and Julian D Gale. Accurate rates of the complex mechanisms for growth and dissolution of minerals using a combination of rare-event theories. *Journal of the American Chemical Society*, 134(1):11–14, 2012.

[40] Hegoi Manzano Moro. *Atomistic simulation studies of the cement paste components*. Servicio Editorial de la Universidad del País Vasco/Euskal Herriko ..., 2009.

[41] H Manzano, AN Enyashin, JS Dolado, A Ayuela, J Frenzel, and G Seifert. Do cement nanotubes exist? *Advanced Materials*, 24(24):3239–3245, 2012.

[42] Hegoi Manzano, Leire Gartzia-Rivero, Jorge Bañuelos, and iñigo López-Arbeloa. Ultraviolet–visible dual absorption by single bodipy dye confined in ltl zeolite nanochannels. *The Journal of Physical Chemistry C*, 117(25):13331–13336, 2013.

[43] Hegoi Manzano, Engin Durgun, I'nigo López-Arbeloa, and Jeffrey C Grossman. Insight on tricalcium silicate hydration and dissolution mechanism from molecular simulations. *ACS applied materials & interfaces*, 7(27):14726–14733, 2015.

[44] Shikha Nangia and Barbara J Garrison. Role of intrasurface hydrogen bonding on silica dissolution. *The Journal of Physical Chemistry C*, 114(5):2267–2272, 2010.

[45] Shikha Nangia and Barbara J Garrison. Reaction rates and dissolution mechanisms of quartz as a function of ph. *The Journal of Physical Chemistry A*, 112(10):2027–2033, 2008.

[46] Alex E Blum, Richard A Yund, and Antonio C Lasaga. The effect of dislocation density on the dissolution rate of quartz. *Geochimica et Cosmochimica Acta*, 54(2):283–297, 1990.

[47] Andreas Lüttge and Pamela G Conrad. Direct observation of microbial inhibition of calcite dissolution. *Appl. Environ. Microbiol.*, 70(3):1627–1632, 2004.

[48] Turpault Marie-Pierre, Nys Claude, and Calvaruso Christophe. Rhizosphere impact on the dissolution of test minerals in a forest ecosystem. *Geoderma*, 153(1-2):147–154, 2009.

[49] Andreas Lüttge. Crystal dissolution kinetics and gibbs free energy. *Journal of Electron Spectroscopy and Related Phenomena*, 150(2):248–259, 2006.

[50] Patrick Juilland, Emmanuel Gallucci, Robert Flatt, and Karen Scrivener. Dissolution theory applied to the induction period in alite hydration. *Cement and Concrete Research*, 40(6):831–844, jun 2010.

[51] Rolf S Arvidson and Andreas Lüttge. Mineral dissolution kinetics as a function of distance from equilibrium–new experimental results. *Chemical Geology*, 269(1-2):79–88, 2010.

[52] Cornelius Fischer, Inna Kurganskaya, and Andreas Lüttge. Inherited control of crystal surface reactivity. *Applied geochemistry*, 91:140–148, 2018.

[53] W-K_ Burton, N Cabrera, and FC Frank. The growth of crystals and the equilibrium structure of their surfaces. *Philosophical Transactions of the Royal Society of London. Series A, Mathematical and Physical Sciences*, 243(866):299–358, 1951.

[54] N Cabrera and MM Levine. Xlv. on the dislocation theory of evaporation of crystals. *Philosophical Magazine*, 1(5):450–458, 1956.

[55] William H Casey, Martin J Carr, and Robert A Graham. Crystal defects and the dissolution kinetics of rutile. *Geochimica et Cosmochimica Acta*, 52(6):1545–1556, 1988.

[56] Andreas Lüttge, Rolf S Arvidson, and Cornelius Fischer. A stochastic treatment of crystal dissolution kinetics. *Elements*, 9(3):183–188, 2013.

[57] William H Casey. Heterogeneous kinetics and diffusion boundary layers: The example of reaction in a fracture. *Journal of Geophysical Research: Solid Earth*, 92(B8):8007–8013, 1987.

[58] Fabien Jousse, Thibauld Jongen, and Wim Agterof. A method to dynamically estimate the diffusion boundary layer from local velocity conditions in laminar flows. *International journal of heat and mass transfer*, 48(8):1563–1571, 2005.

[59] Patricia M Dove and David A Crerar. Kinetics of quartz dissolution in electrolyte solutions using a hydrothermal mixed flow reactor. *Geochimica et cosmochimica acta*, 54(4):955–969, 1990.

[60] Keith J Laidler. The development of the arrhenius equation. *Journal of Chemical Education*, 61(6):494, 1984.

[61] Laura Briese, Rolf S Arvidson, and Andreas Lüttge. The effect of crystal size variation on the rate of dissolution–a kinetic monte carlo study. *Geochimica et Cosmochimica Acta*, 212:167–175, 2017.

[62] H.Henry Teng. Controls by saturation state on etch pit formation during calcite dissolution. *Geochimica et Cosmochimica Acta*, 68(2):253–262, 2004.

[63] William M Murphy. Dislocations and feldspar dissolution: Theory and experimental data. *Chemical Geology*, 70:163, 1988.

[64] GR Holdren, WH Casey, HR Westrich, M Carr, and M Boslough. Bulk dislocation densities and dissolution rates in a calcic plagioclase. *Chemical Geology*, 70(1-2):79, 1988.

[65] Jacques Schott, Susan Brantley, David Crerar, Christophe Guy, Maria Borcsik, and Christian Willaime. Dissolution kinetics of strained calcite. *Geochimica et Cosmochimica Acta*, 53(2):373–382, 1989.

[66] Susan L Brantley, Stephanie R Crane, David A Crerar, Roland Hellmann, and Robert Stallard. Dissolution at dislocation etch pits in quartz. *Geochim. Cosmochim. Acta*, 50(10):2349–2361, 1986.

[67] Heinz A Lowenstam. Minerals formed by organisms. *Science*, 211(4487):1126–1131, 1981.

[68] Fabio Nudelman and Nico AJM Sommerdijk. Biomineralization as an inspiration for materials chemistry. *Angewandte Chemie International Edition*, 51(27):6582–6596, 2012.

[69] Nouamane Laanait, Erika BR Callagon, Zhan Zhang, Neil C Sturchio, Sang Soo Lee, and Paul Fenter. X-ray–driven reaction front dynamics at calcite-water interfaces. *Science*, 349(6254):1330–1334, 2015.

[70] Huseyin Okur, Taner Tekin, A Kadir Ozer, and Mahmut Bayramoglu. Effect of ultrasound on the dissolution of colemanite in h2so4. *Hydrometallurgy*, 67(1-3):79–86, 2002.

[71] Chen Gruber, Chen Zhu, R Bastian Georg, Yevgeny Zakon, and Jiwchar Ganor. Resolving the gap between laboratory and field rates of feldspar weathering. *Geochimica et Cosmochimica Acta*, 147:90–106, 2014.

[72] AJ Gratz, Srinivas Manne, and PK Hansma. Atomic force microscopy of atomic-scale ledges and etch pits formed during dissolution of quartz. *Science*, 251(4999):1343–1346, 1991.

[73] Patricia M Dove and Nizhou Han. Kinetics of mineral dissolution and growth as reciprocal microscopic surface processes across chemical driving force. In *AIP Conference Proceedings*, volume 916, pages 215–234. American Institute of Physics, 2007.

[74] Jordi Cama, Li Zhang, Josep M Soler, Giovanni De Giudici, Rolf S Arvidson, and Andreas Lüttge. Fluorite dissolution at acidic ph: In situ afm and ex situ vsi experiments and monte carlo simulations. *Geochimica et Cosmochimica Acta*, 74(15):4298–4311, 2010.

[75] Pan Feng, Alexander S Brand, Lei Chen, and Jeffrey W Bullard. In situ nanoscale observations of gypsum dissolution by digital holographic microscopy. *Chemical geology*, 460:25–36, 2017.

[76] Alexander S Brand, Pan Feng, and Jeffrey W Bullard. Calcite dissolution rate spectra measured by in situ digital holographic microscopy. *Geochimica et cosmochimica acta*, 213:317–329, 2017.

[77] Alexander S Brand and Jeffrey W Bullard. Dissolution kinetics of cubic tricalcium aluminate measured by digital holographic microscopy. *Langmuir*, 33(38):9645–9656, 2017.

[78] Stephen Brunauer, Paul Hugh Emmett, and Edward Teller. Adsorption of gases in multimolecular layers. *Journal of the American chemical society*, 60(2):309–319, 1938.

[79] Susan L Brantley and Nathan P Mellott. Surface area and porosity of primary silicate minerals. *American Mineralogist*, 85(11-12):1767–1783, 2000.

[80] Ricarda D Rohlfs, Cornelius Fischer, Inna Kurganskaya, and Andreas Lüttge. Crystal dissolution kinetics studied by a combination of monte carlo and voronoi methods. *Minerals*, 8(4):133, 2018.

[81] Antonio C Lasaga and Andreas Lüttge. Mineralogical approaches to fundamental crystal dissolution kinetics. *American Mineralogist*, 89(4):527–540, 2004.

[82] William Gabriel Worley. *Dissolution kinetics and mechanisms in quartz-and grainite-water systems*. PhD thesis, Massachusetts Institute of Technology, 1994.

[83] Per Aagaard and Harold C Helgeson. Thermodynamic and kinetic constraints on reaction rates among minerals and aqueous solutions; i, theoretical considerations. *American journal of Science*, 282(3):237–285, 1982.

[84] Harold C Helgeson, William M Murphy, and Per Aagaard. Thermodynamic and kinetic constraints on reaction rates among minerals and aqueous solutions. ii. rate constants, effective surface area, and the hydrolysis of feldspar. *Geochimica et Cosmochimica Acta*, 48(12):2405–2432, 1984.

[85] Anthonio C. Lasaga and James Kirkpatrick. *Kinetics of Geochemical Processes*. De Gruyter, Berlin, Boston, 1981.

[86] Antonio C Lasaga. Chemical kinetics of water-rock interactions. *Journal of geophysical research: solid earth*, 89(B6):4009–4025, 1984.

[87] Nicholas Metropolis and Stanislaw Ulam. The monte carlo method. *Journal of the American statistical association*, 44(247):335–341, 1949.

[88] Nicholas Metropolis. The beginning of the monte carlo method. *Los Alamos Science*, 15(584):125–130, 1987.

[89] WM Young and EW Elcock. Monte carlo studies of vacancy migration in binary ordered alloys: I. *Proceedings of the Physical Society*, 89(3):735, 1966.

[90] Alfred B Bortz, Malvin H Kalos, and Joel L Lebowitz. A new algorithm for monte carlo simulation of ising spin systems. *Journal of Computational Physics*, 17(1):10–18, 1975.

[91] Shannon D. Piersall and James B. Anderson. Direct Monte Carlo simulation of chemical reaction systems: Simple bimolecular reactions. *The Journal of Chemical Physics*, 95(2):971, 1991.

[92] Tamás Vicsek and Fereydoon Family. Dynamic Scaling for Aggregation of Clusters. *Physical Review Letters*, 52(19):1669–1672, May 1984.

[93] Achutha Prabhu, Sujin B Babu, Jorge S Dolado, and J-C Gimel. Brownian cluster dynamics with short range patchy interactions: Its application to polymers and step-growth polymerization. *The Journal of chemical physics*, 141(2):024904, 2014.

[94] Corbett C Battaile and David J Srolovitz. Kinetic monte carlo simulation of chemical vapor deposition. *Annual Review of Materials Research*, 32(1):297–319, 2002.

[95] Richard Weinkamer, Peter Fratzl, Himadri S. Gupta, Oliver Penrose, and Joel L. Lebowitz. Using Kinetic Monte Carlo simulations to study phase separation in Alloys. *Phase Transitions*, 77(5-7):433–456, May 2004.

[96] Scott M. Auerbach and Horia I. Metiu. Diffusion in zeolites via cage-to-cage kinetics: Modeling benzene diffusion in Na-Y. *The Journal of Chemical Physics*, 105(9):3753, September 1996.

[97] Maria Jose Caturla. Toward a predictive atomistic model of ion implantation and dopant diffusion in silicon. *Computational Materials Science*, 12(4):319–332, November 1998.

[98] RM Ziff, E Gulari, and Y Barshad. Kinetic phase transitions in an irreversible surface-reaction model. *Physical review letters*, 56(24):2553–2556, June 1986.

[99] A. Saul, G. Treglia, and B. Legrand. Kinetics of segregation and dissolution in Cu-Ag and surface phase transition: comparison between mean field and Monte Carlo calculations. *Surface Science*, 307-309:804–809, April 1994.

[100] E. van Veenendaal, P. van Beurden, W. J. P. van Enckevort, E. Vlieg, J. van Suchtelen, and M. Elwenspoek. Monte Carlo study of kinetic smoothing during dissolution and etching of the Kossel (100) and silicon (111) surfaces. *Journal of Applied Physics*, 88(8):4595, October 2000.

[101] Andrei Andreevich Markov. The theory of algorithms. *Trudy Matematicheskogo Instituta Imeni VA Steklova*, 42:3–375, 1954.

[102] Louis F Williams Jr. A modification to the half-interval search (binary search) method. In *Proceedings of the 14th annual Southeast regional conference*, pages 95–101, 1976.

[103] Mikkel Jørgensen and Henrik Grönbeck. Montecoffee: A programmable kinetic monte carlo framework. *The Journal of chemical physics*, 149(11):114101, 2018.

[104] Pablo Martin Garcia, Hegoi Manzano Moro, Julio Luis Medina Pasaje, et al. Desarrollo de un código kinetic monte carlo para su aplicación en ciencia de materiales. 2015.

[105] Eric C Dybeck, Craig P Plaisance, and Matthew Neurock. Generalized temporal acceleration scheme for kinetic monte carlo simulations of surface catalytic processes by scaling the rates of fast reactions. *Journal of chemical theory and computation*, 13(4):1525–1538, 2017.

[106] Inna Kurganskaya and Andreas Lüttge. Kinetic monte carlo approach to study carbonate dissolution. *The Journal of Physical Chemistry C*, 120(12):6482–6492, 2016.

[107] Shikha Nangia and Barbara J Garrison. Advanced monte carlo approach to study evolution of quartz surface during the dissolution process. *Journal of the American Chemical Society*, 131(27):9538–9546, 2009.

[108] K. Oura, M. Katayama, A.A. Saranin, V.G. Lifshits, and A.V. Zotov. *Surface Science*, volume 602. Springer Science & Business Media, 2003.

[109] Thiago A de Assis and Fábio DA Aarão Reis. Dissolution of minerals with rough surfaces. *Geochimica et Cosmochimica Acta*, 228:27–41, 2018.

[110] Yong Liang, Donald R. Baer, James M. McCoy, James E. Amonette, and John P. Lafemina. Dissolution kinetics at the calcite-water interface. *Geochimica et Cosmochimica Acta*, 60(23):4883–4887, 1996.

[111] Kumaran Coopamootoo and Enrico Masoero. Bridging the gap between nanoparticle simulations and chemical kinetics of cement hydration. In *15th International Congress on the Chemistry of Cement (ICCC 2019)*. Newcastle University, 2019.

[112] Joel Z Bandstra and Susan L Brantley. Surface evolution of dissolving minerals investigated with a kinetic ising model. *Geochimica et Cosmochimica Acta*, 72(11):2587–2600, 2008.

[113] Barry M McCoy and Tai Tsun Wu. *The two-dimensional Ising model*. Courier Corporation, 2014.

[114] Luc Nicoleau and Maria Alice Bertolim. Analytical Model for the Alite (C3S) Dissolution Topography. *Journal of the American Ceramic Society*, 99(3):773–786, 2016.

[115] Paul Meakin and Kevin M. Rosso. Simple kinetic Monte Carlo models for dissolution pitting induced by crystal defects. *Journal of Chemical Physics*, 129(20), 2008.

[116] Cornelius Fischer and Andreas Lüttge. Pulsating dissolution of crystalline matter. *Proceedings of the National Academy of Sciences*, 115(5):897–902, 2018.

[117] Gerald V Gibbs, Robert T Downs, David F Cox, Nancy L Ross, Charles T Prewitt, Kevin M Rosso, Thomas Lippmann, and Armin Kirfel. Bonded interactions and the crystal chemistry of minerals: a review. *Zeitschrift für Kristallographie-Crystalline Materials*, 223(01-02):01–40, 2008.

[118] Abhijit Chatterjee and Arthur F Voter. Accurate acceleration of kinetic monte carlo simulations through the modification of rate constants. *The Journal of chemical physics*, 132(19):194101, 2010.

[119] Cornelius Fischer, Rolf S Arvidson, and Andreas Lüttge. How predictable are dissolution rates of crystalline material? *Geochimica et Cosmochimica Acta*, 98:177–185, 2012.

[120] Dennis G Zill. *A first course in differential equations with modeling applications*. Cengage Learning, 2012.

[121] NM Rose. Dissolution rates of prehnite, epidote, and albite. *Geochimica et Cosmochimica Acta*, 55(11):3273–3286, 1991.

[122] Yang Chen and Susan L Brantley. Temperature-and ph-dependence of albite dissolution rate at acid ph. *Chemical Geology*, 135(3-4):275–290, 1997.

[123] Andreas Bauer and Gilles Berger. Kaolinite and smectite dissolution rate in high molar koh solutions at 35 and 80 c. *Applied Geochemistry*, 13(7):905–916, 1998.

[124] Xingchen Ye, Matthew R Jones, Layne B Frechette, Qian Chen, Alexander S Powers, Peter Ercius, Gabriel Dunn, Grant M Rotskoff, Son C Nguyen, Vivekananda P Adiga, et al. Single-particle mapping of nonequilibrium nanocrystal transformations. *Science*, 354(6314):874–877, 2016.

[125] Igor Shvab, Laurent Brochard, Hegoi Manzano, and Enrico Masoero. Precipitation mechanisms of mesoporous nanoparticle aggregates: off-lattice, coarse-grained, kinetic simulations. *Crystal Growth & Design*, page acs.cgd.6b01712, jan 2017.

[126] Qianqian Wang, Hegoi Manzano, Yanhua Guo, I'nigo Lopez-Arbeloa, and Xiaodong Shen. Hydration mechanism of reactive and passive dicalcium silicate polymorphs from molecular simulations. *The Journal of Physical Chemistry C*, 119(34):19869–19875, 2015.

[127] Qianqian Wang, Hegoi Manzano, Iñigo López-Arbeloa, and Xiaodong Shen. Water adsorption on the β-dicalcium silicate surface from dft simulations. *Minerals*, 8(9):386, 2018.

[128] Emilio Artacho, Eduardo Anglada, Oswaldo Diéguez, Julian D Gale, Alberto García, Javier Junquera, Richard M Martin, Pablo Ordejón, José Miguel Pruneda, Daniel Sánchez-Portal, et al. The siesta method; developments and applicability. *Journal of Physics: Condensed Matter*, 20(6):064208, 2008.

[129] Julian D Gale. Gulp: A computer program for the symmetry-adapted simulation of solids. *Journal of the Chemical Society, Faraday Transactions*, 93(4):629–637, 1997.

[130] Paolo Giannozzi, Oliviero Andreussi, Thomas Brumme, Oana Bunau, M Buongiorno Nardelli, Matteo Calandra, Roberto Car, Carlo Cavazzoni, Davide Ceresoli, Matteo Cococcioni, et al. Advanced capabilities for materials modelling with quantum espresso. *Journal of Physics: Condensed Matter*, 29(46):465901, 2017.

[131] Steve Plimpton. Fast parallel algorithms for short-range molecular dynamics. Technical report, Sandia National Labs., Albuquerque, NM (United States), 1993.

[132] Steve Plimpton, Aidan Thompson, and Alex Slepoy. Stochastic parallel particle kinetic simulator. Technical report, Sandia National Laboratories, 2008.

[133] Elizabeth A Holm, Todd D Hoffmann, Anthony D Rollett, and Christopher G Roberts. Particle-assisted abnormal grain growth. In *IOP Conference Series: Materials Science and Engineering*, volume 89, page 012005. IOP Publishing, 2015.

[134] Theron M Rodgers, Jonathan D Madison, Veena Tikare, and Michael C Maguire. Predicting mesoscale microstructural evolution in electron beam welding. *JOM*, 68(5):1419–1426, 2016.

[135] Xinmin Tian, Aart Bik, Milind Girkar, Paul Grey, Hideki Saito, and Ernesto Su. Intel® openmp c++/fortran compiler for hyper-threading technology: Implementation and performance. *Intel Technology Journal*, 6(1), 2002.

[136] Pierre L'Ecuyer. Random number generation. In *Handbook of computational statistics*, pages 35–71. Springer, 2012.

[137] Unofficial xyz file format specification. `http://en.wikipedia.org/wiki/XYZ_file_format`. Accessed: 2019-10-1.

[138] Robert T Downs and Michelle Hall-Wallace. The american mineralogist crystal structure database. *American Mineralogist*, 88(1):247–250, 2003.

[139] Unit cell rotation with vesta. `https://ma.issp.u-tokyo.ac.jp/en/app-post/1788`. Accessed: 2020-03-15.

[140] Geodebra3d. `https://www.geogebra.org/3d?lang=en`. Accessed: 2020-03-15.

[141] Wolfram alpha. `https://www.wolframalpha.com`. Accessed: 2020-6-1.

[142] CS Kohli and MB Ives. Computer simulation of crystal dissolution morphology. *Journal of Crystal Growth*, 16(2):123–130, 1972.

[143] Antonius Petrus Johannes Jansen. *An introduction to kinetic Monte Carlo simulations of surface reactions*, volume 856. Springer, 2012.

[144] Mark D Hill and Michael R Marty. Amdahl's law in the multicore era. *Computer*, 41(7):33–38, 2008.

[145] Daniel Berthelot. Sur le mélange des gaz. *Compt. Rendus*, 126:1703–1855, 1898.

[146] C André Ohlin, Eric M Villa, James R Rustad, and William H Casey. Dissolution of insulating oxide materials at the molecular scale. *Nature materials*, 9(1):11, 2010.

[147] William O'Mara, Robert B Herring, and Lee P Hunt. *Handbook of semiconductor silicon technology*. Crest Publishing House, 2007.

[148] Gerrit Land and Dietmar Stephan. Controlling cement hydration with nanoparticles. *Cement and Concrete Composites*, 57:64–67, 2015.

[149] Francisco J Vela, Roberto Palos, Javier Bilbao, José M Arandes, and Alazne Gutiérrez. Effect of co-feeding hdpe on the product distribution in the hydrocracking of vgo. *Catalysis Today*, 2019.

[150] Frank K Crundwell. On the mechanism of the dissolution of quartz and silica in aqueous solutions. *ACS omega*, 2(3):1116–1127, 2017.

[151] Svetlana V Yanina, Kevin M Rosso, and Paul Meakin. Defect distribution and dissolution morphologies on low-index surfaces of α-quartz. *Geochimica et cosmochimica acta*, 70(5):1113–1127, 2006.

[152] MW Wegner and JM Christie. Chemical etching of deformation sub-structures in quartz. *Physics and Chemistry of Minerals*, 9(2):67–78, 1983.

[153] Kevin G Knauss and Thomas J Wolery. The dissolution kinetics of quartz as a function of ph and time at 70 c. *Geochimica et Cosmochimica Acta*, 52(1):43–53, 1988.

[154] Shikha Nangia and Barbara J Garrison. Ab initio study of dissolution and precipitation reactions from the edge, kink, and terrace sites of quartz as a function of ph. *Molecular Physics*, 107(8-12):831–843, 2009.

[155] Charles L Schaffer and Kendall T Thomson. Density functional theory investigation into structure and reactivity of prenucleation silica species. *The Journal of Physical Chemistry C*, 112(33):12653–12662, 2008.

[156] Louise J Criscenti, James D Kubicki, and Susan L Brantley. Silicate glass and mineral dissolution: calculated reaction paths and activation energies for hydrolysis of a q3 si by h3o+ using ab initio methods. *The Journal of Physical Chemistry A*, 110(1):198–206, 2006.

[157] Li Zhang and Andreas Lüttge. Theoretical approach to evaluating plagioclase dissolution mechanisms. *Geochimica et Cosmochimica Acta*, 73(10):2832–2849, 2009.

[158] Adam F Wallace, GV Gibbs, and Patricia M Dove. Influence of ion-associated water on the hydrolysis of si- o bonded interactions. *The Journal of Physical Chemistry A*, 114(7):2534–2542, 2010.

[159] Yitian Xiao and Antonio C Lasaga. Ab initio quantum mechanical studies of the kinetics and mechanisms of quartz dissolution: Oh- catalysis. *Geochimica et Cosmochimica Acta*, 60(13):2283–2295, 1996.

[160] M Liu, RA Yund, J Tullis, L Topor, and A Navrotsky. Energy associated with dislocations: A calorimetric study using synthetic quartz. *Physics and Chemistry of Minerals*, 22(2):67–73, 1995.

[161] α-quartz unit cell cif file. http://rruff.geo.arizona.edu/AMS/download.php?id=12600.cif&down=cif. Accessed: 2020-02-20.

[162] Vladimir V Murashov. Reconstruction of pristine and hydrolyzed quartz surfaces. *The Journal of Physical Chemistry B*, 109(9):4144–4151, 2005.

[163] F Wendler, A Okamoto, and Philipp Blum. Phase-field modeling of epitaxial growth of polycrystalline quartz veins in hydrothermal experiments. *Geofluids*, 16(2):211–230, 2016.

[164] Achutha Prabhu, Jean-Christophe Gimel, Andrés Ayuela, Silvia Arrese-Igor, Juan J Gaitero, and Jorge S Dolado. A multi-scale approach for percolation transition and its application to cement setting. *Scientific reports*, 8(1):1–11, 2018.

[165] Peter Hewlett and Martin Liska. *Lea's chemistry of cement and concrete*. Butterworth-Heinemann, 2019.

[166] HN Stein and JM Stevels. Influence of silica on the hydration of 3 cao, sio2. *Journal of Applied Chemistry*, 14(8):338–346, 1964.

[167] David L Kantro, Stephen Brunauer, and CHARLES H Weise. Development of surface in the hydration of calcium silicates. ii. extension of investigations to earlier and later stages of hydration. *The Journal of Physical Chemistry*, 66(10):1804–1809, 1962.

[168] Ellis M Gartner and Hamlin M Jennings. Thermodynamics of calcium silicate hydrates and their solutions. *Journal of the American Ceramic Society*, 70(10):743–749, 1987.

[169] EM Gartner, JF Young, DA Damidot, and I Jawed. Hydration of portland cement. *Structure and performance of cements*, 2:57–113, 2002.

[170] Paul Wencil Brown, Ellen Franz, Geoffrey Frohnsdorff, and HFW Taylor. Analyses of the aqueous phase during early c3s hydration. *Cement and Concrete Research*, 14(2):257–262, 1984.

[171] JGM De Jong, HN Stein, and JM Stevels. Hydration of tricalcium silicate. *Journal of Applied Chemistry*, 17(9):246–250, 1967.

[172] Renichi Kondo and Masaki Daimon. Early hydration of tricalcium silicate: a solid reaction with induction and acceleration periods. *Journal of the American Ceramic Society*, 52(9):503–508, 1969.

[173] James Derek Birchall, AJ Howard, and JE Bailey. On the hydration of portland cement. *Proceedings of the Royal Society of London. A. Mathematical and Physical Sciences*, 360(1702):445–453, 1978.

[174] DD Double, A Hellawell, and SJ Perry. The hydration of portland cement. *Proceedings of the Royal Society of London. A. Mathematical and Physical Sciences*, 359(1699):435–451, 1978.

[175] J Skalny and JF Young. Mechanisms of portland cement hydration. In *Proceedings, 7th International Symposium Chemical of Cement, Paris*, volume 1, pages 3–45, 1980.

[176] ME Tadros, JAN Skalny, and RS Kalyoncu. Early hydration of tricalcium silicate. *Journal of the American Ceramic Society*, 59(7-8):344–347, 1976.

[177] Ivan Odler and J Schüppstuhl. Early hydration of tricalcium silicate iii. control of the induction period. *Cement and Concrete Research*, 11(5-6):765–774, 1981.

[178] Toshio Sakurai, Takeshi Sato, and Atushi Yoshinaga. The effect of minor components on the early hydraulic activity of the major phases of portland cement clinker. In *Proceedings of the fifth international symposium on the chemistry of cement*, volume 1, pages 300–321, 1968.

[179] JN Maycock, J Skalny, and R Kalyoncu. Crystal defects and hydration i. influence of lattice defects. *Cement and Concrete Research*, 4(5):835–847, 1974.

[180] P Fierens and JP Verhaegen. Hydration of tricalcium silicate in paste—kinetics of calcium ions dissolution in the aqueous phase. *Cement and Concrete Research*, 6(3):337–342, 1976.

[181] JF Young, HS Tong, and RL Berger. Compositions of solutions in contact with hydrating tricalcium silicate pastes. *Journal of the American Ceramic Society*, 60(5-6):193–198, 1977.

[182] P Barret and D Ménétrier. Filter dissolution of c3s as a function of the lime concentration in a limited amount of lime water. *Cement and Concrete Research*, 10(4):521–534, 1980.

[183] I Odler and H Dörr. Early hydration of tricalcium silicate ii. the induction period. *Cement and Concrete Research*, 9(3):277–284, 1979.

[184] S Garrault-Gauffinet and A Nonat. Experimental investigation of calcium silicate hydrate (csh) nucleation. *Journal of crystal growth*, 200(3-4):565–574, 1999.

[185] L Nicoleau and A Nonat. A new view on the kinetics of tricalcium silicate hydration. *Cement and Concrete Research*, 86:1–11, 2016.

[186] Melvin Avrami. Kinetics of phase change. i general theory. *The Journal of chemical physics*, 7(12):1103–1112, 1939.

[187] John W Cahn. The kinetics of grain boundary nucleated reactions. *Acta metallurgica*, 4(5):449–459, 1956.

[188] Jeffrey J Thomas. A new approach to modeling the nucleation and growth kinetics of tricalcium silicate hydration. *Journal of the American Ceramic Society*, 90(10):3282–3288, 2007.

[189] Shashank Bishnoi and Karen L Scrivener. Studying nucleation and growth kinetics of alite hydration using μic. *Cement and Concrete Research*, 39(10):849–860, 2009.

[190] Jeffrey J Thomas, Hamlin M Jennings, and Jeffrey J Chen. Influence of nucleation seeding on the hydration mechanisms of tricalcium silicate and cement. *The Journal of Physical Chemistry C*, 113(11):4327–4334, 2009.

[191] George W Scherer, Jie Zhang, and Jeffrey J Thomas. Nucleation and growth models for hydration of cement. *Cement and Concrete Research*, 42(7):982–993, 2012.

[192] George W Scherer. Models of confined growth. *Cement and concrete research*, 42(9):1252–1260, 2012.

[193] R Gonzalez-Teresa, Jorge S Dolado, Andrés Ayuela, and Jean-Christophe Gimel. Nanoscale texture development of csh gel: a computational model for nucleation and growth. *Applied Physics Letters*, 103(23):234105, 2013.

[194] Shashank Bishnoi. Geometric limitations of nucleation and growth models: Revisiting the impingement assumption. *Cement and concrete research*, 46:30–40, 2013.

[195] Jeffrey J Thomas, Joseph J Biernacki, Jeffrey W Bullard, Shashank Bishnoi, Jorge S Dolado, George W Scherer, and Andreas Luttge. Modeling and simulation of cement hydration kinetics and microstructure development. *Cement and concrete research*, 41(12):1257–1278, 2011.

[196] Jeffrey W Bullard. A determination of hydration mechanisms for tricalcium silicate using a kinetic cellular automaton model. *Journal of the American Ceramic Society*, 91(7):2088–2097, 2008.

[197] Enrico Masoero, Jeffrey J Thomas, and Hamlin M Jennings. A reaction zone hypothesis for the effects of particle size and water-to-cement ratio on the early hydration kinetics of c3s. *Journal of the American Ceramic Society*, 97(3):967–975, 2014.

[198] Karen Scrivener, Alexandre Ouzia, Patrick Juilland, and Aslam Kunhi Mohamed. Advances in understanding cement hydration mechanisms. *Cement and Concrete Research*, 124:105823, 2019.

[199] Alite unit cell cif file. `http://rruff.geo.arizona.edu/AMS/download.php?id=14493.cif&down=cif`. Accessed: 2020-07-15.

[200] Jeffrey J Thomas. The instantaneous apparent activation energy of cement hydration measured using a novel calorimetry-based method. *Journal of the American Ceramic Society*, 95(10):3291–3296, 2012.

[201] Elizaveta Pustovgar, Rahul P Sangodkar, Andrey S Andreev, Marta Palacios, Bradley F Chmelka, Robert J Flatt, and Jean-Baptiste d'Espinose de Lacaillerie. Understanding silicate hydration from quantitative analyses of hydrating tricalcium silicates. *Nature communications*, 7(1):1–9, 2016.

[202] J Bonneville and J-L Martin. Multiplication, mobility and exhaustion of dislocations. In *Multiscale Phenomena in Plasticity: From Experiments to Phenomenology, Modelling and Materials Engineering*, pages 57–66. Springer, 2000.

Appendix A: KIMERA input files

Below we show, in order of appearance, the necessary commands and some indications to perform the simulations shown throughout the thesis in the KIMERA program.

A.1 Quartz. Model SCS-L1

```
DIMENSION_A 50
DIMENSION_B 40
DIMENSION_C 30

CELL_A 5.01
CELL_B 5.01
CELL_C 5.47
CELL_ALPHA 90
CELL_BETA 90
CELL_GAMMA 120

READ_POSITIONS_FROM_XYZ_FILE    path-to-xyz-file/Quartz-without-O.xyz

DEFINE_DISSOLUTION_EVENT Si NEIGHBOUR Si 3.09832 28.0 10.0 4
    NEIGHBOUR_LINKED Si 5.01000 LINK Si 3.09832 3.09832 4.0 1.0 0
    NEIGHBOUR_LINKED Si 5.66774 LINK Si 3.09832 3.09832 4.0 1.0 0
    NEIGHBOUR_LINKED Si 4.42416 LINK Si 3.09832 3.09832 4.0 1.0 0
    FFD 1.0e12
    FFP 1.0e12

DELTA_G* -100.0
TARGET_TIME 8.0e22

SURFACE_FRAMES 30
DATA_ANALYSIS 300
MEAN_DISSOLVED_ANALYSIS  30

REMOVE_CUBE 0.0    0.0    0.0    600.0
ADD_ELLIPSOID   75.0    85.0    80.0    65.0     85.0    75.0
ADD_YZ_DISLOCATION  80.0    80.0   3.1
```

```
WORK_NAME Quartz-grain-modelSCS-L1
```

A.1.1 xyz quartz file

Moreover, the '.xyz' file without oxygen atoms is needed:

```
7
Si O2
Si    2.50500    0.00000    0.00000
Si    2.50500    0.00000    5.47000
Si    0.00000    4.33879    0.00000
Si    0.00000    4.33879    5.47000
Si   -1.25250    2.16939    3.64667
Si    3.75750    2.16939    3.64667
Si    1.25250    2.16939    1.82333
```

A.2 AB Kossel crystals

A.2.1 Configuration B

Simulation at far from equilibrium conditions $\Delta G^* = -100$ and energy barrier values $E_{\mathrm{da_{A\text{-}A}}} = 12$, $E_{\mathrm{da_{B\text{-}B}}} = 4$ and $E_{\mathrm{da_{A\text{-}B}}} = 6.92\ k_{\mathrm{B}}T$ units and $E_{\mathrm{pa_{A\text{-}A}}} = E_{\mathrm{pa_{B\text{-}B}}} = E_{\mathrm{pa_{A\text{-}B}}} = 1\ k_{\mathrm{B}}T$ units

```
DIMENSION_A 60
DIMENSION_B 60
DIMENSION_C 15

CELL_A 5.0
CELL_B 5.0
CELL_C 5.0
CELL_ALPHA 90
CELL_BETA 90
CELL_GAMMA 90

----1----
POSITION    B    0.0    0.0    0.0  1
```

```
----2----
 POSITION    A    2.5    0.0    0.0  1
----3----
 POSITION    B    0.0    0.0    2.5  1
----4----
 POSITION    A    2.5    0.0    2.5  1
----5----
 POSITION    A    0.0    2.5    0.0  1
----6----
 POSITION    B    2.5    2.5    0.0  1
----7----
 POSITION    A    0.0    2.5    2.5  1
----8----
 POSITION    B    2.5    2.5    2.5  1

 DEFINE_DISSOLUTION_EVENT A
     NEIGHBOUR A 2.5 12.0 1.0 2
     NEIGHBOUR B 2.5 6.92 1.00 4
     FFD 4e13
     FFP 4e13

 DEFINE_DISSOLUTION_EVENT B
     NEIGHBOUR B 2.5 4.0 1.0 2
     NEIGHBOUR A 2.5 6.92 1.00 4
     FFD 4e13
     FFP 4e13

 PERIODICITY A B

--change dG* below to deltaG study
 DELTA_G* -100.0
 TARGET_STEP 400000

 SURFACE_FRAMES 20
 DATA_ANALYSIS 100
 LAYER_ANALYSIS C 100
 MEAN_DISSOLVED_ANALYSIS 10

 DEFINE_AB_INSOLUBLE_CELLS   0   0   0   60   60
 REMOVE_AC_PLANE_BY_CELLS    30   30   5   1   9
 REMOVE_AC_PLANE_BY_CELLS    30   30   14   1   1
 REMOVE_CUBE_FROM_SURFACE    150.0  150.0  -80.0  152.49

 WORK_NAME AB_KC_configurationB
```

A.2.2 Configuration F

Simulation at far from equilibrium conditions $\Delta G^* = -100$ and energy barrier values $E_{\mathrm{da_{A\text{-}A}}} = 12$, $E_{\mathrm{da_{B\text{-}B}}} = 4$ and $E_{\mathrm{da_{A\text{-}B}}} = 6.92\ k_{\mathrm{B}}T$ units and $E_{\mathrm{pa_{A\text{-}A}}} = E_{\mathrm{pa_{B\text{-}B}}} = E_{\mathrm{pa_{A\text{-}B}}} = 1\ k_{\mathrm{B}}T$ units

```
DIMENSION_A 120
DIMENSION_B 120
DIMENSION_C 30

POSITION    A    0.5000    0.5000    0.5000   0.5
POSITION    B    0.5000    0.5000    0.5000   0.5

DEFINE_DISSOLUTION_EVENT A
    NEIGHBOUR A 2.5 12.0 1.0 6
    NEIGHBOUR B 2.5 6.92 1.00 6
    FFD 4e13
    FFP 4e13

DEFINE_DISSOLUTION_EVENT B
    NEIGHBOUR B 2.5 4.0 1.0 6
    NEIGHBOUR A 2.5 6.92 1.00 6
    FFD 4e13
    FFP 4e13

SEED_BOX 20
PERIODICITY A B

CELL_A 2.5
CELL_B 2.5
CELL_C 2.5
CELL_ALPHA 90
CELL_BETA 90
CELL_GAMMA 90

--change dG* below to deltaG study
DELTA_G* -100.0
TARGET_STEP 400000

SURFACE_FRAMES 20
DATA_ANALYSIS 100
LAYER_ANALYSIS C 100
MEAN_DISSOLVED_ANALYSIS 10
```

```
DEFINE_AB_INSOLUBLE_CELLS   0   0   0   120   120

REMOVE_AC_PLANE_BY_CELLS    60   60   10   2   19
REMOVE_AC_PLANE_BY_CELLS    60   60   29   2   1
REMOVE_AC_PLANE_BY_CELLS    60   61   10   2   19
REMOVE_AC_PLANE_BY_CELLS    60   61   29   2   1

REMOVE_CUBE_FROM_SURFACE    150.0  150.0  -80.0  152.49

WORK_NAME AB_KC_configurationF
```

A.3 Quartz

A.3.1 {001} plane

```
DIMENSION_A 240
DIMENSION_B 240
DIMENSION_C 10

READ_POSITIONS_FROM_XYZ_FILE path_to_xyzfile/quartz.xyz

--change energy barrier values and ffd and ffp below to temperature study
DEFINE_DISSOLUTION_EVENT O NEIGHBOUR_DIRECT_LIST  O   2.585   LIST_LENGTH 6
19.02748414 15.22198732
21.56448203 17.7589852
24.10147992 20.29598309
26.6384778  26.6384778
34.24947146 34.24947146
50.73995772 50.73995772
6
NEIGHBOUR   Si     1.58333      0.0       0.0       2
FFD   2.45E+10
FFP   2.45E+10
DG* -100.0

--change only dG above to deltaG study

DEFINE_DISSOLUTION_EVENT
Si  NEIGHBOUR   O     1.58333    100.0    0.0        4
FFD   2.45E+10
```

```
FFP   2.45E+10
DG* -200.0

SET_MASS Si 28.08
SET_MASS O 16.0

CELL_A 5.01
CELL_B 5.01
CELL_C 5.47
CELL_ALPHA 90
CELL_BETA 90
CELL_GAMMA 120

PERIODICITY A B

BOX_FRAMES 10
SURFACE_FRAMES 50
DATA_ANALYSIS 500
LAYER_ANALYSIS C 50
MEAN_DISSOLVED_ANALYSIS  50

DISTANCE_ACCURACY 0.01
TARGET_STEP 1000000

REMOVE_AC_PLANE_BY_CELLS    120   120   0   1   10

DEFINE_AB_INSOLUBLE_CELLS   0   0   0   240   240

REMOVE_AB_PLANE_FROM_SURFACE    0   0   0   240   240
REMOVE_AB_PLANE_FROM_SURFACE    0   0   1   240   240
REMOVE_AB_PLANE_FROM_SURFACE    0   0   2   240   240
REMOVE_AB_PLANE_FROM_SURFACE    0   0   3   240   240
REMOVE_AB_PLANE_FROM_SURFACE    0   0   4   240   240
REMOVE_AB_PLANE_FROM_SURFACE    0   0   5   240   240
REMOVE_AB_PLANE_FROM_SURFACE    0   0   6   240   240
REMOVE_AB_PLANE_FROM_SURFACE    0   0   7   240   240
REMOVE_AB_PLANE_FROM_SURFACE    0   0   8   240   240

WORK_NAME Quartz_001plane
```

A.3.2 {001} plane with stabilization

```
DIMENSION_A 240
DIMENSION_B 240
DIMENSION_C 10

READ_POSITIONS_FROM_XYZ_FILE path_to_xyzfile/quartz.xyz

--change energy barrier values and ffd and ffp below to temperature study
DEFINE_DISSOLUTION_EVENT O NEIGHBOUR_DIRECT_LIST  O   2.585   LIST_LENGTH 6
19.02748414 15.22198732
21.56448203 17.7589852
24.10147992 20.29598309
26.6384778  26.6384778
34.24947146 34.24947146
50.73995772 50.73995772
6
NEIGHBOUR   Si     1.58333      0.0       0.0       2
FFD   2.45E+10
FFP   2.45E+10
DG* -100.0

--change only dG above to deltaG study

DEFINE_DISSOLUTION_EVENT
Si  NEIGHBOUR   O     1.58333    100.0    0.0        4
FFD   2.45E+10
FFP   2.45E+10
DG* -200.0

SET_MASS Si 28.08
SET_MASS O 16.0

CELL_A 5.01
CELL_B 5.01
CELL_C 5.47
CELL_ALPHA 90
CELL_BETA 90
CELL_GAMMA 120

PERIODICITY A B

BOX_FRAMES 10
SURFACE_FRAMES 50
```

```
DATA_ANALYSIS 500
LAYER_ANALYSIS C 50
MEAN_DISSOLVED_ANALYSIS  50

DISTANCE_ACCURACY 0.01
TARGET_STEP 1000000

REMOVE_AC_PLANE_BY_CELLS    120   120   0   1   10

DEFINE_AB_INSOLUBLE_CELLS   0   0   0   240   240

REMOVE_AB_PLANE_FROM_SURFACE    0   0   0   240   240
REMOVE_AB_PLANE_FROM_SURFACE    0   0   1   240   240
REMOVE_AB_PLANE_FROM_SURFACE    0   0   2   240   240
REMOVE_AB_PLANE_FROM_SURFACE    0   0   3   240   240
REMOVE_AB_PLANE_FROM_SURFACE    0   0   4   240   240
REMOVE_AB_PLANE_FROM_SURFACE    0   0   5   240   240
REMOVE_AB_PLANE_FROM_SURFACE    0   0   6   240   240
REMOVE_AB_PLANE_FROM_SURFACE    0   0   7   240   240
REMOVE_AB_PLANE_FROM_SURFACE    0   0   8   240   240
REMOVE_AB_PLANE_FROM_SURFACE    0   0   9   240   240

ADD_AB_PLANE_TO_SURFACE  119   119   9   3   1
ADD_AB_PLANE_TO_SURFACE  119   121   9   3   1
ADD_AB_PLANE_TO_SURFACE  119   120   9   1   1
ADD_AB_PLANE_TO_SURFACE  121   120   9   1   1

WORK_NAME Quartz_001plane_S
```

A.3.3 Wulff shape

```
DIMENSION_A 16
DIMENSION_B 16
DIMENSION_C 47

CELL_A 5.01
CELL_B 5.01
CELL_C 5.47
CELL_ALPHA 90
CELL_BETA 90
CELL_GAMMA 120
```

```
READ_POSITIONS_FROM_XYZ_FILE    path-to-xyz-file/Quartz.xyz

DEFINE_DISSOLUTION_EVENT O NEIGHBOUR_DIRECT_LIST   O   2.585   LIST_LENGTH 6
19.02748414 15.22198732
21.56448203 17.7589852
24.10147992 20.29598309
26.6384778  26.6384778
34.24947146 34.24947146
50.73995772 50.73995772
6
NEIGHBOUR   Si  1.58333 0.0 0.0 2
FFD   2.45E+10
FFP   2.45E+10
DG*  -100.0

DEFINE_DISSOLUTION_EVENT    Si
NEIGHBOUR   O   1.58333 100.0   0.0 4
FFD   2.45E+10
FFP   2.45E+10
DG* -200.0

SET_MASS Si 28.08
SET_MASS O 16.0

BOX_FRAMES 2
SURFACE_FRAMES 50
DATA_ANALYSIS 300
MEAN_DISSOLVED_ANALYSIS  30

DISTANCE_ACCURACY 0.01
TARGET_STEP 62700

REMOVE_PLANE 726868.37 -419657.66 347.09998 -99105912 83.352005
REMOVE_PLANE 731025.25 -417257.66 994.50000 1.0343943e+08 88.528000
REMOVE_PLANE -187175.30 108065.70 173899.36 -86372176 152.25000
REMOVE_PLANE -187175.30 -108065.70 173897.84 -71101464 124.24800
REMOVE_PLANE 0.0000000 -216131.41 173897.11 -58946700 80.431999
REMOVE_PLANE 187175.30 -108065.70 173897.84 -81832440 135.88800
REMOVE_PLANE 187175.30 108065.70 173899.36 -84200872 117.38000
REMOVE_PLANE 0.0000000 216131.41 173900.09 -85376280 121.61600
REMOVE_PLANE -187175.30 -108065.70 173898.59 29434504 79.064003
REMOVE_PLANE -187175.30 108065.70 173898.59 17969432 64.776001
REMOVE_PLANE 0.0000000 216131.41 173898.59 12254965 71.220001
REMOVE_PLANE 187175.30 108065.70 173898.59 10416989 64.596001
REMOVE_PLANE 187175.30 -108065.70 173898.59 19110464 68.889999
```

```
REMOVE_PLANE 0.0000000 -216131.41 173898.59 29767128 80.262001

ADD_XZ_DISLOCATION  19  149.682   3.1

REMOVE_XZ_DISLOCATION_FROM_SURFACE  19  149.682   6.0
    FROM_Y_TO_Y   0.82     68.7

ADD_XY_DISLOCATION  2.128   45.6    3.1

REMOVE_XY_DISLOCATION_FROM_SURFACE  2.128   45.6    6.0
    FROM_Z_TO_Z    27.6  226.56

WORK_NAME Quartz-wulff
```

A.3.4 xyz quartz file

Moreover, the '.xyz' file with oxygen atoms is needed in all the three previous examples:

```
9
Si O2
Si    2.50500    0.00000    0.00000
Si   -1.25250    2.16939    3.64667
Si    1.25250    2.16939    1.82333
 O    1.59543    0.92112    0.91167
 O    3.41457    0.92112    4.55833
 O    2.50500    2.49654    2.73500
 O    0.90957    3.41766    0.91167
 O   -0.90957    3.41766    4.55833
 O    0.00000    1.84225    2.73500
```

A.4 Alite. Kossel crystal

```
DIMENSION_A 200
DIMENSION_B 200
DIMENSION_C 80

POSITION    Any    0.5000    0.5000    0.5000   1
```

```
DEFINE_DISSOLUTION_EVENT Any NEIGHBOUR_DIRECT_LIST  Any  4.9   LIST_LENGTH 6
13.2 13.2
15.2 11.5
17.6 10.3
20.0 9.0
22.0 7.3
24.0 5.7
6
FFD  6e8
FFP  6e8
DG* -100.0

--change only dG above to deltaG study

PERIODICITY A B

CELL_A 4.9
CELL_B 4.9
CELL_C 4.9
CELL_ALPHA 90
CELL_BETA 90
CELL_GAMMA 90

SURFACE_FRAMES 50
DATA_ANALYSIS 500
LAYER_ANALYSIS C 10
MEAN_DISSOLVED_ANALYSIS 100

TARGET_STEP 3000000

DEFINE_AB_INSOLUBLE_CELLS          0   0   0   200   200
REMOVE_AC_PLANE_BY_CELLS           100   100   0   1   80

REMOVE_AC_PLANE_FROM_SURFACE                99   100   0   1   79
REMOVE_AC_PLANE_FROM_SURFACE                101   100   0   1   79
REMOVE_AC_PLANE_FROM_SURFACE                100   99   0   1   79
REMOVE_AC_PLANE_FROM_SURFACE                100   101   0   1   79

WORK_NAME KC_ALITA_MODEL3
```

Appendix B: Cement chemistry notation

Cement chemistry notation is as follows:

C = CaO H = H_2O $\hat{S}$ = SO_3 F = Fe_2O_3 S = SiO_2 M = MgO K = K_2O A = Al_2O_3

N=Na_2O P = P_2O_5